

REPORT DOCUMENTATION PAGE				Form Approved OMB No. 0704-0188	
The public reporting burden for this collection of information is estimated to average 1 hour per response, including the time for reviewing instructions, searching existing data sources, gathering and maintaining the data needed, and completing and reviewing the collection of information. Send comments regarding this burden estimate or any other aspect of this collection of information, including suggestions for reducing the burden, to Department of Defense, Washington Headquarters Services, Directorate for Information Operations and Reports (0704-0188), 1215 Jefferson Davis Highway, Suite 1204, Arlington, VA 22202-4302. Respondents should be aware that notwithstanding any other provision of law, no person shall be subject to any penalty for failing to comply with a collection of information if it does not display a currently valid OMB control number.					
PLEASE DO NOT RETURN YOUR FORM TO THE ABOVE ADDRESS.					
1. REPORT DATE (DD-MM-YYYY) 21/Aug/2001		2. REPORT TYPE DISSERTATION		3. DATES COVERED (From - To)	
4. TITLE AND SUBTITLE OBSERVED MICROPHYSICAL AND RADIATIVE STRUCTURE OF MID LEVEL, MIXED PHASED CLOUDS				5a. CONTRACT NUMBER	
				5b. GRANT NUMBER	
				5c. PROGRAM ELEMENT NUMBER	
				5d. PROJECT NUMBER	
6. AUTHOR(S) MAJ FLEISHAUER ROBERT P				5e. TASK NUMBER	
				5f. WORK UNIT NUMBER	
7. PERFORMING ORGANIZATION NAME(S) AND ADDRESS(ES) ST LOUIS UNIVERSITY				8. PERFORMING ORGANIZATION REPORT NUMBER CI01-204	
9. SPONSORING/MONITORING AGENCY NAME(S) AND ADDRESS(ES) THE DEPARTMENT OF THE AIR FORCE AFIT/CIA, BLDG 125 2950 P STREET WPAFB OH 45433				10. SPONSOR/MONITOR'S ACRONYM(S)	
				11. SPONSOR/MONITOR'S REPORT NUMBER(S)	
12. DISTRIBUTION/AVAILABILITY STATEMENT Unlimited distribution In Accordance With AFI 35-205/AFIT Sup 1					
13. SUPPLEMENTARY NOTES					
<div style="font-size: 2em; font-weight: bold;">20010904 046</div>					
14. ABSTRACT					
15. SUBJECT TERMS					
16. SECURITY CLASSIFICATION OF:			17. LIMITATION OF ABSTRACT	18. NUMBER OF PAGES 176	19a. NAME OF RESPONSIBLE PERSON
a. REPORT	b. ABSTRACT	c. THIS PAGE			19b. TELEPHONE NUMBER (Include area code)

The views expressed in this article are those of the author and do not reflect the official policy or position of the United States Air Force, Department of Defense, or the U.S. Government

DISSERTATION

OBSERVED MICROPHYSICAL AND RADIATIVE  
STRUCTURE OF MID-LEVEL, MIXED-PHASE CLOUDS

Submitted by

Robert P. Fleishauer

Department of Atmospheric Science

In partial fulfillment of the requirements

For the Degree of Doctor of Philosophy

Colorado State University

Fort Collins, Colorado

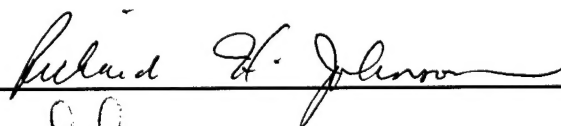
Summer 2001

COLORADO STATE UNIVERSITY

May 21, 2001

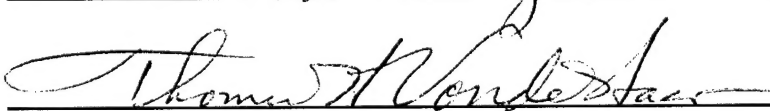
WE HEREBY RECOMMEND THAT THE DISSERTATION  
PREPARED UNDER OUR SUPERVISION BY ROBERT P. FLEISHAUER  
ENTITLED OBSERVED MICROPHYSICAL AND RADIATIVE STRUCTURE  
OF MID-LEVEL MIXED-PHASE CLOUDS BE ACCEPTED AS FULFILLING  
IN PART REQUIREMENTS FOR THE DEGREE OF DOCTOR OF  
PHILOSOPHY.

Committee on Graduate Work

  
\_\_\_\_\_

  
\_\_\_\_\_

  
\_\_\_\_\_

  
\_\_\_\_\_

Adviser

  
\_\_\_\_\_

Department Head

## **ABSTRACT OF DISSERTATION**

### **OBSERVED MICROPHYSICAL AND RADIATIVE STRUCTURE OF MID-LEVEL, MIXED-PHASE CLOUDS**

Airborne measurements of six mid-level clouds observed over the Great Plains of the United States in late 1999 and early 2000 are analyzed extensively. All cloud fields are associated with a 500-mb low-pressure center or a potential vorticity maximum, with additional lift provided by upper-level jet streams. Data show that these innocuous looking clouds display complicated microphysical and thermodynamic structures. Five of six cases include mixed-phase conditions in temperatures ranging from near freezing to  $-31^{\circ}\text{C}$ , at altitudes of 2400 to 7200 m. Four of the cases consist of a single cloud layer, while the other two are multi-layered systems. Of particular note, in single-layered clouds, there is an increase of liquid water content with height versus a decrease in ice water content over the same depth. This is in contrast to multi-layered systems, where the liquid water content has the same basic shape, but the ice water content is distributed more uniformly throughout all layers. We attribute these structural differences to a seeder-feeder mechanism operating in the multi-layered systems.

A lack of temperature inversions in these mid-level clouds is a major difference from the thermodynamic structure of most stratocumulus systems. We found the virtual potential temperature to be the best discriminator of cloud interfaces for mid-level clouds, with 1-2° C differences between ambient and cloud air. A noteworthy contribution to this observational study was the use of the Cloud Particle Imager (CPI) instrument for the qualitative analysis of the particle sizes, shapes, habits, and distributions through the cloud. An analysis of the liquid water budget of a Lagrangian cloud sample revealed that large-scale subsidence was the main mechanism responsible for its dissipation. Heating rates and fluxes are computed for each cloud using a single-column radiative transfer model. Sensitivity studies included the radiative effects of doubling and halving liquid and ice water content, which changed the radiative cooling and heating rates by 25 to 30%. Incorrect parameterizations of cloud water phase resulted in vertical net radiative heating rate errors of 400%.

Microphysical data collected from these mid-level, mixed-phase clouds provide the observational base needed to increase our understanding of how mid-level clouds are generated, maintained, and dissipated, thus allowing for the development of better parameterizations in large-scale numerical models and improved methods for retrieving cloud properties with remote sensing instruments.

Robert P. Fleishauer  
Department of Atmospheric Science  
Colorado State University  
Fort Collins, Colorado, 80523  
Summer 2001

Advisor: Thomas H. Vonder Haar

## ACKNOWLEDGEMENTS

- Many thanks to my advisor, Dr. Thomas Vonder Haar, who has been a great mentor to me in every facet of my student career at Colorado State University.
- Thanks also to my dissertation committee: Drs. Graeme Stephens, Richard Johnson and David Krueger for their help and support.
- I sincerely appreciated the encouragement and help I received from Vince Larson, Adam Kankiewicz, Don Reinke, Larry Carey, Jim Kossin, Scott Hausman, Ken Knapp, Brian McNoldy, Rich Moore, and Julie Demuth.
- Thanks to the crew of the University of North Dakota's Citation II aircraft, and especially to Prof Mike Poellot, for their tremendous help and patience in collecting and pre-processing the cloud data for this study.
- Thanks to Daryl J. Onton of the University of Utah for providing MM5 forecast output. A portion of the CPI imagery was obtained through funding by NASA/EOS (contract number S-97894-F) to Dr. A. Heymsfield. NOAA-CIRES Climate Diagnostics Center, Boulder, Colorado, USA provided the 500-mb geopotential height maps at <http://www.cdc.noaa.gov>.
- This research was supported by the Air Force Institute of Technology and the Department of Defense Center for Geosciences/Atmospheric Research Agreement #DAAL01-98-2-0078.

And a very special thanks to my wife, [redacted], and to [redacted] and [redacted], who always do a great job of holding down the fort while I am out doing battle.

## Table of Contents

ABSTRACT OF DISSERTATION	iii
ACKNOWLEDGEMENTS	v
TABLE OF CONTENTS	vi
LIST OF FIGURES	vii
1. INTRODUCTION	1
2. INSTRUMENTATION	7
3. FLIGHT PATTERNS AND DATA PROCESSING	15
4. SYNOPTIC AND MESOSCALE SITUATIONS	19
5. MEASUREMENTS	25
6. COMPARISON OF FINDINGS WITH OTHER OBSERVATIONS	64
7. CLOUD PROCESSES	68
8. THE DEATH OF AN ALTOCUMULUS CLOUD	80
9. RADIATIVE EFFECTS AND SENSITIVITIES	93
10. SUMMARY & IMPLICATIONS FOR FORECASTING AND MODELING	145
11. CONCLUSIONS AND FUTURE WORK	159
12. REFERENCES	164

## List of Figures

- 1.1 Lagrangian racetrack pattern flown on 11 Nov 99. The aircraft drifted with a cloud parcel embedded in westerly flow (top) and the same track with the winds subtracted (bottom).
- 4.1 Satellite pictures and corresponding 500mb geopotential heights (dm) showing synoptic and mesoscale situations for (from top to bottom) 11 Nov, 2 Dec, and 4 Dec 99. Aircraft observation point is located roughly at the tip of the arrow.
- 4.2 Same as figure 4.1 except for 5 Dec 99, 10 Mar 00 and 12 Apr 00.
- 5.1 Cloud evolution diagram for the 11 Nov 99 case showing the relative time and height of the spiral soundings and subsequent racetracks. Measurements for the spirals are point values, while those for the flight legs are mean values of the diagram are temperature, liquid water content (lwc), pressure, horizontal wind direction and speed, and cloud fraction (CF). Light shading represents lower CF.
- 5.2 Same as the previous figure except for 2 Dec 99 Eulerian aircraft data.
- 5.3 Same as the previous figure except for 4 Dec 99. Again, the lighter shading represents lower CF due to inhomogeneous cloud areas, as pockets of drier air were mixed into this cloud. We also had problems moving the aircraft to the cloud on this day due to air traffic control delays when changing flight altitude.
- 5.4 Same as the previous figure except for 5 Dec 99.
- 5.5 Same as the previous figure except for the multi-layered cloud system on 10 Mar 00. Note that the original three layers devolved into two layers after about 18:31 UTC and the bottom layer ascended to a slightly higher height with time.
- 5.6 Same as the previous figure except for 12 Apr 00. Pressure and wind data were not available for this flight on the SPEC aircraft.
- 5.7 Vertical profiles of liquid and ice water content ( $\text{g m}^{-3}$ ) for the 11 Nov 99 single layer cloud case. To the right is a vertically consistent collage of CPI images, showing representative particles at the relative location they were measured in-cloud.
- 5.8 Same as previous figure except for 2 Dec 99. Note the change in scale; this cloud has half the lwc as the 11 Nov 99 cloud. Also, despite temperatures in the  $-27$  to  $-30^\circ\text{C}$  range, this cloud had very low amounts of iwc. This is mainly due to a low concentration of ice particles, as the sizes were generally larger than for 11 Nov 99.
- 5.9 Same as the previous two figures except for 4 Dec 99. This cloud was “psuedo-convective”, as it was detrained from convection upstream and then advected over the ARM site. The two discontinuities in lwc and iwc are a result of air traffic control delays of up to 15 minutes.

- 5.10 Same as previous three figures except for 5 Dec 99. This cloud was composed primarily of supercooled liquid droplets, despite temperatures of only  $-6$  to  $-8^{\circ}\text{C}$ . Dry air entrainment near cloud top caused a slight departure from the increase of lwc with height seen in figures 5.7-5.8.
- 5.11 Same as previous four figures except for multi-layered cloud on 10 Mar 00. Note the relatively low lwc values and the homogeneous vertical distribution of iwc.
- 5.12 Same as previous figure except for 12 Apr 00. Note the relatively high lwc, despite large amounts of ice. The higher total water content leads us to believe this cloud was more strongly forced than the 10 Mar 00 case. A seeder-feeder process is evident, with ice between the layers.
- 5.13 Droplet spectra for the single-layer cloud cases on 11 Nov 99 (top), 2 Dec 99 (middle), and 5 Dec 99 (bottom). Notice a shift to larger-sized liquid water droplets with height through each cloud. The concentrations also increase with height in each cloud except 5 Dec 99, when entrainment caused cloud top drying.
- 5.14 Same as figure 5.13, except for the multi-layered system observed on 10 Mar 00. Note the different vertical scales and the absence of droplet size and concentration with height, due to seeder-feeder processes and the presence of more ice particles in this system.
- 5.15 Same as figure 5.14, except for 12 Apr 00. The distribution of sizes with concentration is again fairly homogeneous. The increase at sizes greater than  $20\text{ }\mu\text{m}$  may be due to some contamination by larger ice particles in those bins.
- 5.16 Same as the previous two figures, except in this case the droplet spectra is a summation of the earlier plots for the total three cloud system.
- 5.17 Same as the previous four figures, except for ice concentration and size using 2D-C measurements, rather than FSSP liquid droplet spectra. Note the relatively small and rather homogeneous concentrations for all ice particle sizes.
- 5.18 Differences in vertical distribution of particle size and concentration between single layers (top) and multiple layers (middle and bottom). Note the increase in particle concentration at the bottom of the single layer cloud, the homogeneous distribution of both size and concentration in the 10 Mar 00 case, and the increase in size with decreasing altitude on 12 Apr 00.
- 5.19 Vertical profiles of temperature for four of the cloud cases, including the individual layers of the 10 Mar 00 case. Note the lack of temperature inversions at the cloud boundaries, particularly at cloud top.
- 5.20 Vertical profiles of virtual potential temperature for the same cases as Figure 5.19. This variable allows for slightly easier determination of mid-level cloud boundaries than temperature inversions, as there is a 1-2 K increase of  $\theta_v$  at cloud top (not seen at the top of the bottom and mid layers of 10 Mar 00 case).

- 5.21 Variation of ice water content with temperature for the five mixed-phase cloud cases. Highest values of iwc are between  $-8$  and  $-20^{\circ}\text{C}$ , corresponding to the maximum in both ice supersaturation and the growth rate of plate-like crystals centered at  $-15^{\circ}\text{C}$ . B, M and T denote bottom, middle and top of cloud, respectively.
- 7.1 Formative mechanisms and processes for mid-level, mixed-phase clouds. In this stage, a cloud is generally first formed by lifting a moist air layer until it cools and condenses, and then destabilized by vertical differential radiative heating and cooling processes. Evaporative cooling at cloud top and the release of latent heat further destabilizes the layer, causing internal circulations to develop. The added lift may increase the condensation supply rate, causing further cooling and more intense cloud circulations, but also increasing the dry air entrainment rate.
- 7.2 Maintenance processes for mid-level, mixed-phase clouds. In this stage, a delicate balance exists between the condensate supply rate, the bulk ice crystal growth rate, the dry air entrainment rate, and the amount of sedimentation. The circulation has to be strong enough to produce more liquid water, but not so strong that dry air is entrained too rapidly. The amount of ice nuclei also appears to be important for maintaining the cloud against rapid glaciation. Sedimentation of large ice from the base of the cloud may moisten the layer beneath by sublimation to the point where a new cloud layer is formed.
- 7.3 Dissipation mechanisms for mid-level, mixed-phase clouds include large-scale subsidence drying, loss of cloud water mass by excessive sedimentation of ice particles from the cloud, excessive dry air entrainment, or a change in the net radiative heating balance of the cloud. Differential vertical radiative heating is critical for maintaining cloud circulations, so if shortwave and latent heating overcome longwave and evaporative cooling at cloud top, the cloud will dissipate.
- 8.1 Time series of GOES-8 visible satellite images of the 11 Nov 99 cloud that coincides with the time of the CLEX-5 Lagrangian aircraft measurements. The focus of this part of the study was to determine the physical mechanisms responsible for the “death” of the mid-level, mixed-phase cloud shown at the tip of the arrow.
- 8.2 Cross-section of MM5 forecast vertical velocity ( $\text{cm s}^{-1}$ ) initialized 12 UTC on 11 November 1999. The air motion is upward at several  $\text{cm s}^{-1}$  at 1500 UTC, decreases to downward at about  $-3 \text{ cm s}^{-1}$  by 1800 UTC as the cloud starts to decay, and remains at  $-3 \text{ cm s}^{-1}$  by 2100 UTC, after the cloud dissipates.
- 8.3 The change in vertical velocity seen in Fig 8.2 is associated with an upper-level patch of high potential vorticity that breaks off from a trough and is advected eastward, as shown in the above MM5 forecast output. Mean 200-400 mb PV values decrease through the period from 1.1 at 15Z to just over 0.5 at 21Z.

- 9.1 BUGSRAD model lwc and iwc input profiles for (A) 11 Nov 99, (B) 2 Dec 99, (C) 5 Dec 99, (D) 10 Mar 00 and (E) 12 Apr 00. The model profiles use observed lwc and iwc values at 30 m vertical grid spacing and capture the main features of the observed profiles shown in Figures 5.7–5.12.
- 9.2 BUGSRAD model longwave and shortwave heating rates (A) and fluxes (B) for the 11 Nov 99 cloud case. Longwave plots are red; shortwave plots are blue. Note the strong longwave cloud top cooling rate of  $21.3 \text{ K hr}^{-1}$  at 5700 m due to flux divergence. In contrast, the shortwave heating rate of  $2.5 \text{ K hr}^{-1}$  is relatively small.
- 9.3 Same as Fig 9.2 except for 2 Dec 99 heating rates and fluxes. Note the different scales. The maximum lwc for this case is half that of 11 Nov 99, resulting in smaller longwave and shortwave heating and cooling rates.
- 9.4 Same as previous two figures except for 5 Dec 99. Despite having the largest maximum lwc of any case, the maximum cooling rate is a relatively modest  $3.4 \text{ K hr}^{-1}$ , because of a dry air entrainment-induced reduction in lwc at cloud top.
- 9.5 Same as the previous three figures except for the multi-layered cloud of 10 Mar 00. Small lwc and iwc values result in small amounts of flux convergence and divergence, which equates to small net heating rates.
- 9.6 Same as previous four figures except for 12 Apr 00. Despite relatively high amounts of lwc and iwc through this system, the maximum longwave cooling and shortwave heating rates are only  $2.7$  and  $1.3 \text{ K hr}^{-1}$ , respectively. This is due to lwc decreases at the top of the cloud and radiative interactions between the layers.
- 9.7 Results of a sensitivity study on the 12 Apr 00 case (Fig 9.6) showing the increase in heating rate (top) and flux (bottom) when the maximum lwc is located at cloud top (A,C) or the maximum iwc is located at cloud top (B,D). Note that the maximum longwave cooling approximately triples for (A) and quadruples for (B).
- 9.8 Sensitivity of longwave and shortwave radiative heating rate and flux to the amount of lwc for the 11 Nov 99 case. BUGSRAD model results for doubled and halved lwc are compared to the measured lwc value (see legend). Quantitative values and percent changes for the three plots are shown in Tables 9.1 and 9.2.
- 9.9 Same as previous figure except for 2 Dec 99 case. Longwave cooling and shortwave heating both occur at or near cloud top, while longwave heating occurs near cloud base. Note the change in scale, and refer to Tables 9.1 and 9.2 for the values of radiative heating and cooling when the lwc is doubled and halved.
- 9.10 Same as previous two figures except for 5 Dec 99. The variation of longwave cooling near the cloud top is due to the effects of dry air entrainment; the cooling rate associated with maximum lwc is at 2880 m, but decreasing amounts of lwc above that level interact with the fluxes to cause reduced cloud top cooling rates.
- 9.11 Same as previous three figures except for 10 Mar 00. Small lwc amounts ( $< 0.04 \text{ g m}^{-3}$ ) result in small flux changes and a small net heating rate. Note the change in scale from the other figures. Refer to Tables 9.1 and 9.2 for quantitative values of heating rate and the percent changes from the control case.

- 9.12 Same as previous four figures except for 12 Apr 00. Note the small changes in fluxes and heating rates when the lwc is doubled and halved; this is due both to decreasing lwc with height at the cloud top, similar to that seen in Fig 9.10 for the 5 Dec 99 case, and to the radiative interactions with adjacent cloud layers.
- 9.13 Same as Fig 9.8 except for sensitivity to iwc instead of lwc. The heating and cooling rate values and percent changes are shown in parentheses in Tables 9.1 and 9.2. Note the almost indiscernible changes in flux and heating rate when the iwc is doubled and halved, in contrast to the larger radiative interactions with lwc.
- 9.14 Same as previous figure except for 2 Dec 99 sensitivity to iwc. Again, note that there is very little impact to the fluxes and heating rates when doubling and halving the iwc, due to the relatively small amounts of ice in the bottom parts of the single-layer clouds.
- 9.15 Same as previous figure except for the 10 Mar 00 multi-layered case. The effects of doubling and halving the iwc are much more apparent here than in the previous two cases, because the cloud iwc was uniformly distributed and of the same order of magnitude as the lwc. Values are shown in Tables 9.1 and 9.2.
- 9.16 Same as previous figure except for 12 Apr 00. The sensitivity to iwc is also evident in this cloud, as the iwc values were relatively large and the ice particles were more evenly distributed with height than in the single-layer cases. For both multi-layer cases, heating rates changed 25-30% when iwc was doubled or halved.
- 9.17 Sensitivity of heating rate profiles to model parameterization of cloud phase. (A) shows the heating rate profile using the measured lwc and iwc values; (B) shows the same profile when the cloud is converted completely to ice, as it would be in current models that determine water phase by temperature.
- 9.18 Sensitivity of heating rate profiles to model parameterization of cloud phase. (A) and (C) show the observed heating and flux profiles using measured lwc and iwc values for 11 Nov 99; (B) and (D) show the same profile when the cloud lwc and iwc profiles are inverted in the vertical. This is another possible effect of using temperature to determine water phase, as iwc would increase toward cloud top.
- 9.19 Sensitivity of shortwave heating rate to solar zenith angle for 2 Dec 99. The black curve marks the observed heating rate and flux at the observation time; the other curves represent zenith angles as annotated in the diagram. Small angle changes after sunrise may offset nocturnal radiative cooling and cause dissipation.
- 9.20 Diurnal variation of mid-level clouds over North Dakota. The top panel shows percent frequency of occurrence of mid-level clouds versus time of day for September, October and November. The plots are derived from a three-hourly infrared ISCCP database over a ten-year period of record. The bottom panel shows the satellite-derived surface temperature over the same time period. Clouds increase overnight in response to radiative cooling but decrease after sunset, as net radiational cooling decreases in response to shortwave heating at cloud top.

- 9.21 Sensitivity of radiative heating rates (A, B) and fluxes (C, D) to changes or errors in cloud height. Plots A and C show the heating rates and fluxes at the actual measurement height, while B and D use the same cloud profile, but at 1 km lower height. The resulting heating rates are about  $1 \text{ K hr}^{-1}$  for the lower cloud.
- 9.22 Same as Fig 9.21 except at lower heights of 5.2 km (A,C) and 4.2 km (B,D). Note that smaller height differences between cloud base and the Earth's surface result in less heating at cloud base and cooling at cloud top, as forwarded by Stephens (1978). For this reason, cloud height accuracy is important for GCMs.
- 9.23 Sensitivity of radiative heating rates and fluxes to changes in cloud layering. The three-digit binary code corresponds to the layers included in each plot, i.e., only the top layer is included in "100". The 10 Mar 00 control case (all three layers) is shown in Figure 9.5 and is represented by a dashed line in each plot.
- 9.24 Same as Fig 9.23 except for cases in which only the bottom layer is included (001) and only the top and bottom layers are included (101). Note the longwave cooling in the bottom layer in the absence of intervening layers aloft.
- 9.25 Same as the previous two figures except for cases in which only the top two layers (110) and the bottom two layers (011) are included in the profile. The "110" profile in (A) nearly mirrors that of the observed case, while the longwave cooling in the middle layer dominates the "011" profile in (B).
- 9.26 Same as Fig 9.23 except for 12 Apr 00. In panel (A), note the longwave heating at the base of the top layer when removing the bottom layers. Likewise, panel (B) shows both radiative heating and cooling in the middle layer that was completely absent when all three layers were present.
- 9.27 Same as Fig 9.24 except for 12 Apr 00. Significant longwave cooling is apparent in (A) when the lowest layer is allowed to radiate without interacting with upper layers; from zero when layers are present to  $6 \text{ K hr}^{-1}$  when they are removed. The net radiative profile will change with time as layers develop and dissipate.
- 9.28 Same as Fig 9.25 except for 12 Apr 00. Note that the bottom of the lowest layer and the top of the top layer interact radiatively as if they were a single cloud layer. However, since the differential heating acts over a greater vertical distance with multiple layers, the radiatively driven circulations will be weaker.

# **1. Introduction**

## **1.1 Motivation and Background**

Mid-level, non-precipitating clouds are the “forgotten clouds” (Vonder Haar et al., 1997) in atmospheric science, often overlooked in favor of tropospheric studies of boundary layer stratus or upper-level cirrus clouds. The study of altocumulus cloud suffers neglect because they are not associated with severe weather and rarely produce precipitation that reaches the ground (Gedzelman, 1988). Yet there are important features of these clouds that need to be further scrutinized and understood. Warren et al. (1988) point out that altocumulus and altostratus are ubiquitous: together they cover 22% of the Earth’s surface. These clouds often extend through, or are completely above, the freezing level, giving rise to a mixture of liquid and ice microphysics. Matveev (1984) reported that more than 30% of clouds between  $-8$  and  $-26^{\circ}\text{C}$  were mixed-phase.

The precise mixture of liquid and ice may have important implications for cloud radiative transfer. As clouds changed phase from all liquid to all ice for a prescribed set of conditions, Sun and Shine (1994) reported optical depth variations from 28.2 to 2.9, with a corresponding change in albedo from 72.6% to 29.8%. In a related study of the radiation budget for the Tibetan Plateau in March, area mean planetary albedo decreased considerably from 40% to 36.5% when a mid-level cloud was changed from water to mixed-phase. According to the authors, “Assuming the ice to be in liquid form in

simulations commits a greater error than if ice is totally ignored.” Therefore, they called for refined observations of morphology and microphysical details of mixed-phase clouds.

If cloud radiative transfer is affected by mixed-phase microphysics, there will be an associated impact on the retrieval of cloud parameters from remote sensing devices. Phase is important in discerning whether absorption or scattering is the dominant extinction mechanism, while particle size and shape determine the type and amount of scattering. Accurate calculations of ice growth require precise knowledge of cloud particle habit (Korolev et al., 1999), which affects both the size and shape of the particle. Mason (1994) found that use of the wrong particle shape for calculating ice mass may result in errors as high as a factor of fifteen, and Mischenko et al. (1996) warn that use of the wrong particle shape in satellite retrievals of cloud optical thickness may result in an under- or overestimation of the cloud optical thickness by more than a factor of three.

A further motivation for refined measurements of mid-level, mixed-phase clouds is to provide improved data for the initialization of numerical weather prediction models. One significant lesson learned from Operations DESERT SHIELD and DESERT STORM was the difficulty of forecasting mid-level clouds, as they routinely covered target areas and hampered missions (Vonder Haar et al., 1997). There were also mid-level cloud impacts to military operations in the recent Balkans conflict. Uninhabited Aerial Vehicles (UAV) used the mid-altitudes for targeting, forward air control, and battle damage assessments, and were hampered by mid-level cloudiness. General rules of engagement for strike aircraft were to stay at or above 4500 m and to visually identify all targets. Due to mid-level cloudiness, aircraft often returned home without expending any ordnance. Furthermore, aircraft refuelings took place between 3000 and 5500 m, and

were often canceled due to clouds at this level. Finally, numerical weather prediction models generally failed to capture the areal coverage or longevity of mid-level clouds, impacting planning forecasts. Regarding civilian aviation, mid-level clouds restrict flight visibility, pose a possible icing hazard, and may cause light to moderate turbulence. In order to forecast mid-level clouds better, an improved understanding of their structure and evolution is needed.

Several agencies have realized the importance of utilizing mixed-phase cloud microphysics in their forecast models, including the European Centre for Medium-range Weather Forecasts (ECMWF). They have also highlighted some examples of model schemes for mixed-phase clouds that may be flawed. For example, results of two separate 10-day runs of the ECMWF model, one using all liquid and the other partitioned into ice and liquid, showed significant differences in various global mean quantities (Rockel et al., 1991). Tiedtke (1993) tested a prognostic cloud scheme in the global forecast model of the ECMWF, assuming latent heat released in clouds is applied uniformly to cloud air and environmental air, and defining clouds by volume-averaged cloud water and cloud ice contents. He also distinguished between cloud water and cloud ice solely on the basis of temperature. However, Hobbs and Rangno (1998) found ice particle concentrations were poorly correlated with temperature and, if anything, showed a decrease in concentration with decreasing temperature. Their analysis showed cloud phase to be more related to age than temperature, stating that, "On some occasions, clouds with temperatures as low as  $-24.5^{\circ}\text{C}$  were found to be virtually unglaciated, probably on account of small droplet sizes."

Literature on the actual structure of mid-level, mixed-phase clouds is relatively sparse. The findings that have been published can be divided into observational studies and modeling studies. Field (1999), Heymsfield et al. (1991), Hobbs and Rangno (1985,1998), Paltridge et al., (1986), Rauber and Tokay (1991), Tulich and Vonder Haar (1998), and Young et al. (2000) have all completed observational studies. These studies tend to tabulate the results of a few observed clouds, and then draw provisional conclusions about one or two aspects of the clouds from limited data. The most recent observations have been mainly of Arctic stratus (e.g., Pinto 1998), which is often mixed-phase, but tied to boundary layer processes different from those for mid-latitude, mid-level clouds that are decoupled from the surface.

In recent years, increased computing power has given rise to a limited number of mixed-phase cloud simulations from cloud-resolving models, such as Harrington et al. (1999), Liu and Krueger (1998), and Jiang et al. (2000). These studies will hereafter be referred to as H99, LK98 and J00, respectively. Both H99 and J00 focused on mixed-phase clouds, but they were boundary layer Arctic stratus, which are inherently different from mid-level, mid-latitude clouds. They forward the idea that a strong diurnal cycle of solar radiation is one major factor distinguishing mid-level, mixed-phase clouds from Arctic mixed-phase stratus. The H99 study provides some great insight and value, but it is purely hypothetical. The J00 simulation goes a step further than H99 by tying the model to actual clouds observed in Pinto (1998). LK98, on the other hand, models mid-level clouds in the mid-latitudes, but the clouds are liquid phase only. In summary, although there have been several studies of liquid-only clouds that exist at midlevels, and

several studies of Arctic stratus that are mixed-phase, few researchers have studied mid-level, mixed-phase clouds in detail.

## **1.2 Purpose**

This research describes an observational study of several mixed-phase, mid-level clouds that was recently completed during the Complex Layered Cloud Experiment (CLEX) field campaign. During the experiment, the University of North Dakota Citation II research aircraft took in-situ microphysical measurements of mid-level clouds over the central and northern Great Plains of the United States from 5 November through 5 December 1999. The flights yielded four cloud cases, designated as 11 Nov and 2, 4, and 5 Dec 99. The 11 Nov 99 case was a Lagrangian measurement (e.g., Passarelli, 1978; Bretherton and Pincus, 1995; Field, 1999) over east-central Montana, while the December cases were sampled over the Atmospheric Radiation Measurement (ARM) site in north-central Oklahoma. Additional measurements were obtained over the ARM site on 10 March 2000 (designated 10 Mar 00) and an opportunistic flight on 12 April 2000 (12 Apr 00) during a cloud Intensive Observing Period (IOP).

The main goal of this study is to characterize the morphology of these mixed-phase clouds in order to mould a conceptual picture of the microphysical and thermodynamic mechanisms that drive them, and to determine how this structure affects the radiative transfer. An overview of the instrumentation (Chapter 2) and aircraft sampling strategy (Chapter 3) precedes a discussion of the synoptic and mesoscale environments in which the mid-level, mixed-phase clouds were embedded (Chapter 4). A review of the resulting measurements (Chapter 5) includes a discussion of the

similarities and differences between single-layer and multi-layered clouds, as well as contrasts between mid-level and boundary layer clouds. The CLEX results are then compared with those obtained in previous studies of mixed-phase clouds (Chapter 6). Mid-level, mixed-phased cloud formation, maintenance and dissipation mechanisms are discussed and evaluated (Chapter 7) before performing a detailed study of the dissipation mechanisms that “killed” the cloud during the 11 November 1999 Lagrangian measurements (Chapter 8). A radiative transfer model is then described and used to determine radiative transfer through synthetic clouds created using the observed microphysics (Chapter 9). The findings are summarized along with a discussion of the implications of the research results for forecasting and modeling mid-level, mixed-phase clouds (Chapter 10). The conclusions and future work are listed in Chapter 11.

## **2. Instrumentation**

### **2.1 Overview**

Most of the microphysical measurements reported in this study were obtained aboard the University of North Dakota's Citation II research aircraft. The basic instrument package is described in Poellot et al., 1999, and includes measurements of temperature, dewpoint temperature, pressure, and cloud microphysics, along with aircraft position, attitude, and performance characteristics at a 25 Hz data rate. Winds are computed from measurements of airspeed, angle of attack and sideslip from a ported radome, and static pressure, aircraft velocity and attitude from an Inertial Navigation System, using the method of Lenschow (1986). The aircraft also carried Eppley pyrgeometers and pyranometers to measure the upward and downward shortwave and longwave broadband fluxes, and a forward-looking video camera to monitor visual conditions.

For our study, we focus on the cloud microphysical measurements, which were made with an array of Particle Measuring System (PMS) probes at a 4 Hz data rate, and a Cloud Particle Imager (CPI). The PMS probes include the Forward Scattering Spectrometer Probe (FSSP), one-dimensional (1D-C) and two-dimensional (2D-C) optical array imaging probes, and the King Liquid Water Probe. Each of the PMS instruments is described in detail in NCAR's Research Aviation Facility Bulletin 24 (Baumgardner, 1989). The 12 Apr 00 flight took place aboard a Learjet leased by

Stratton Park Engineering Company (SPEC). This aircraft had the same basic instrument package as described for the Citation II, including PMS and King probes, CPI, temperature, and altitude sensors. In contrast, however, the Learjet did not carry pressure or wind instruments, and analog data was recorded at the slower rate of 1 Hz. Since the PMS measurements are critical to our study, a detailed review of the instruments is given below and details of the major errors and corrections are listed in Tables 2.1a and 2.1b.

## **2.2 Forward-Scattering Spectral Probe (FSSP)**

The FSSP measures particles in the 2 to 47  $\mu\text{m}$  diameter range by relating the amount of light a spherical particle forward scatters to its size. FSSP concentrations are corrected for electronic delays and dead time following Baumgardner et al. (1985), while sizes are corrected for electronic response times using Baumgardner and Spowart (1990). These corrections minimize the two major limitations of FSSP measurements. The first limitation is that cloud particle concentrations are underestimated when particles are either coincident in the beam or pass through the sensing area of the probe during the electronic processing period of a previous particle. This factor produces a 10% error for concentrations greater than about  $300\text{ cm}^{-3}$ , which was very rarely observed in our measurements. The second limitation involves the sizing accuracy of the probe, which is affected by non-uniformities of the laser beam. These non-uniformities can cause errors in the amount of light that a particle scatters.

The response time of the electronics also causes several problems, including under-sizing of particles, detection of particles coincident in the beam as a larger single particle, and failure to discriminate between ice particles and liquid droplets. In fact,

**Table 2.1a Summary of King liquid water probe and Cloud Particle Imager measurement errors and associated corrections for CLEX-5 data.**

<b>King Aircraft Probe and CPI Measurement Errors and Corrections</b>		
<b>Sensor</b>	King Probe	CPI
<b>Type</b>	Hot-Wire	Digital Imager
<b>Measure</b>	Liquid water	2.3 $\mu\text{m}$ resolution
<b>Use</b>	Liquid water content	Ice crystal habit
	Cloud fraction	Degree of riming or sublimation Water phase discrimination
<b>Error</b>	Droplet break-up on wire	High airspeed
<b>Effect</b>	Underestimates lwc for droplets > 30 $\mu\text{m}$	Resolution limited to ~5 $\mu\text{m}$
<b>Correction</b>	Small droplets	None
<b>Error</b>	Responds to both liquid and ice	Image focus
<b>Effect</b>	Not calibrated with respect to ice, so lwc can be overestimated by ~20%	Difficult to distinguish liquid-ice
		Sizing errors
<b>Correction</b>	CPI cross-check	None
<b>Error</b>	Dry air response	
<b>Effect</b>	Ambient air cools hot-wire	
<b>Correction</b>	Apply offset to each flight leg	
<b>Error</b>	----- Small amounts of ice -----	
<b>Reduction</b>	Good qualitative agreement	Used as qualitative check for
	With the FSSP measurements	liquid and ice amounts
	----- Corrected for pitch and roll -----	

**Table 2.1b Same as Table 2.1a except a summary of aircraft FSSP, 1D-C and 2D-C probe measurement errors and associated corrections for CLEX-5 data.**

	<b>FSSP, 1D-C and 2D-C Aircraft Probe Measurement</b>		
	<b>Errors and Corrections</b>		
<b>Sensor</b>	FSSP-100	1D-C	2D-C
<b>Type</b>	-----	-----Spectrometers-----	-----
<b>Measure</b>	2-47 $\mu\text{m}$ diameter	25-600 $\mu\text{m}$ diameter	33-1056 $\mu\text{m}$ diameter
<b>Use</b>	Cloud discrimination Cloud fraction	Particle concentration	Ice particle size iwc calculations
<b>Error</b>	Elect.delay/deadtime	Electronic response time	Electronic response
<b>Effect</b>	Concs > 300 $\text{cm}^{-3}$ are underestimated by 10%	Particles pass through the array too quickly	Airspeed corrected to properly size particles
<b>Correction</b>	Baumgardner et al., 1985	None	Baumgardner, 1987
<b>Error</b>	Electronic response time	1-dimensional array	Particle size &
<b>Effects</b>	Sizing accuracy errors Non-uniform beam	No info on particle type, shape, or orientation	concentration (artifact rejection)
<b>Correction</b>	Baumgardner and Spowart, 1990	None	Cooper, 1978
<b>Error</b>	No phase discrimination	Small sample volume	High ice concentrations
<b>Effect</b>	Spurious sizes and concentrations	Statistically unrepresentative	Overloads data buffer
<b>Correction</b>	None	None	Low airspeeds and low ice concentrations
<b>Error</b>	-----	Small ice amounts -----	-----
<b>Reduction</b>	Not used for lwc		iwc based on large ice particle sizes compared to liquid droplet sizes
	Good qualitative agreement w/ King		
	-----	Corrected for pitch/roll -----	-----

Gardiner and Hallett (1985) describe FSSP particle size distributions in mixed-phase clouds as spurious, while McFarquhar and Heymsfield (1996) note the distributions are of poor quality when large non-spherical ice is present. However, recent laboratory investigations (e.g., Arnott et al., 2000) and comparisons with other particle counters (e.g. Poellot et al., 1999; Lawson et al., 2001) strongly suggest that the FSSP counts both small ( $< 50 \mu\text{m}$ ) ice particles and cloud drops with equal efficiency. Nonetheless, quantitative measurements are suspect in mixed-phase conditions, as errors in FSSP sizing are raised to the third power and can result in significant errors in lwc. For this reason, we only used the counts from this instrument to qualitatively determine whether we were in or out of cloud.

### **2.3 One-Dimensional (1D-C) Optical Array Imaging Probe**

The 1D-C Probe measures particles in the 25-600  $\mu\text{m}$  diameter range, by illuminating a linear array of photodiodes with a Helium-Neon laser. As a particle passes through the beam, a shadow image is cast on the diodes. The total number of occulted diodes then represents particle size. The limitations of this device include electronic response time errors if the particles pass too rapidly across the array; it cannot differentiate particle shapes, types, or orientation; and it may be statistically unrepresentative of cloud particle population due to a small sample volume and small concentrations of larger particles in the cloud.

## **2.4 Two-Dimensional (2D-C) Optical Array Imaging Probe**

The 2D-C probe measures particles from 33 to 1056  $\mu\text{m}$  in diameter. It is almost identical to the 1D-C probe, except shape and size can be discerned. 2D-C data are processed using artifact rejection criteria described in Cooper (1978). Both 1D-C and 2D-C particle sizes and concentrations are corrected for airspeed according to an algorithm provided by Baumgardner (1987). The main limitations of this probe are the distortion of images at airspeeds greater than  $132 \text{ m s}^{-1}$ , and a problem in high ice concentrations. The first limitation is not a factor for the Citation flights, as it flew at mean airspeeds of  $112 \text{ m s}^{-1}$ , but may have been a factor for the single Learjet flight, with mean airspeeds of  $150 \text{ m s}^{-1}$ . The other limitation involves a second buffer in the system becoming filled before the first buffer empties to the data system, causing an overload period in which the probe cannot take any more measurements. Ice concentrations were relatively low for our measurements, making this second effect negligible.

## **2.5 King Liquid Water Probe**

The King Liquid Water Probe is based on the design developed by King et al. (1978). It is a hot wire instrument that relates the change in resistance of a heated sensing wire to the amount of cooling caused by vaporization of cloud droplets. Specifically, the probe measures the amount of power necessary to maintain a heated element at a constant temperature while it is being cooled by convection and evaporation. The liquid water content (lwc) can be directly related to power consumption using a total energy equation.

The first limitation of this device is that when droplet diameters become greater than  $50 \mu\text{m}$ , droplets begin to break up on the sensing element and are removed by the

airflow before they totally evaporate, causing an underestimation of liquid water (Biter et al., 1987). This problem was minimized in our measurements by the existence of smaller cloud droplets in mid-level, mixed-phase clouds. The second limitation involves the fact that the probe responds to both water and ice, but is not calibrated with respect to ice, so caution must be used in mixed-phase conditions. This factor was minimized by the use of several probes for cross-checking values, and especially by utilizing the CPI.

A third factor that can affect lwc measurements using the hot-wire probes is the presence of large quantities of ice particles. Cober et al. (2000) found a “false lwc signal” of about 15–20% of the total ice mass when the hot-wire probe was operated at airspeeds of  $100 \text{ m s}^{-1}$ . This false signal increases to about 40% when the instrument is operated at airspeeds of  $200 \text{ m s}^{-1}$  (Strapp et al. 1999). This would suggest a maximum “false lwc signal” on the order of 25–30% for the Learjet on 12 Apr 00, and approximately 20% for the Citation cases, given the aircraft airspeeds mentioned earlier.

## **2.6 Error Reduction**

The lwc measurements between the King and FSSP probes show generally good qualitative agreement, with differences less than 35% most of the time. Different response times of the instruments and the FSSP sizing errors discussed earlier probably caused some of the same large momentary differences in lwc, as reported in Hobbs and Rangno (1998). To aid in the comparisons between the six cases, we elected to report lwc from the King probe, except for the 10 Mar 00 case where we use FSSP measurements due to a system failure of the King probe during that particular flight. Use of the King probe for most flights negated the need to correct FSSP lwc errors due to ice

contamination. Following Pinto (1998), a cloud is defined by King probe measurements of lwc exceeding  $0.005 \text{ g m}^{-3}$ . We further required that all of the liquid water probes indicate a sustained deviation from zero.

Because the King probe also has some limitations discerning liquid from ice particles, we utilized the CPI, a relatively new instrument that records high-resolution ( $2.3 \text{ }\mu\text{m}$ ) digital images of cloud particles and processes them “on the fly” (Lawson and Jensen, 1998). This instrument casts images of particles on a solid state, one million pixel CCD camera, and then freezes the motion of particles with a 20 ns pulsed, high-power laser diode. By identifying and sizing up to 1,000 particles per second, this technology allows for very precise characterization of particles at any point in time and space, helping to resolve qualitative questions regarding cloud phase. Since the CPI is a relatively new instrument, a thorough analysis of its response characteristics is a work in progress (Lawson et al., 2001). Our method for using the CPI to determine water phase is described in Chapter 5.

### **3. Flight Patterns and Data Processing**

We used three basic flight patterns in CLEX and the auxiliary data collections: a racetrack pattern over a fixed point, a Lagrangian racetrack, and a slow, spiral sounding. The racetrack is the basic sampling pattern. It involves a series of racetrack-shaped patterns at varying altitudes. For a typical cloud of one-kilometer thickness, we flew five racetracks at different altitudes: one above cloud, three in-cloud, and another below cloud. Rapid ascents/descents were made between racetracks. The straight and level portions of a racetrack are termed flight legs. Lagrangian racetracks were displaced horizontally from one another so the aircraft drifted with the wind at various levels in the cloud, as shown in Figure 3.1 for the 11 Nov 99 flight. We sampled the wind speed and direction during the first mid-cloud racetrack and used this information to determine the horizontal position of subsequent racetracks, so that we stayed in the same relative cloud parcel for the duration of the measurement time.

Airspace restrictions prevented us from making Lagrangian measurements over the Southern Great Plains ARM site for the cloud cases on and after 2 Dec 99. For this reason, we sampled clouds over the ARM site while centered at a fixed latitude and longitude, with the longer dimension of the racetrack approximately 20 km in length. The in-cloud legs of a given racetrack were chopped to ensure they were contained entirely within a uniform cloud region. Above and below cloud racetracks were made 100-200 m away from the cloud so that they occurred entirely within clear air. The

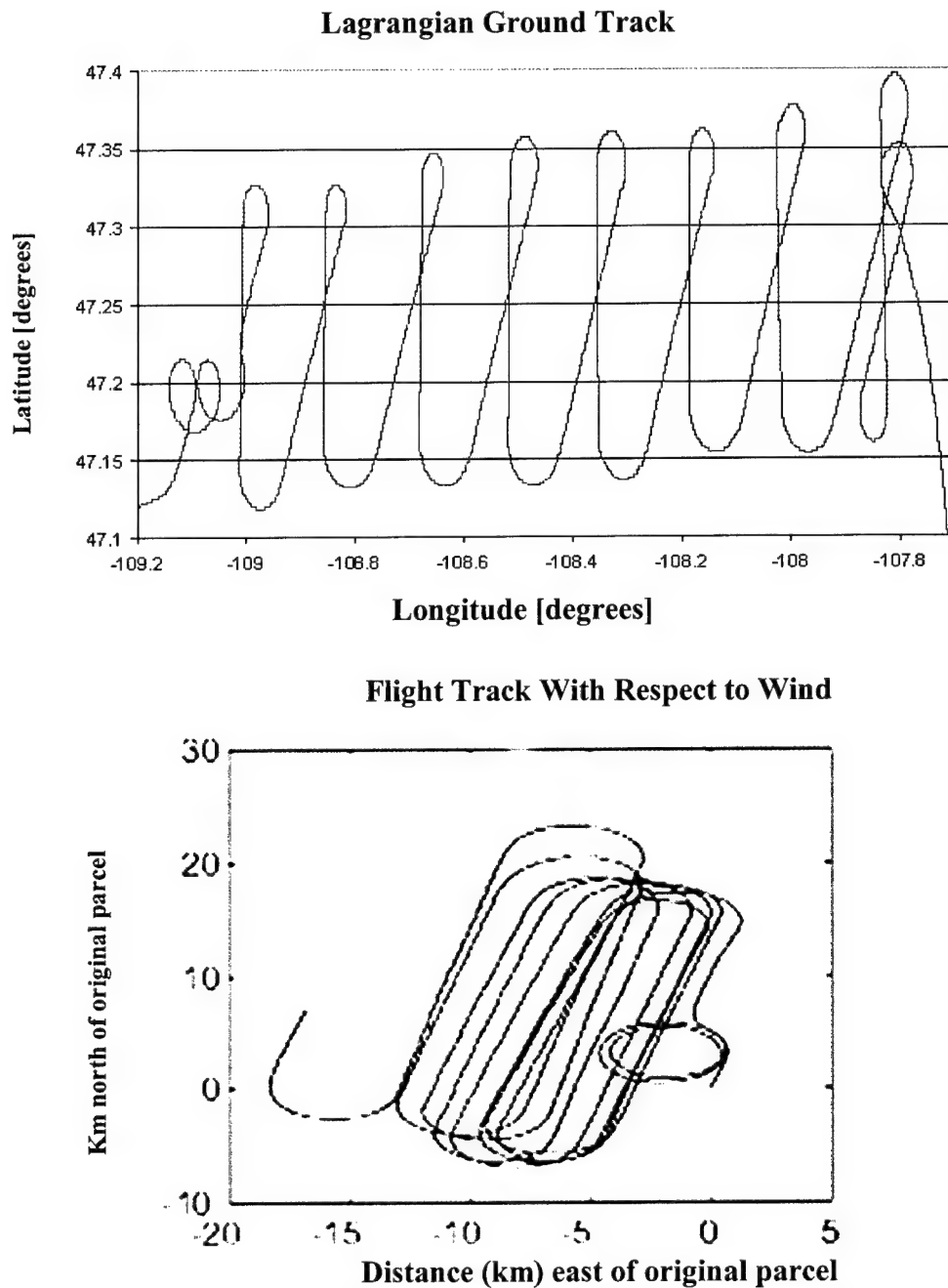


**Fig 3.1 Lagrangian racetrack pattern flown on 11 Nov 99. The aircraft drifted with a cloud parcel embedded in westerly flow (top) and the same track with the winds subtracted (bottom).**

highest racetrack within cloud was made just enough below cloud top to ensure the racetrack was entirely within cloud. Similarly, the lowest racetrack within cloud was just above cloud base. The racetracks within cloud were vertically separated by 200-500 m, depending on cloud depth. Due to limited upper-air data, and the desire to get vertical samples of the clouds, the aircraft performed slow spiral descents for a thermodynamic sounding. The typical aircraft sounding extended from a few hundred meters above cloud top to about the same distance below cloud base. The aircraft rate of ascent or descent for these profiles was constant at  $300 \text{ m min}^{-1}$ .

Aircraft data were processed to eliminate pitch, roll and yaw effects, so that only straight and level flight legs remained. To correct for the cooling effects of dry air on the King hot wire probe, offsets were determined for each leg by noting measurements in the ambient air outside of cloud at the same airspeed and air density. The offsets were checked for consistency at every flight level and then subtracted from the measured values. Since the correction amount varies with air density, the final vertical profile of King lwc from the spiral soundings had to be adjusted slightly. This was accomplished by using a simple linear correction formula, which effectively zeroed the profile in non-cloud regions.

During our preliminary analyses of the flight data, we found there were certain legs over the ARM site where we were in and out of cloud. For example, a cloud may have been advecting into the western part of the 20-km racetrack area, while it was still clear air on the eastern end. To account for these horizontal inhomogeneities in a given racetrack, we computed the mean time-weighted in-cloud liquid water content for each flight leg. For example, a racetrack may have been composed of flight legs 1a, b, and c.

The mean time-weighted in-cloud lwc would be the summation of each flight leg's time divided by the total time of all three flight legs, multiplied by the mean liquid water content of the individual flight legs. This is more readily apparent mathematically:

$$\overline{lwc} = \left( \frac{t_{1a}}{t_{1a} + t_{1b} + t_{1c}} \right) (lwc_{1a}) + \left( \frac{t_{1b}}{t_{1a} + t_{1b} + t_{1c}} \right) (lwc_{1b}) + \left( \frac{t_{1c}}{t_{1a} + t_{1b} + t_{1c}} \right) (lwc_{1c})$$

where  $t$  is time in-cloud; 1a, 1b, and 1c are flight legs; and lwc is liquid water content.

Ice water content (iwc) was calculated using the method of Mitchell et al. (1990) (hereafter referred to as M90), which is one of several papers that give dimension to mass relationships. Because our spiral descents contained a mixture of aggregates, dendrites, hexagonal plates, columns, bullets, etc., we chose the “all snow types” formulation from M90 for the clouds sampled in this study. Several papers (e.g., M90, Heymsfield and Platt (1984), and Heymsfield and Parrish (1986)) discuss the large uncertainties in iwc calculations, including assumptions about the physical characteristics of the ice particles.

Two important caveats must be made concerning the iwc calculations (Lawson, 2001, personal communication). First, the sampling statistics for the larger particles are poor, but are the most influential in the computation of iwc; Poisson statistics for 1 Hz measurements suggest a 25 to 50% uncertainty due to sampling. Second, the larger particles may not be sampled as reliably as the smaller particles, but the larger particles strongly influence the iwc calculation. Since the M90 computations were used exclusively in this study, the comparisons and trends are one-to-one; this may not be true if comparing our results with studies that use a different method to compute iwc.

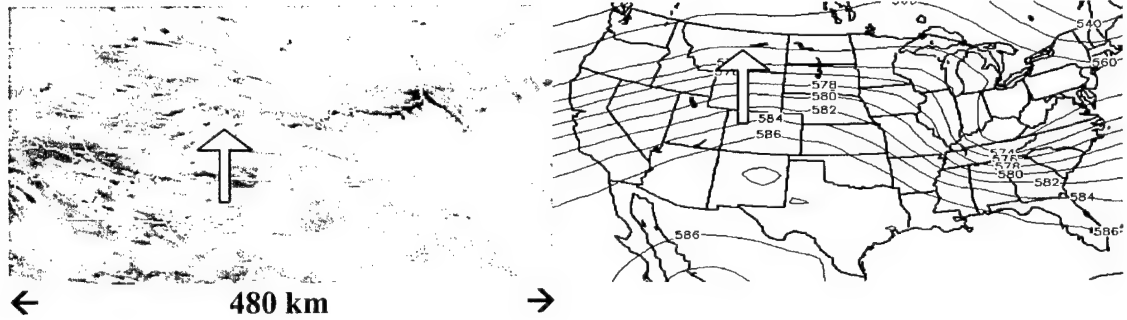
## **4. Synoptic and Mesoscale Situations**

Satellite images of each of the clouds we sampled are shown in Figures 4.1 and 4.2, along with the corresponding 500-mb geopotential height maps. All of the clouds formed in regions of large-scale ascent associated with an upper-level disturbance. A description of the synoptic and mesoscale situation for each cloud follows in the paragraphs below.

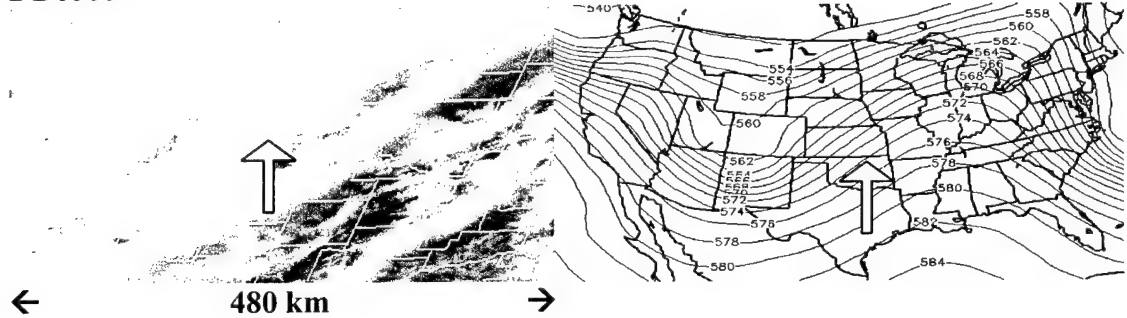
### **4.1 11 Nov 99**

A large area of mid- and upper-level cloudiness advected eastward along the Wyoming-Montana border, about halfway between Casper, WY and Great Falls, MT. The cloud area marked the northern end of a very strong upper-level ridge axis, with the high- pressure center located over Mexico. The surface high was near the four-corners region of the US. A potential vorticity (PV) patch, associated with an upper-level shortwave on the US-Canadian border, moved across northern MT and enhanced the early morning clouds beginning around local noon. Our Lagrangian aircraft sample took place between 1923 and 2040 UTC, as the cloud field was dissipating; the system had already crested the ridge axis and was losing the support of the PV maximum, which was moving east of the measurement area.

11 Nov 99



2 Dec 99



4 Dec 99



**Fig 4.1 Satellite pictures and corresponding 500mb geopotential heights (dm) showing synoptic and mesoscale situations for (from top to bottom) 11 Nov, 2 Dec, and 4 Dec 99. Aircraft observation point is located roughly at the tip of the arrow.**

## **4.2 2 Dec 99**

Bands of mid- and upper-level cloud, associated with a deep upper-level trough that extended from the Dakotas to the southern tip of the Baja Peninsula, moved across the TX Panhandle and into northern OK. These clouds were east of a dry air slot over NM and southern CO. The dry slot eventually moved into the area and helped fire pre-frontal convection ahead of a slow-moving cold front that was situated from south central MN to southern NM. The 300-mb winds were SSW at 70 kts at the ARM site, as the central core of a 100-kt jet stream developed over northeast TX. We sampled a pre-frontal mid-level cloud band as it moved over north central OK from 1453 to 1605 UTC.

## **4.3 4 Dec 99**

Frontal passage on the evening of 3 Dec 99 generated a significant amount of convection, with thunderstorms over northern and eastern OK lasting throughout the night. The storms included some severe cells, with five tornadoes reported in a triangular area between Ponca City, Tulsa and Oklahoma City, OK. Light to moderate rain continued through the morning and early afternoon hours, but stopped by mid-afternoon. Mid-level, “pseudo-convective” clouds moved into the area from the west-southwest at that time, prompting a flight over the ARM site from 2030 until 2207 UTC (we use the term pseudo-convective here to indicate that the mid-level cloud formed as a result of convection upstream of our aircraft measurements. The cloud was well mixed by convective turbulence, which distinguishes it from the other clouds in this study, but was non-convective and stratiform in appearance during the sample time). A stratus cloud

deck with a base of about 650 m was evident beneath the mid-level cloud layers. The jet core was directly over the ARM site during this time, with winds in excess of 100 kts.

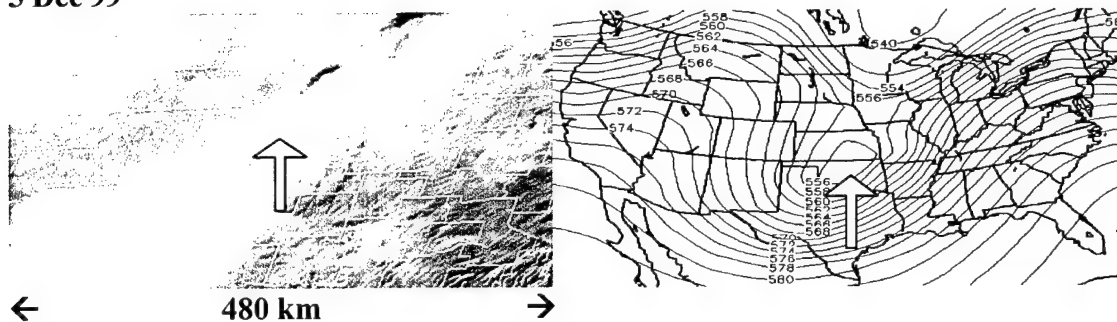
#### **4.4 5 Dec 99**

An upper-level low-pressure center moved just north of the OK border behind the strong surface system that preceded it on the evening of 4 Dec 99. Snow fell overnight, with light flurries lingering into the early morning hours. Ponca City, OK was on the western edge of a “wrap-around” cloud field, with non-precipitating low- and mid-level clouds over the ARM site. We sampled this system for approximately 45 minutes, from 1430 to 1515 UTC, until it moved east of the flight area. The 300-mb winds were northerly at approximately 30 kts. The mid-level cloud extended from 2390 to 3002 m, with a stratus cloud layer observed beneath it from 1400 m to 2200 m.

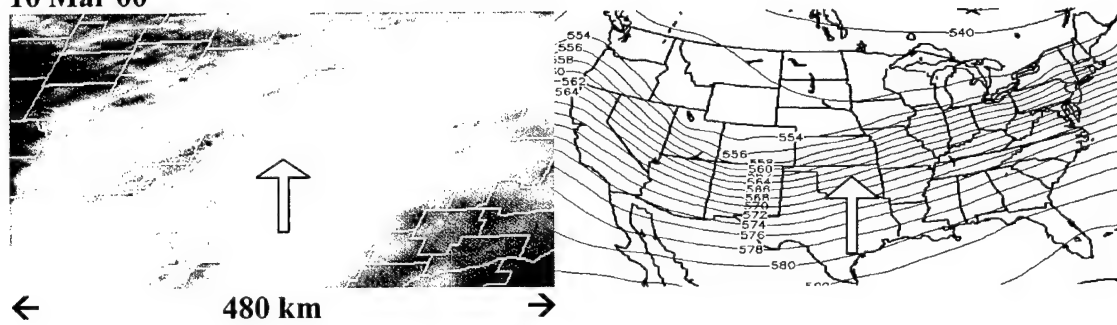
#### **4.5 10 Mar 00**

Mid-level cloudiness on 10 March 2000 was associated with ascent forced by an upper-level trough that moved from the Front Range of the Rocky Mountains into the western Great Plains during the day. A 90-kt jet stream flowed from the TX panhandle, across OK and into the Ohio River Valley, helping to support the system. It also brought southwesterly flow over an 850-mb low-pressure center in southern OK, and a quasi-stationary surface low that was located just south of the TX-OK border. This large-scale setting generated a thick layer of cirrus cloud over the ARM site, and eventually evolved into the multi-layered, mid-level cloud that was sampled between 1713 and 1939 UTC.

5 Dec 99



10 Mar 00



12 Apr 00

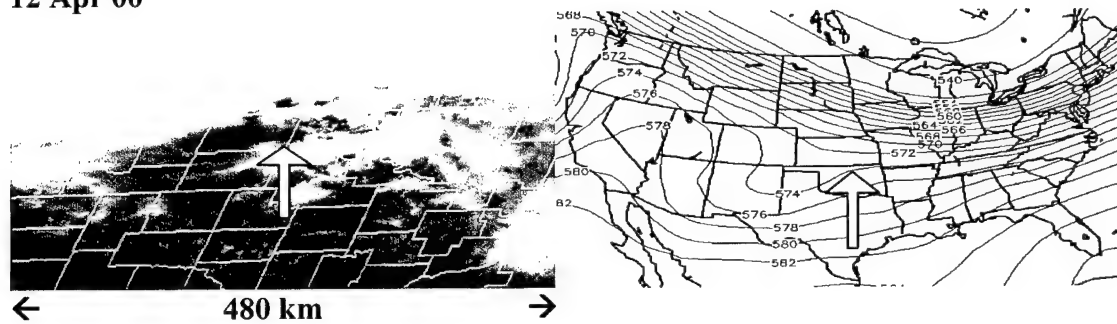


Fig 4.2 Same as Figure 4.1, except for 5 Dec 99, 10 Mar 00 and 12 Apr 00.

#### **4.6 12 Apr 00**

The synoptic situation for this case was very similar to the one described for 10 Mar 00. An upper-level low was again resident over the TX panhandle, although it was somewhat weaker. The main jet stream extended up and across the northern tier of the U.S., with a weaker 55-kt jet streak wrapped around the southern end of the upper-level low, across the panhandle region and into northeastern OK. A strong surface ridge of high pressure extended from the Great Lakes southwestward into east central OK, where it clashed with a quasi-stationary frontal boundary that extended northward from a surface low-pressure center near Houston, TX. In addition to being a similar synoptic situation to the 10 Mar 00 case, it also generated a similar three-layer cloud system. We sampled this cloud with the SPEC Learjet from 1700 to 1810 UTC.

## **5. Measurements**

### **5.1 Summary of Mean Observed Microphysical Parameters**

The mean measurements taken within the mid-level clouds we sampled are summarized in Table 5.1. Figures 5.1 through 5.6 show the basic measurements (temperature, liquid water content, pressure, winds and cloud fraction (CF)) at the relative time and location where they were observed with respect to the cloud. The measurements for the spirals are point values, while those given for the flight legs are mean values.

Mixed-phase conditions were evident in five of the six cloud systems, ranging in altitude from 2390 m to 7220 m. The 5 Dec 99 cloud was entirely above the freezing level, with a mean temperature of  $-7^{\circ}\text{C}$ , but consisted solely of liquid water. The highest lwc values of all observed clouds were found at the top of this cloud, possibly due to the lack of ice. The synoptic conditions were somewhat similar for the cloud cases after 11 November 1999, which were all measured over the ARM site in north central OK. The first four cases chronologically were all single-layer clouds, while the clouds on 10 Mar and 12 Apr 00 consisted of multiple layers. Three of the single-layer clouds were approximately 600 m thick, while the pseudo-convective cloud on 4 Dec 99 was 1500 m thick. The multi-layered systems each covered about 3000 m in vertical extent, with

**Table 5.1** Mean values of measurement location, height, pressure (p), temperature (T), time-weighted in-cloud liquid water content (lwc), standard deviation of lwc ( $\sigma_{lwc}$ ), horizontal wind direction and speed, and standard deviation of the vertical wind ( $\sigma_w$ ) for the 11 Nov, 2 Dec, 4 Dec, 5 Dec 99 and 10 Mar 00 cases, respectively. T, M and B signify cloud top, middle and bottom. I/O denotes in/out of cloud. 12 Apr 00 means are missing, as several instruments failed just after the sounding.

Mission Case Day	Leg #	Location	Height [m]	p [mb]	T [°C]	lwc [g m <sup>-3</sup> ]	$\sigma_{lwc}$ [g m <sup>-3</sup> ]	Dir [deg]	Speed [m s <sup>-1</sup> ]	w [m s <sup>-1</sup> ]	$\sigma_w$ [m s <sup>-1</sup> ]
11 Nov 99	1	Under	4525	575	-8.3	0.002	0.002	268	23.8	0.58	0.23
	2	In (B)	5279	520	-13.9	0.026	0.024	266	26.3	1.17	0.74
	3	In (T)	5608	498	-16.4	0.143	0.064	269	26.5	0.59	0.64
	4	Above	5794	485	-16.3	0.000	0.000	270	24.5	1.02	0.29
	5	In (M)	5546	502	-15.8	0.103	0.058	270	26.1	0.60	0.68
	6	In (M)	5434	510	-14.9	0.051	0.031	271	25.6	2.17	0.84
	7	In (B)	5182	527	-12.7	0.012	0.004	271	25.5	2.87	0.50
	8	Below	4877	549	-10.0	0.007	0.003	273	25.8	1.22	0.63
2 Dec 99	1	Above	8238	344	-37.5	0.000	0.000	242	27.8	-0.32	0.16
	2	In (B)	6711	428	-27.1	0.013	0.012	204	24.0	-0.24	0.59
	3	In (T)	7008	410	-29.7	0.057	0.018	205	25.2	0.14	0.74
	4	Above	7314	393	-30.2	0.000	0.000	212	26.9	-0.09	0.15
	5	Out (M)	6969	412	-27.8	0.000	0.000	209	24.6	0.00	0.21
	6	I/O (M)	6892	417	-27.8	0.009	0.002	206	27.4	-0.21	0.22
4 Dec 99	1	Above	6712	428	-27.8	0.000	0.000	185	51.2	-0.20	0.50
	2	In (M)	5199	526	-18.9	0.026	0.014	189	32.0	-0.14	0.32
	3	I/O (M)	4899	548	-16.4	0.004	0.005	193	33.4	0.01	0.37
	4	Turns	---	---	---	---	---	---	---	---	---
	5	I/O (M)	4903	547	-17.0	0.008	0.006	191	31.7	-0.48	0.68
	6	I/O (B)	4288	594	-13.1	0.029	0.025	187	20.1	-0.45	0.63
	7	I/O (B)	4291.5	593	13.3	0.038	0.013	187	21.2	1.46	0.71
5 Dec 99	1	In (M)	2592	738	-7.1	0.074	0.024	347	19.55	0.63	0.25
	2	I/O (M)	2592	738	-6.9	0.085	0.031	352	20.5	0.63	0.23
	3	In (B)	2390	757	-6.5	0.129	0.055	344	18.0	0.11	0.34
	4	In (M)	2625	735	-7.2	0.093	0.031	354	24.1	0.79	0.16
	5	I/O (T)	2810	718	-7.8	0.051	0.017	345	19.3	0.83	0.18
	6	Below	2386	758	-5.9	0.000	0.003	351	19.95	0.95	0.26
10 Mar 00	1	Above	6408	446	-27.4	0.002	0.003	233	28.2	-0.02	0.22
	2	In (M)	3309	674	-6.3	0.012	0.011	0	8.9	0.14	0.31
	3	In (T)	3375	668	-6.6	0.051	0.032	190	10.2	0.10	0.28
	4	In (M)	3316	673	-6.1	0.021	0.012	0	9.8	0.02	0.02
	5	I/O (M)	5482	506	-20.9	0.012	0.011	219	26.3	0.05	0.31
	6	In (T)	5594	499	-21.9	0.050	0.037	199	27.1	0.28	0.44
	7	In (M)	5517	504	-21.3	0.029	0.024	174	27.3	0.94	0.31

internal layers of 400 to 900 m in depth. Temperatures varied from a near-freezing value of  $-0.9^{\circ}\text{C}$  to a low of  $-30.3^{\circ}\text{C}$ . Mean liquid water content values were on the order of  $0.01$  to  $0.15\text{ g m}^{-3}$ , with a maximum point value of  $0.35\text{ g m}^{-3}$ . Horizontal winds were from the south through west at approximately  $20\text{--}30\text{ m s}^{-1}$  for all clouds except 5 Dec 99, which was situated in northerly flow. The standard deviation of the vertical wind was highest throughout the 11 Nov and 4 Dec 99 clouds, as well as the top of the 2 Dec 99 cloud, indicating greater turbulent mixing in these cases.

As mentioned previously, the 11 Nov 99 case was a Lagrangian sample, so the aircraft remained in the same cloud column with time and measured the evolution of the various microphysical parameters as it drifted in a westerly flow at approximately 25 kts. The flight legs are in chronological order, so note the temporal changes in the various quantities during the 75 minutes prior to cloud dissipation. In-cloud temperatures ranged from about  $-12.5$  to  $-16.5^{\circ}\text{C}$  through a cloud depth of 525 m. Highest values of lwc ( $0.30\text{ g m}^{-3}$ ) were found in the upper portion of the cloud during the initial spiral, while the mean values for each flight leg varied from a maximum of 0.14 to less than  $0.02\text{ g m}^{-3}$  at cloud base. The mean iwc for the aircraft sounding was  $0.02\text{ g m}^{-3}$  with a maximum of  $0.24\text{ g m}^{-3}$  found eight meters above cloud base.

The Eulerian nature of the remaining measurements over the ARM Site caused some inhomogeneities in the measured fields; racetrack patterns were flown through cloud fields that were advecting through the area and changing with time. The north-south distance between successive legs was on the order of 10-12 km. Each of these factors may have contributed to some quantitative differences in the various microphysical values, due purely to sampling considerations within a given racetrack.

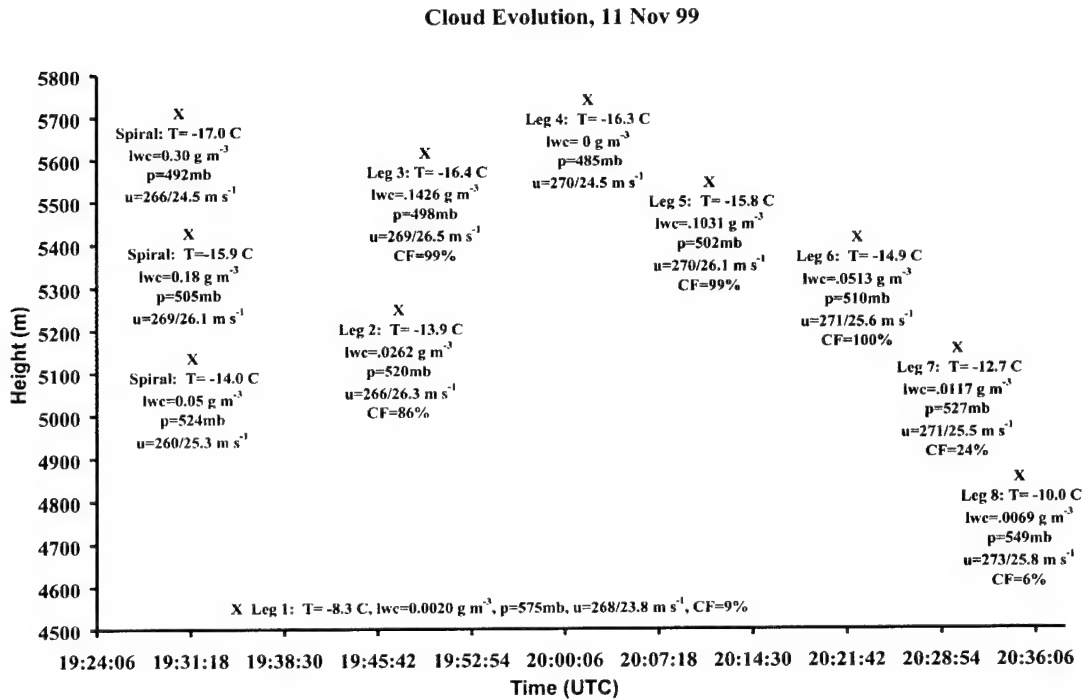


**Figure 5.1** Cloud evolution diagram for the 11 Nov 99 case showing the relative time and height of the spiral soundings and subsequent racetracks. Measurements for the spirals are point values, while those for the flight legs are mean values of the diagram are temperature, liquid water content (lwc), pressure, horizontal wind direction and speed, and cloud fraction (CF). Light shading represents lower CF.

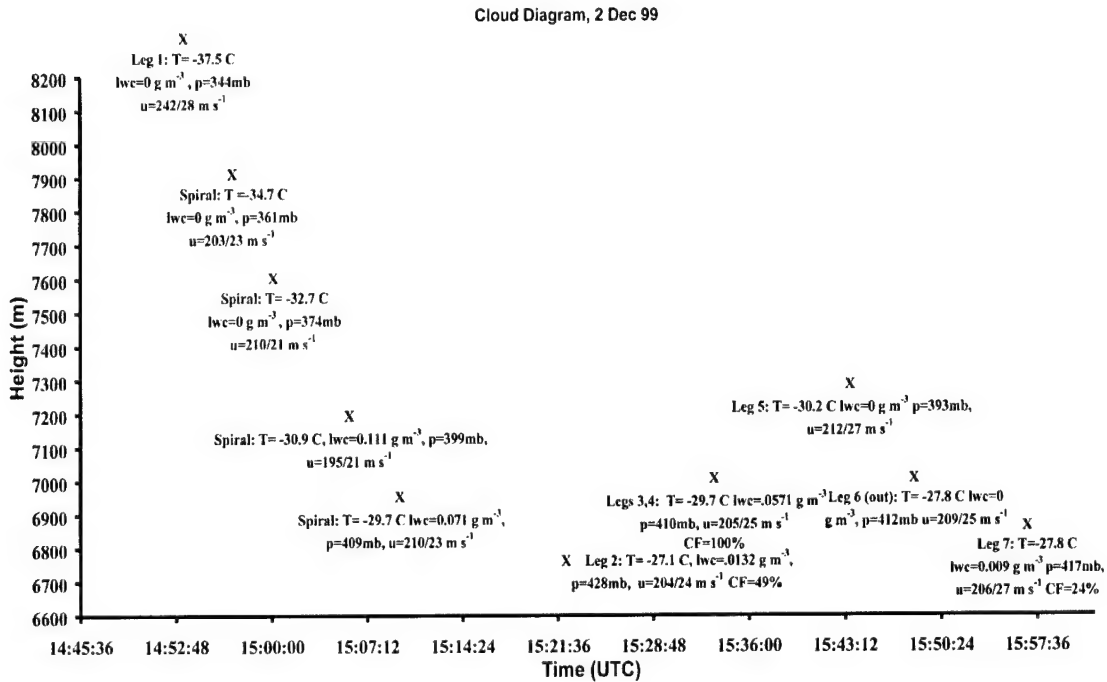


**Figure 5.2** Same as the previous figure except for 2 Dec 99 Eulerian aircraft data.

The cloud on 2 Dec 99 was  $15^{\circ}\text{C}$  cooler than the previous case, with temperatures ranging from  $-26.5$  to  $-30.3^{\circ}\text{C}$  through a cloud depth of just over 600 meters. Liquid water contents were about half of those measured on 11 Nov 99, with a maximum of  $0.14\text{ g m}^{-3}$ . Mean values were substantially lower, with  $0.01\text{ g m}^{-3}$  in leg 2 and  $0.06\text{ g m}^{-3}$  in both legs 3 and 4. The mean iwc for the aircraft sounding was slightly less than  $0.01\text{ g m}^{-3}$  with a maximum of  $0.037\text{ g m}^{-3}$  found 30 m above cloud base. The vertical wind field shows very little upward motion throughout the sample time, in contrast to the relatively large upward motions seen in the 11 Nov 99 cloud. Horizontal winds were more SSW, but the speeds were roughly the same as the aforementioned case.

Temperatures in the 4 Dec 99 case ranged from  $-13$  to  $-23^{\circ}\text{C}$ . The system was approximately 1500 m deep, which is two to three times that of the other single-layer clouds. Mean liquid water contents were similar to the 2 Dec 99 cloud, with values ranging from a low of  $0.004\text{ g m}^{-3}$  in leg 3a to a maximum around  $0.04\text{ g m}^{-3}$  in legs 6d and 7b. The mean iwc for the aircraft sounding was slightly less than  $0.10\text{ g m}^{-3}$  with a maximum of  $0.84\text{ g m}^{-3}$  found within 100 m of the cloud base. Interestingly, the vertical wind field shows mostly downward motion throughout the sample time, except for flight legs 3a, 7 and 7b.

Cloud temperatures in the 5 Dec 99 case are the warmest of the single-layer clouds, with a mean of  $-6.5^{\circ}\text{C}$  and a range of  $\pm 1^{\circ}\text{C}$ . Cloud depth was on the order of 600 m, similar to the first two cases. Liquid water contents were fairly high and similar to the Montana case, with mean values of  $0.05$  to  $0.14\text{ g m}^{-3}$ . The maximum lwc of  $0.35\text{ g m}^{-3}$  was found about 190 m below cloud top. High values could possibly be due to the lack of ice in this cloud; only one particle was evident in CPI images. Although this



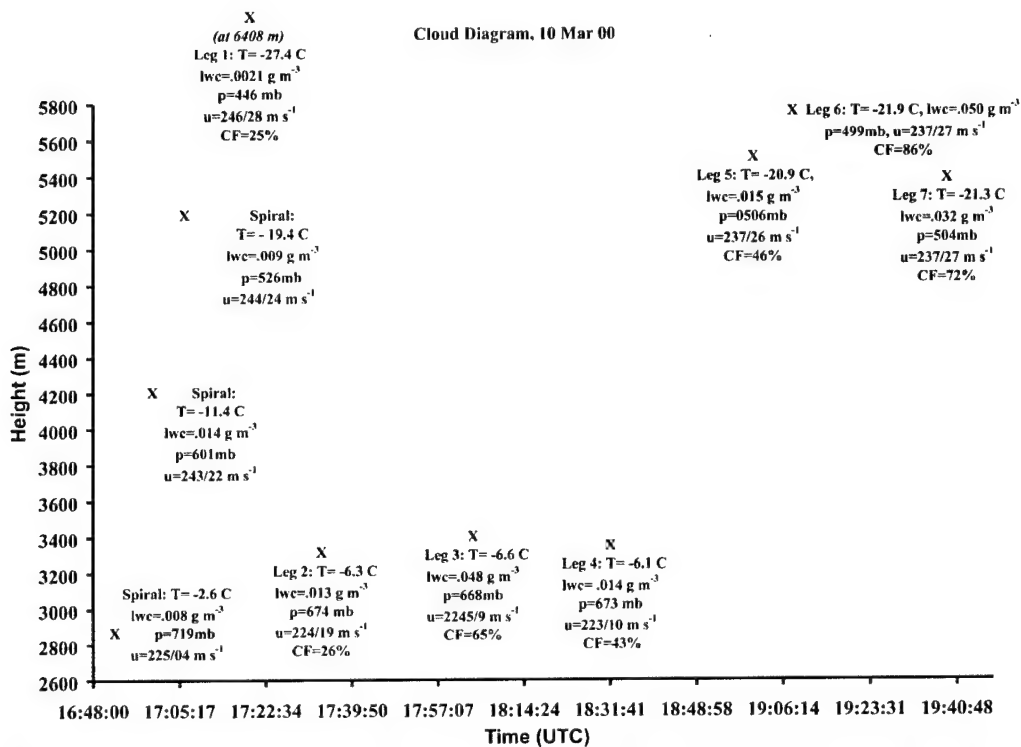


**Figure 5.5** Same as the previous figure except for the multi-layered cloud system on 10 Mar 00. Note that the original three layers devolved into two layers after about 18:31 UTC and the bottom layer ascended to a slightly higher height with time.

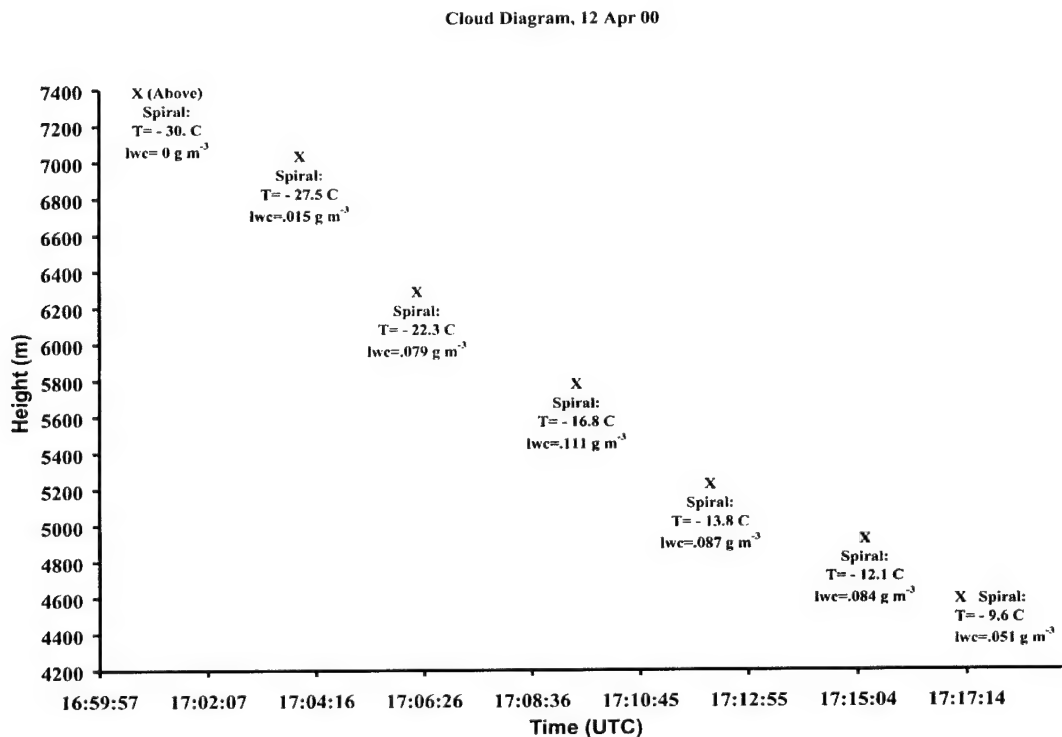


**Figure 5.6** Same as the previous figure except for 12 Apr 00. Pressure and wind data were not available for this flight on the SPEC aircraft.

cloud was post-frontal, vertical motion was upward and on the order of  $0.5 \text{ m s}^{-1}$  while the cloud persisted.

Clouds on 10 Mar and 12 Apr 00 were multi-layered, mixed-phase cloud systems. The 10 Mar 00 system extended from 2600 to 5594 m, with individual layers between 400 and 750 m deep. The temperature range was from about the freezing point to  $-22^\circ \text{C}$ , with SW winds varying from  $9 \text{ m s}^{-1}$  near the base to over  $27 \text{ m s}^{-1}$  in the top layer. Mean lwc values ranged from 0.01 to  $0.05 \text{ g m}^{-3}$ . The mean iwc for the aircraft sounding was slightly more than  $0.01 \text{ g m}^{-3}$  with a maximum of  $0.05 \text{ g m}^{-3}$  found in the top layer of the cloud system. The 12 Apr 00 cloud was nearly 2000 m higher, with a vertical range from 4300 to 7275 m, and layers 700 to 1000 m deep. The mean lwc was  $0.08 \text{ g m}^{-3}$  through the depth of this cloud, in temperatures that ranged from  $-8.1$  to  $-29.3^\circ \text{C}$ . The mean iwc of  $0.22 \text{ g m}^{-3}$  during the aircraft sounding was the highest of any cloud measured. The maximum iwc was  $0.78 \text{ g m}^{-3}$ , found in the middle part of the lowest layer of this system.

The analysis of the mean microphysical fields leads to several questions concerning cloud structure. First, how is the liquid and ice distributed vertically in mixed-phase clouds? What are the microphysical differences between single- and multi-layered mid-level cloud systems? What is the supporting role of the CPI data for mixed-phase studies? Do wind shears, temperature inversions, or other microphysical discontinuities play a role in the observed structure? Finally, how do our observations compare to measurements of similar clouds by other authors? These questions will be discussed in the following subsections and in Chapter 6.

## 5.2 Liquid and Ice Water Content Profiles

Plots of liquid and ice water contents for each cloud case were constructed using the King lwc and 2D-C ice concentration and particle size measurements from aircraft sounding spirals, as shown in Figures 5.7 through 5.12. Beside each plot is a vertical profile of representative CPI particle images, positioned in the graph relative to where they were found in the cloud field.

Before closer inspection of individual cases, a few general observations should be noted. The most striking feature of these plots is the increase in lwc with height in the single-layer cases and, to a lesser degree, in the individual layers of multi-layered clouds. In most cases, the lwc is a maximum at cloud top. An exception occurs for 5 Dec 99, when lwc peaks about 190 m below cloud top. In this latter case, it appears that a small temperature inversion may have decoupled the uppermost portion of the system, subjecting that part of the cloud to more dry air entrainment from aloft. This process will be discussed in more detail later. Ice water content is a maximum near the base of single-layer clouds, whereas it is more evenly distributed in the vertical for the multi-layered cloud systems. It is interesting to note that Pinto (1998) saw the same lwc and iwc structure in mixed-phase, boundary-layer Arctic stratus clouds that we observed in single-layer, mid-level clouds.

The profiles for 11 Nov and 2 Dec 99 clouds look very similar in shape, but there are some significant differences. The lwc in the first case is nearly twice that of the latter case, and the temperature is about 14° C warmer. Despite having a lower lwc, the 2 Dec 99 cloud contains bigger and more heavily rimed ice crystals than 11 Nov 99, but fewer of them. Although it is only speculation, we believe the difference in particle size

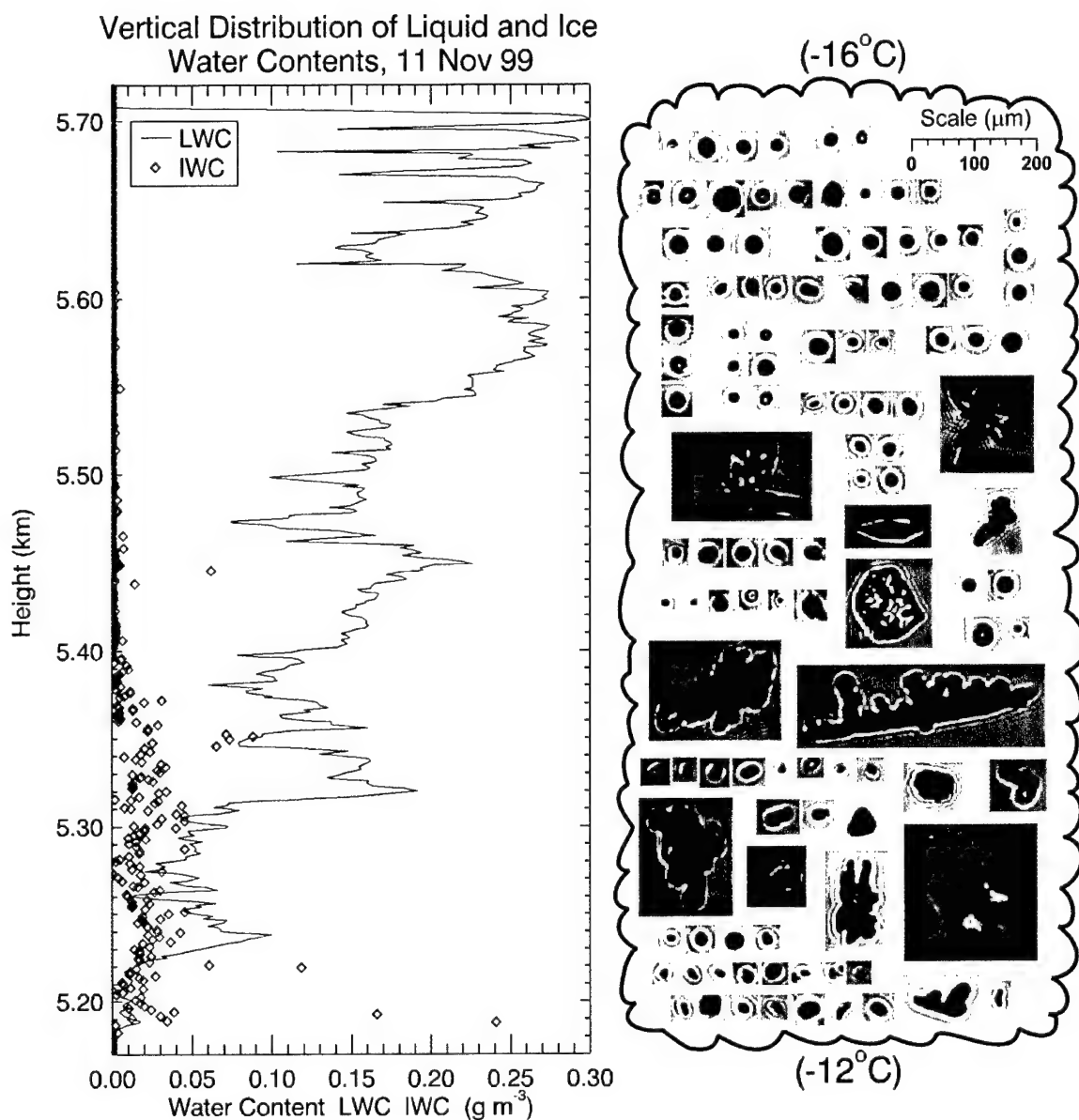


**Fig 5.7** Vertical profiles of liquid and ice water content ( $\text{g m}^{-3}$ ) for the 11 Nov 99 single-layer cloud case. To the right is a vertically consistent collage of CPI images, showing representative particles at the relative location they were measured in the cloud.

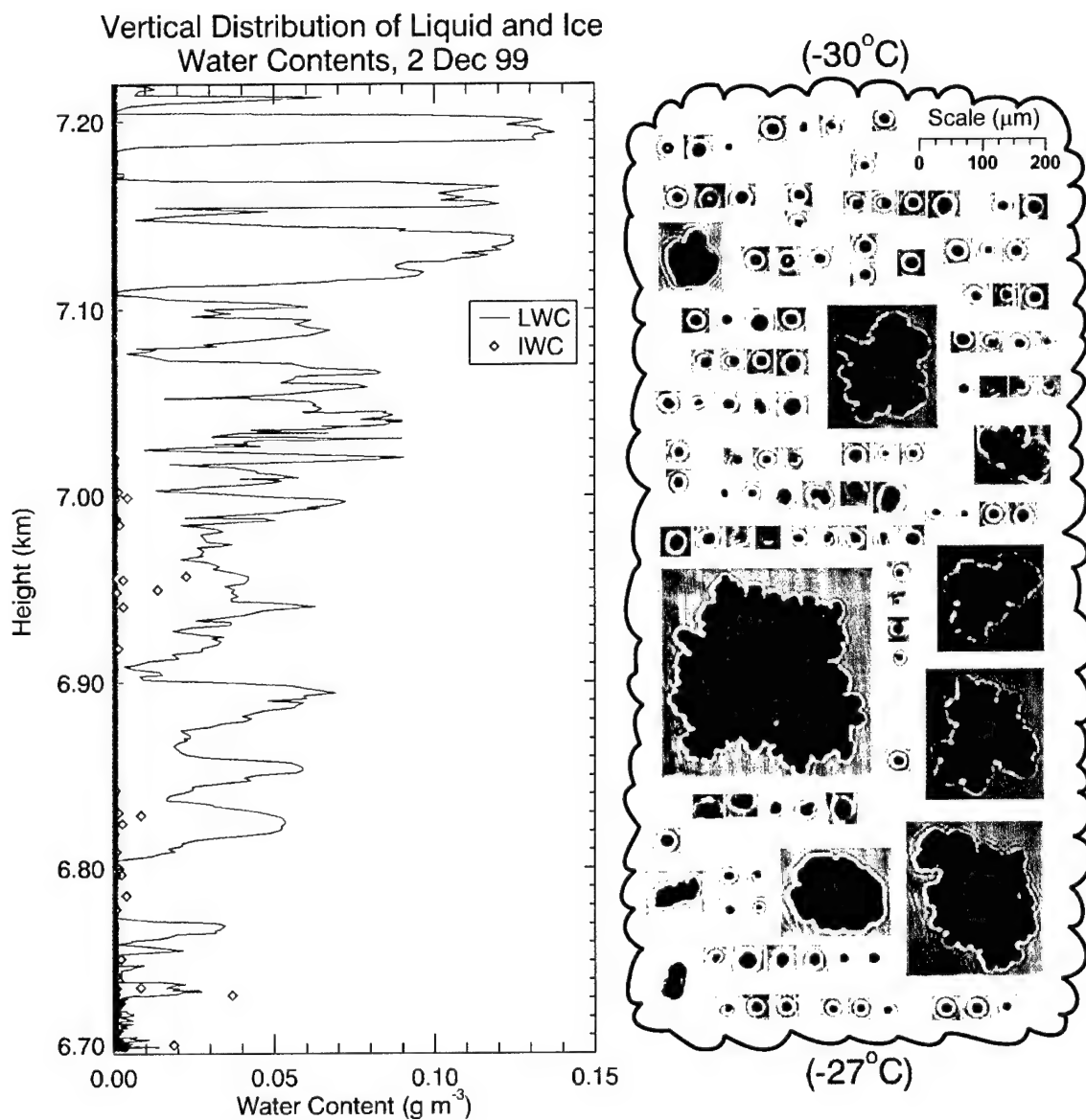


**Fig 5.8** Same as previous figure except for 2 Dec 99. Note the change in scale; this cloud has half the lwc as the 11 Nov 99 cloud. Also, despite temperatures in the  $-27$  to  $-30^{\circ}\text{C}$  range, this cloud had very low amounts of iwc. This is mainly due to a low concentration of ice particles, as the sizes were generally larger than for 11 Nov 99.

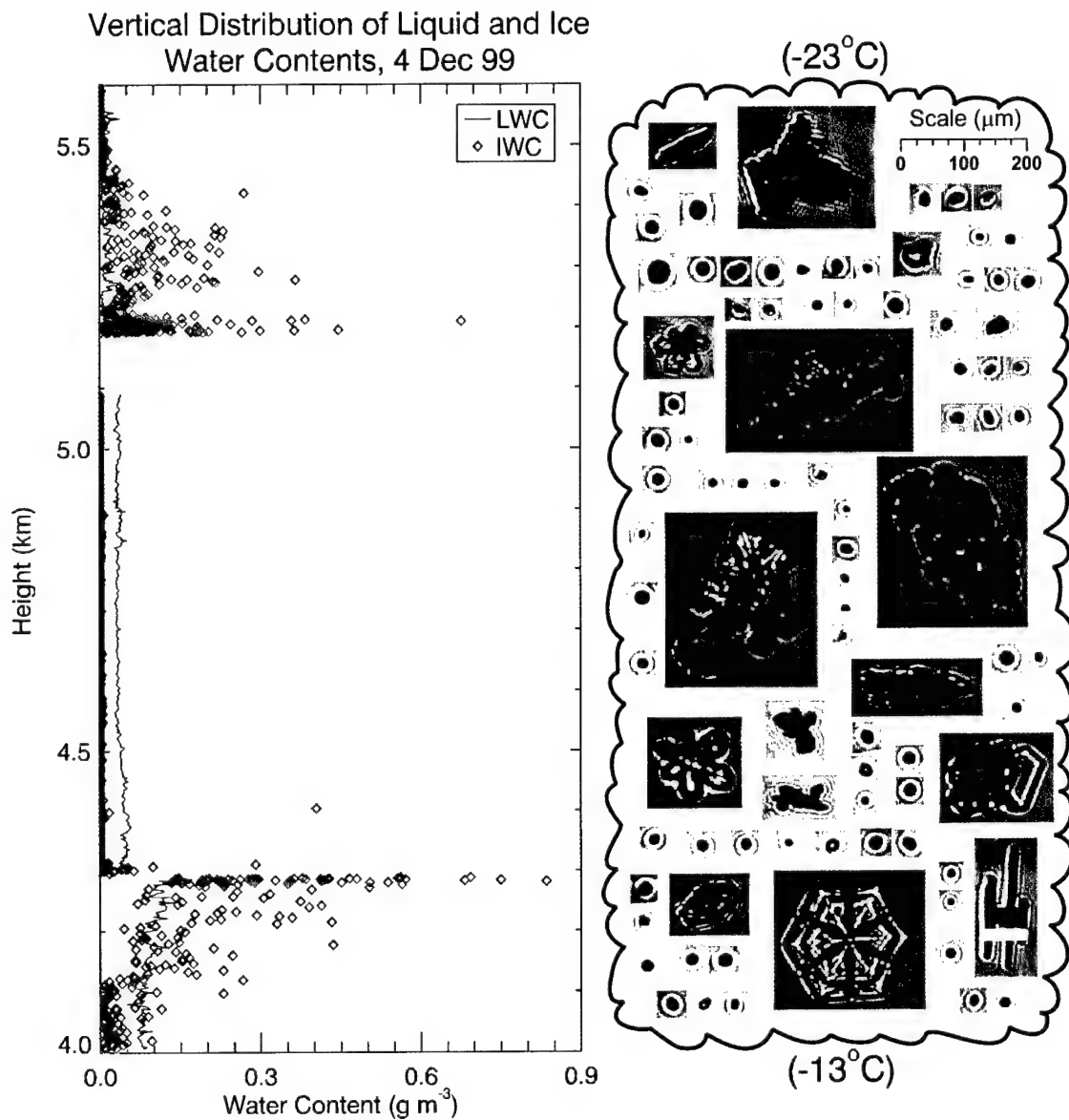


**Figure 5.9** Same as the previous two figures except for 4 Dec 99. This cloud was “psuedo-convective”, as it was detrained from convection upstream and then advected over the ARM site. The two discontinuities in lwc and iwc are a result of air traffic control delays of up to 15 minutes.

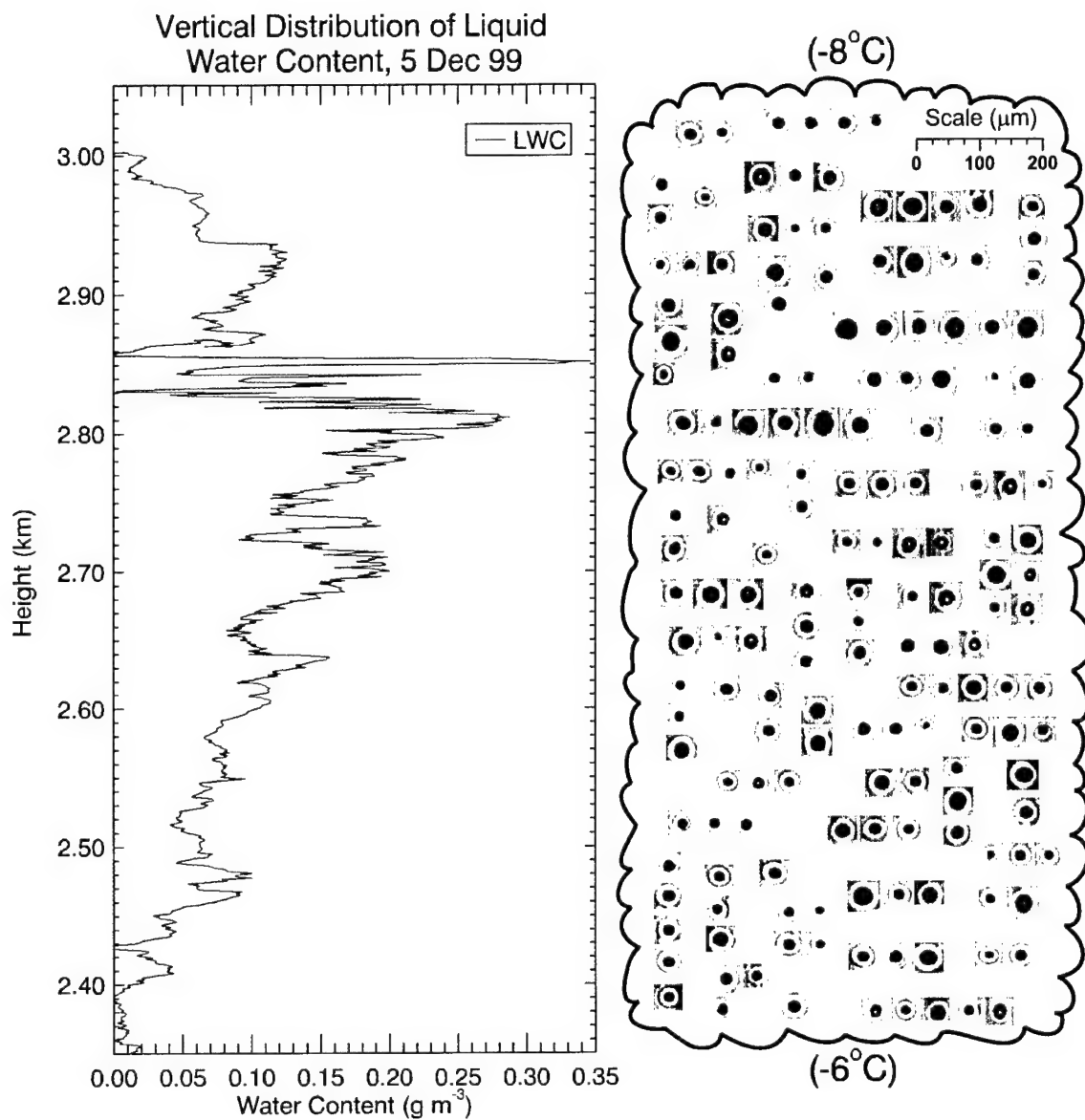


**Figure 5.10** Same as previous three figures except for 5 Dec 99. This cloud was composed primarily of supercooled liquid droplets, despite temperatures of only  $-6$  to  $-8^\circ\text{C}$ . Dry air entrainment near cloud top caused a slight departure from the increase of lwc with height seen in figures 5.7-5.8.

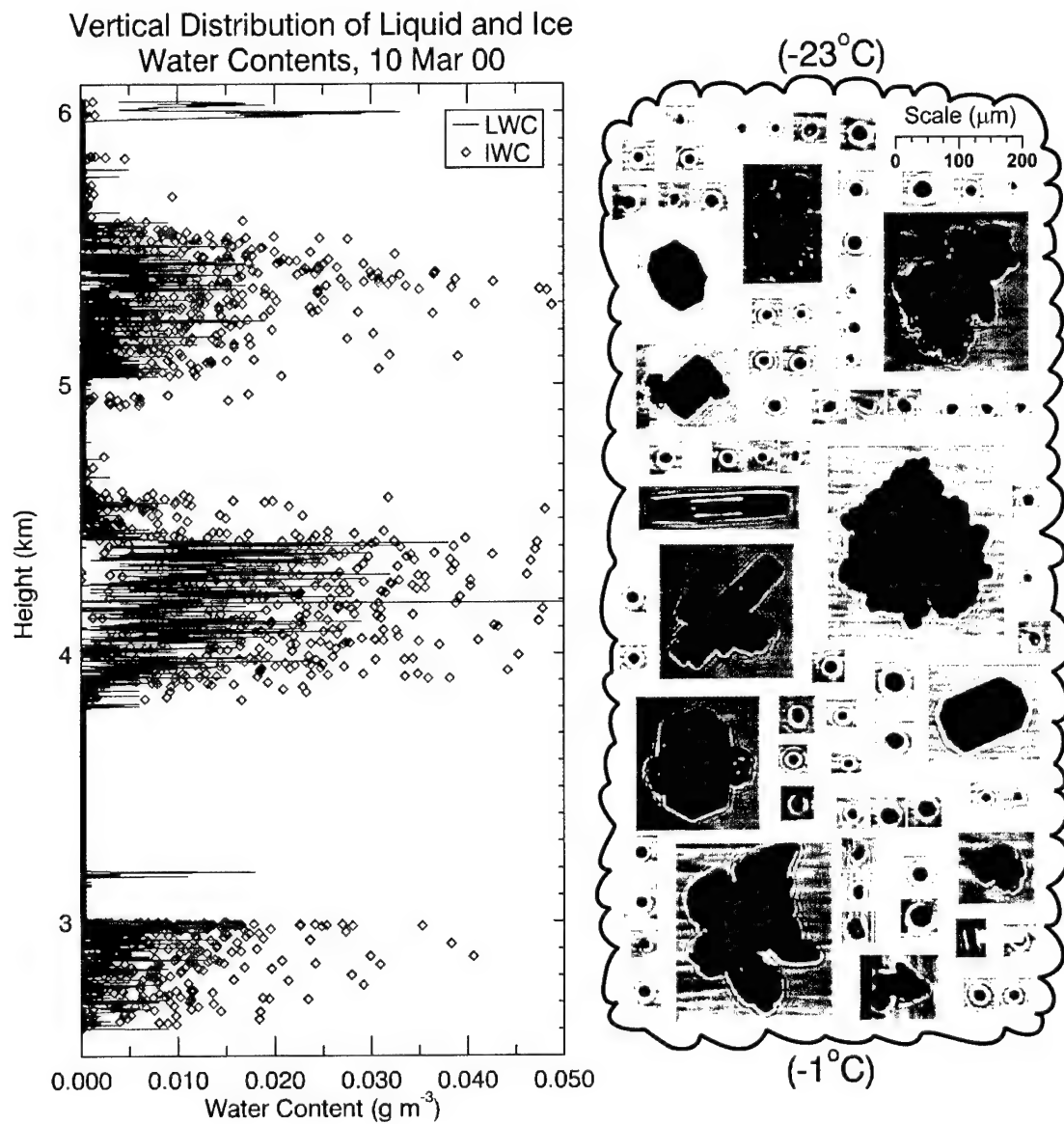


**Fig 5.11** Same as previous four figures except for multi-layered cloud on 10 Mar 00. Note the relatively low lwc values and the homogeneous vertical distribution of iwc.

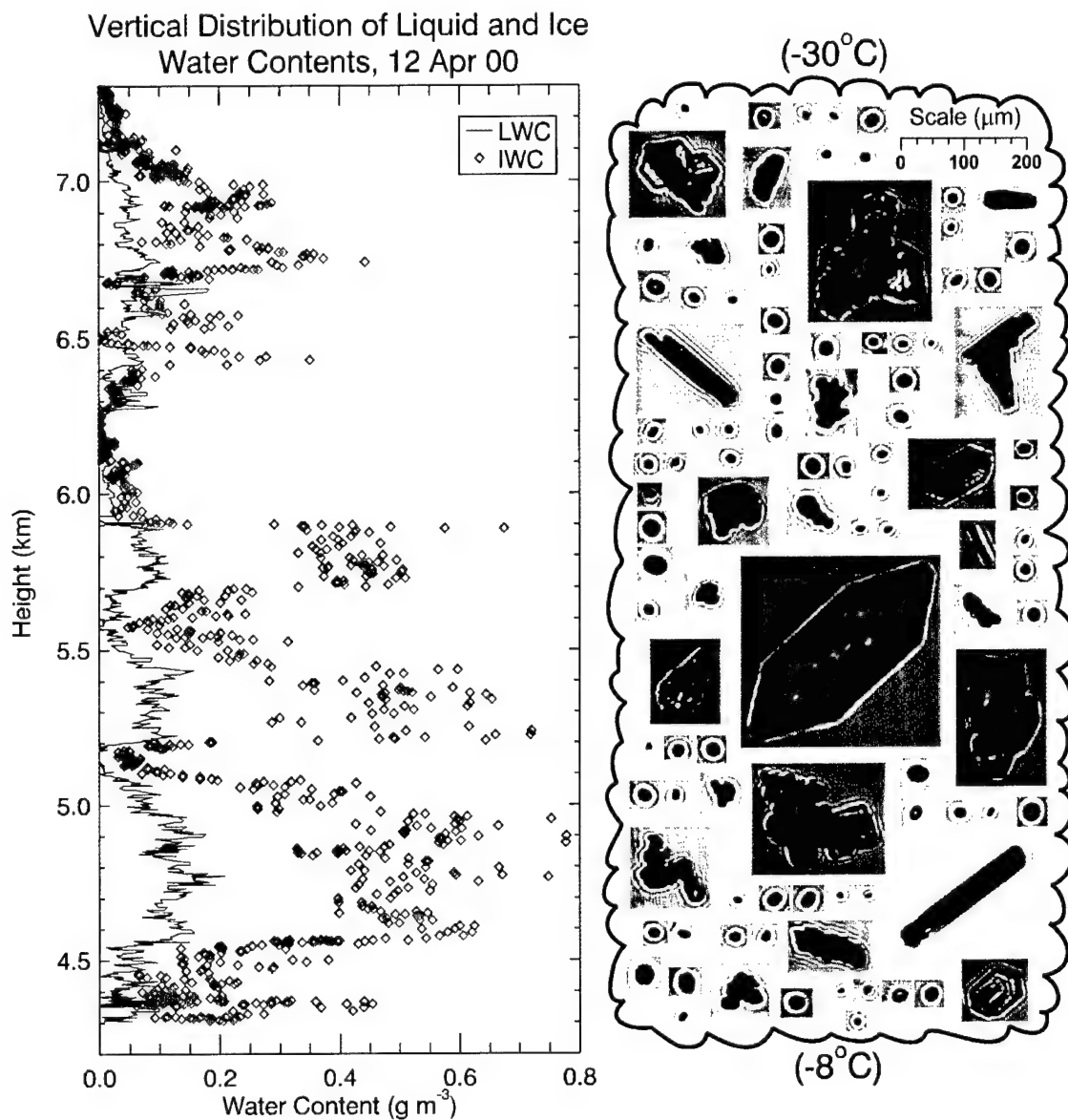


**Fig 5.12** Same as previous figure except for 12 Apr 00. Note the relatively high lwc, despite large amounts of ice. The higher total water content leads us to believe this cloud was more strongly forced than the 10 Mar 00 case. A seeder-feeder process is evident, with ice between the layers.

and concentration may be due to fewer ice nuclei in this cloud, allowing fewer ice crystals to grow at the expense of the available liquid water.

The 4 Dec 99 cloud is somewhat of a novelty in this study, as it was moderately deep, but not separated into distinct layers. The obvious vertical discontinuities in lwc and iwc in Figure 5.9 are due to air traffic control time delays of up to 15 minutes between each of the three distinct segments. The mean values listed in Table 5.1 are more meaningful quantitatively, but this profile highlights one of the major problems with Eulerian measurements over the ARM site; the cloud may change before the aircraft can get to it.

The cloud was pseudo-convective in nature; although it was quiescent for about a two-hour period during the aircraft measurements, there was considerable convective activity before and immediately afterwards. The observations followed a period of thunderstorms, with intense rainfall and gusty conditions at the surface, and preceded a squall line that was moving in from the southwest during our flight. These conditions may explain why the cloud is deeper, and the ice distributed more homogeneously, than the other cases. Also, note the mean lwc was an order of magnitude less than the other single-layer clouds, due mainly to the presence of large amounts of ice. The ice formed and grew at the expense of the available liquid droplets, resulting in iwc several times larger than lwc at the time of our observations. The very large and heavily rimed particles shown in the CPI images offer further support to the argument that this cloud was convectively mixed through a relatively deep layer.

The 5 Dec 99 cloud is also an interesting case, because it was 6 to 8° C below freezing, yet only one ice particle was sampled. It was composed primarily of small,

supercooled liquid droplets, with a maximum lwc of nearly  $0.35 \text{ g m}^{-3}$ . Unlike the clouds measured on 11 Nov and 2 Dec 99, cloud top entrainment appears to have had a disproportionately strong drying effect on the top two hundred meters of the 5 Dec 99 cloud. This seems to be related to a rather weak temperature inversion of  $0.5$  to  $1^\circ \text{ C}$  at  $2810 \text{ m}$ , which corresponds to the location of the lwc maximum. The inversion decoupled the top of the cloud from the main body and hindered dry air from being transported below the inversion, resulting in the observed lwc shape.

The 10 Mar and 12 Apr 00 cases illustrate an important feature of the multi-layered systems observed in this study; the ice is distributed more uniformly in the vertical profile, in contrast to the increase in iwc at cloud base observed in the single-layer cases. This implies that different mechanisms or processes are at work for the single-layer clouds and multi-layered systems. Despite the difference in the vertical distribution of ice, the individual layers of the 10 Mar 00 case retain essentially the same characteristic triangular shape of lwc increasing with height as the single-layer cases. However, the maximum lwc is only about  $0.04 \text{ g m}^{-3}$ , an order of magnitude less than that of the single-layer clouds. The 12 Apr 00 cloud, on the other hand, has a maximum lwc of  $0.14 \text{ g m}^{-3}$ , which is more in the range of the observed quantities of the single-layer cases. We speculate that the differences in total water may be due to greater forcing in the 12 Apr 00 cloud, causing a higher production of liquid water and a concomitant increase in ice particle growth.

### 5.3 Liquid Droplet and Ice Particle Spectra

Now that the liquid and ice structure has been presented in a bulk sense, it is interesting to look at how the size and concentration of the liquid droplets and ice particles vary through the depth of the cloud layer. First, the liquid droplet spectra are shown in Figures 5.13 through 5.16 using the FSSP measurements. Recall the FSSP measures particles up to 24  $\mu\text{m}$  radius. A visual inspection of the CPI images showed that only 1 in 72, or 1.3% of the liquid droplets had radii greater than 24  $\mu\text{m}$ . This observation gives us some confidence that we captured nearly all of the cloud liquid water droplets with the FSSP instrument. There may be some contamination of the FSSP measurements by small ice particles. However, due to high supersaturation with respect to ice, most ice particles grow rapidly to recognizable, non-spherical shapes of larger than 25  $\mu\text{m}$  in less than a minute in mixed-phase clouds (Lawson et al., 2001). Because of this dichotomy between ice particle and liquid droplet sizes, we use the FSSP measurements for the liquid water droplet spectra, and 2D-C measurements in the larger-sized bins for the ice particle spectra.

The liquid water spectra consist of droplet radius (microns) plotted against mean bin concentration ( $\text{cm}^{-3} \mu\text{m}^{-1}$ ). The clouds were divided into equal thirds; top, middle and bottom. The single-layer clouds all exhibit a common trait: droplet sizes increase with increasing height through the layer. For the 11 Nov and 2 Dec 99 cases, the mean concentration also increases with height. With respect to the entire system, this means the smallest concentrations of the smallest droplets reside in the bottom of the cloud, with increasingly larger concentrations of larger droplets in the upper portions of the cloud. This is consistent with the increase in lwc with height seen in the previous section.

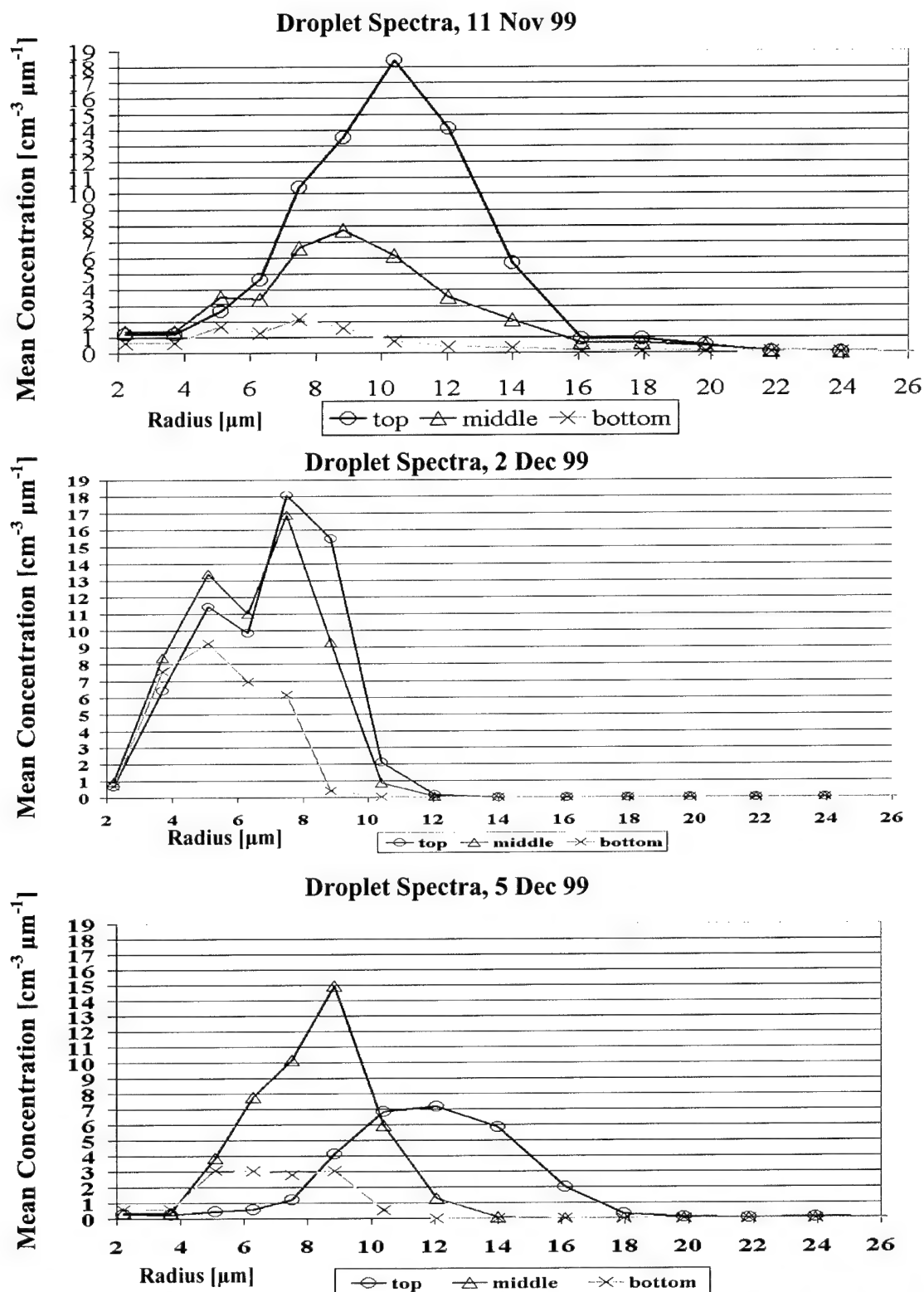


**Figure 5.13** Droplet spectra for the single-layer cloud cases on 11 Nov 99 (top), 2 Dec 99 (middle), and 5 Dec 99 (bottom). Notice a shift to larger-sized liquid water droplets with height through each cloud. The concentrations also increase with height in each cloud except 5 Dec 99, when entrainment caused cloud top drying.

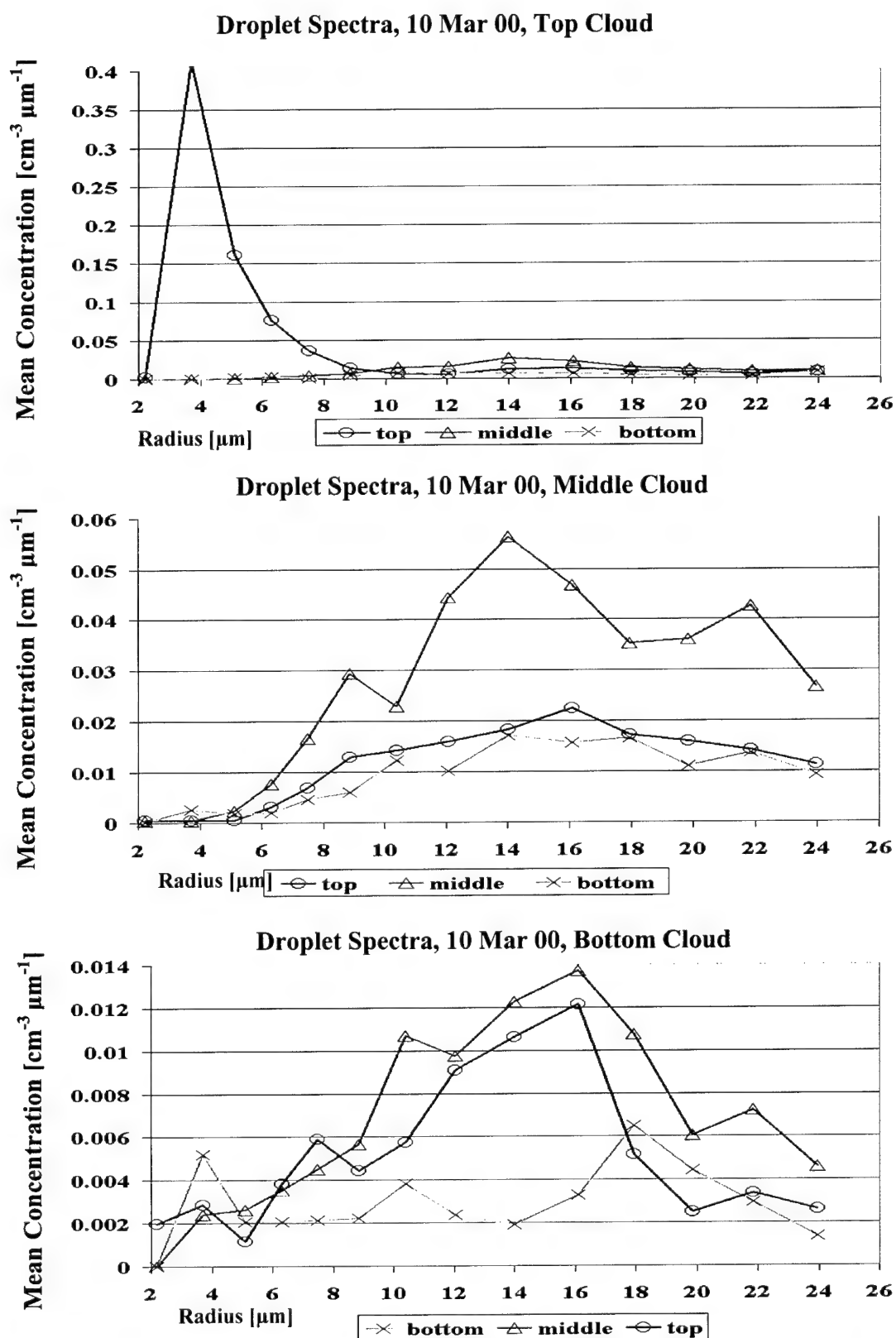


Figure 5.14 Same as figure 5.13, except for the multi-layered system observed on 10 Mar 00. Note the different vertical scales and the absence of droplet size and concentration with height, due to seeder-feeder processes and the presence of more ice particles in this system.

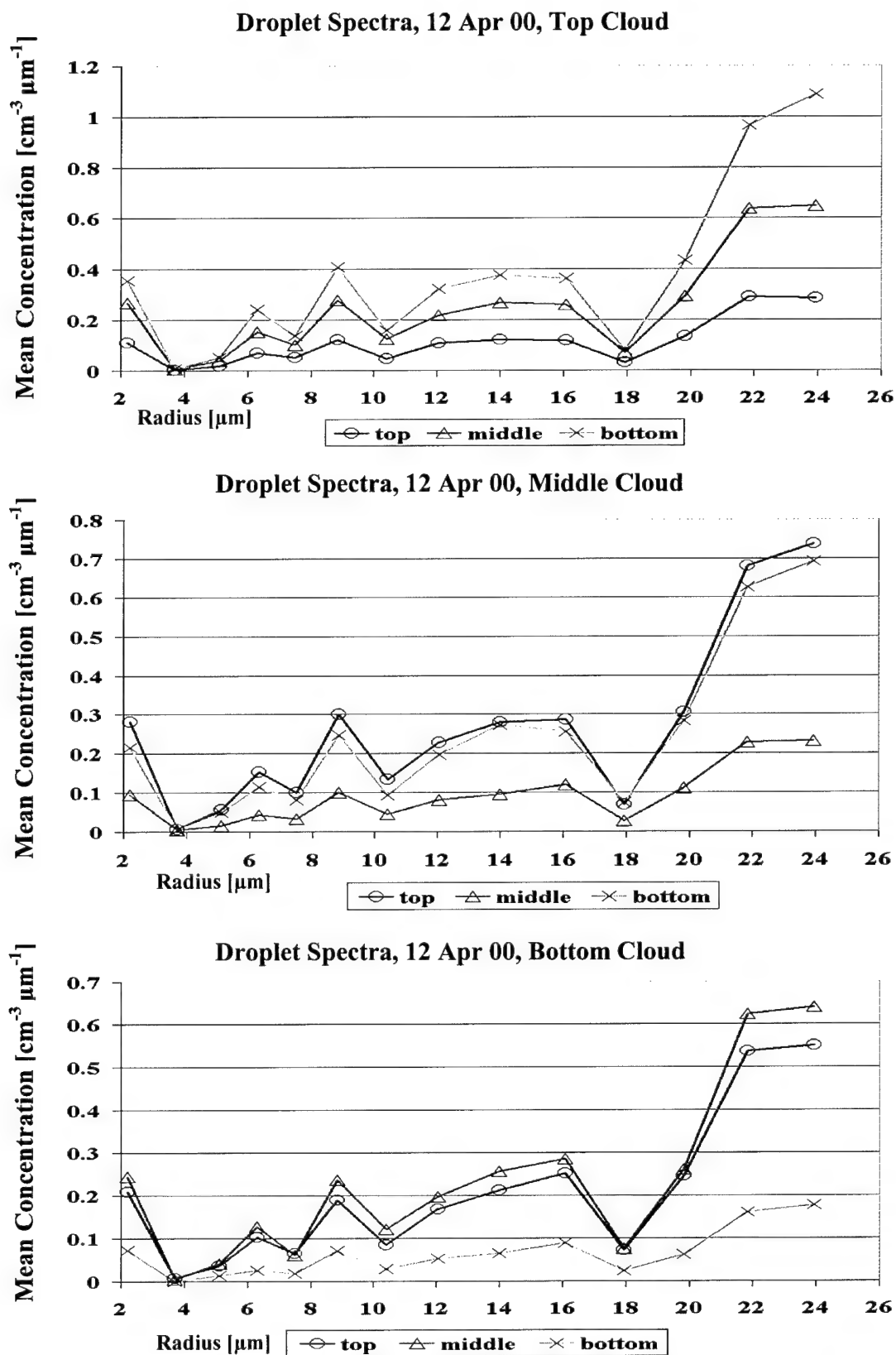


Figure 5.15. Same as figure 5.14, except for 12 Apr 00. The distribution of sizes with concentration is again fairly homogeneous. The increase at sizes greater than 20 μm may be due to some contamination by larger ice particles in those bins.

The 5 Dec 99 droplet spectra show the same increase in size with height as the 11 Nov and 2 Dec 99 cases, but the concentration of the largest droplets in the top of the cloud does not exhibit the same increase with height. Recall that the 5 Dec 99 case had a small temperature inversion that caused the uppermost part of the cloud to be decoupled from the rest of the cloud. The lwc values decreased with height above the inversion, due to evaporative dry air entrainment. This process reduces the amount of water vapor available for diffusive growth of the liquid water droplets, and causes the smallest droplets to evaporate first, resulting in the very small concentration seen in the size range below 6-7 microns in radius. The lack of small droplets then reduces the chances for growth by collision and coalescence, resulting in the broader distribution of droplet sizes at a relatively low concentration in the top of the cloud.

The liquid droplet spectra for the multi-layered systems are quite different from the single-layer cloud cases. Figures 5.14 and 5.15 show the droplet spectra for each of the three individual clouds composing the layered cloud systems on 10 Mar 00 and 12 Apr 00, respectively. Note that the mean concentrations are one to three orders of magnitude smaller than the former cases, reflecting the larger amounts of ice distributed evenly with height through the cloud layers. In both cases, the largest concentration of droplets is generally in the 14 to 16  $\mu\text{m}$  size range. The first exception is a relatively large concentration of 4-5  $\mu\text{m}$  droplets in the top part of the top cloud layer on 10 Mar 00. This may be due to small ice falling from a cirrus layer that was above the mid-level system, with the ice growing at the expense of the available lwc. However, the concentrations are all quite small, making it equally likely that the small peak is simply due to measurement noise. The second exception is the relatively large concentration of

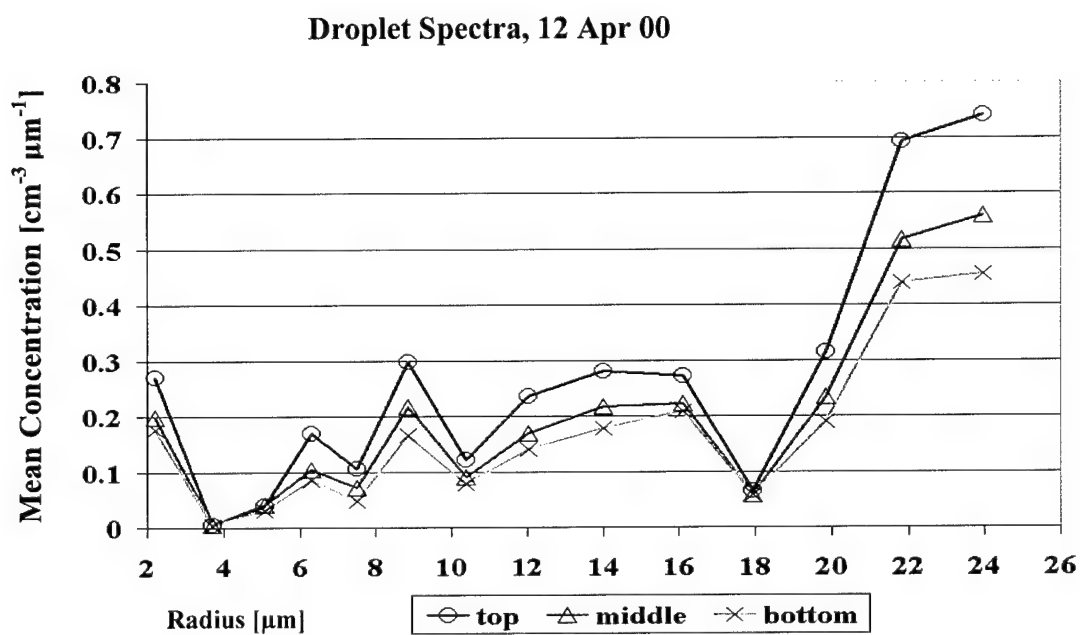
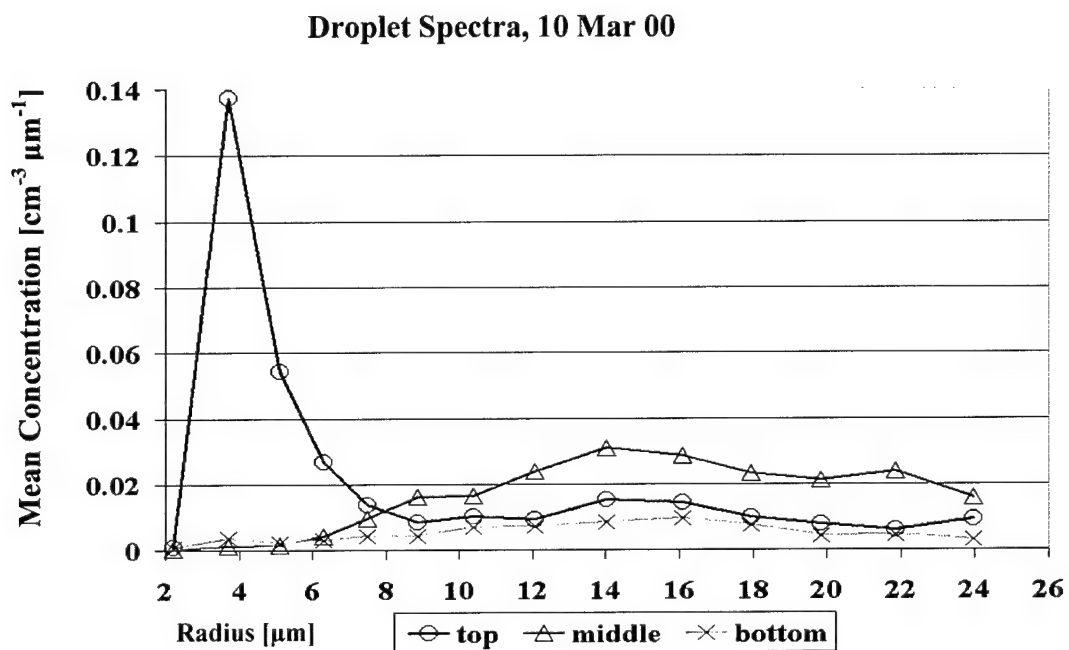


Figure 5.16 Same as the previous two figures, except in this case the droplet spectra is a summation of the earlier plots for the total three cloud system.

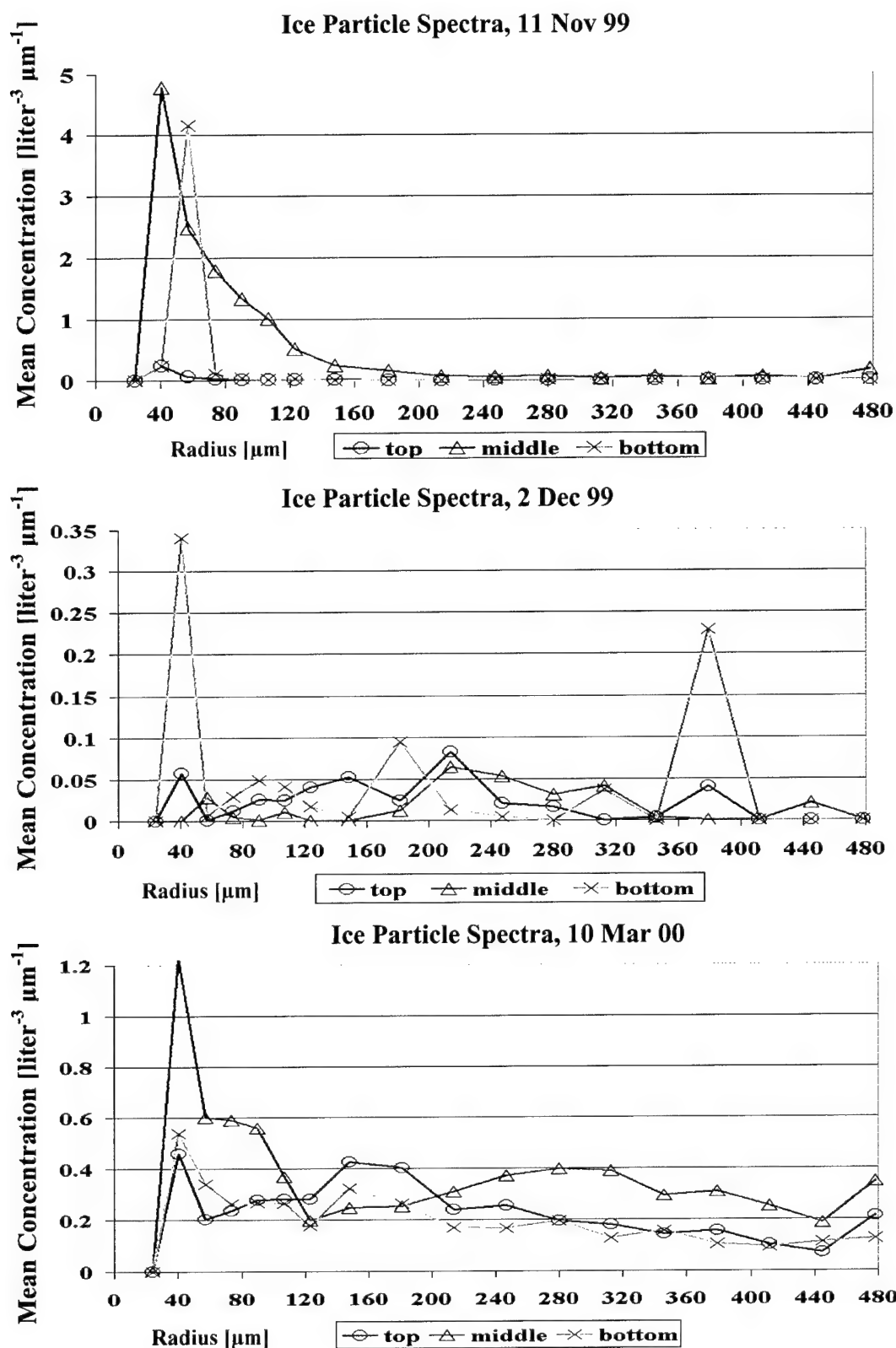


Figure 5.17 Same as the previous four figures, except for ice concentration and size using 2D-C measurements, rather than FSSP liquid droplet spectra. Note the relatively small and rather homogeneous concentrations for all ice particle sizes.

droplets greater than 20  $\mu\text{m}$  in all three cloud layers of the 12 Apr 00 system. This effect may be due to some contamination of the measurements by small ice particles in the largest FSSP size bins, as the CPI images indicate a rather large concentration of small ice particles through this cloud system. However, the overall FSSP spectra for the 12 Apr 00 flight looks somewhat suspect, as the mean concentrations all vary by a similar amount in a given size bin. Finally, Figure 5.16 shows the droplet spectra through the entire system, rather than each individual layer, for both 10 Mar and 12 Apr 00.

Figure 5.17 is a representative sampling of ice particle spectra for single- and multi-layered clouds observed on 11 Nov 99, 2 Dec 99, and 10 Mar 00. Overall, the mean ice concentrations are relatively low, with a uniform distribution of particles greater than 100  $\mu\text{m}$  in radius. In each case, the peak concentration is in the middle or bottom part of the cloud for ice particles in the size range from 40 to 80  $\mu\text{m}$  radius.

More information about the particle sizes and concentrations can be gleaned from Figure 5.18, which shows how these quantities are distributed vertically through the cloud systems. In this figure, we show the single-layer cloud from 11 Nov 99 and the two multi-layered systems from 10 Mar and 12 Apr 00. In the single-layer cloud, the ice particle concentration peaks in the bottom half of the cloud, with a mean of approximately 20  $\text{liter}^{-1}$ , and a maximum of 55  $\text{liter}^{-1}$ . The mean size appears to be about 60 to 80  $\mu\text{m}$  in radius, matching the values depicted in Figure 5.17, with a couple of particles near the base of the cloud approaching 200  $\mu\text{m}$ .

Unlike the single-layer cloud, the concentrations of both the multi-layered systems exhibit rather consistent particle concentrations through the vertical, although the 12 Apr 00 case does vary somewhat from about 50 to 150  $\text{liter}^{-1}$ . The main difference

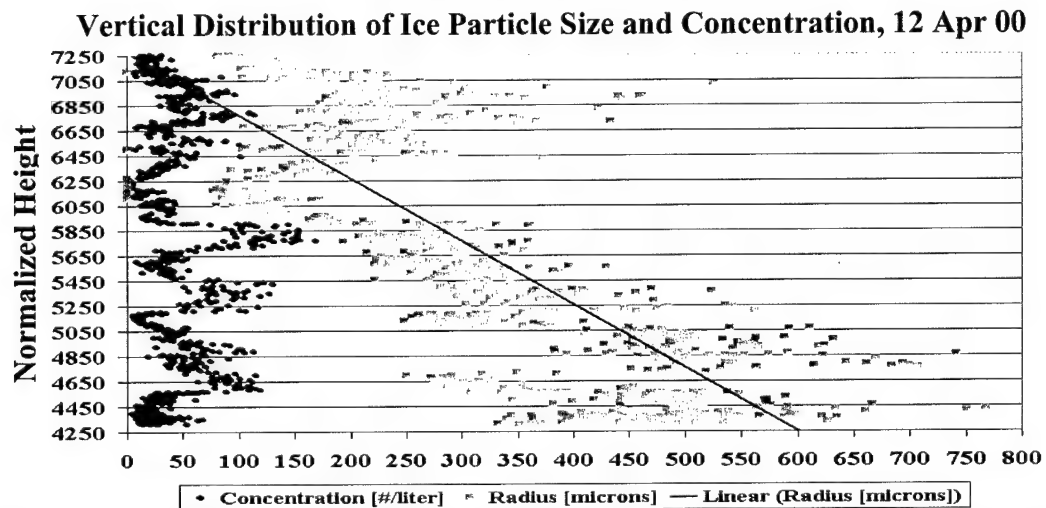
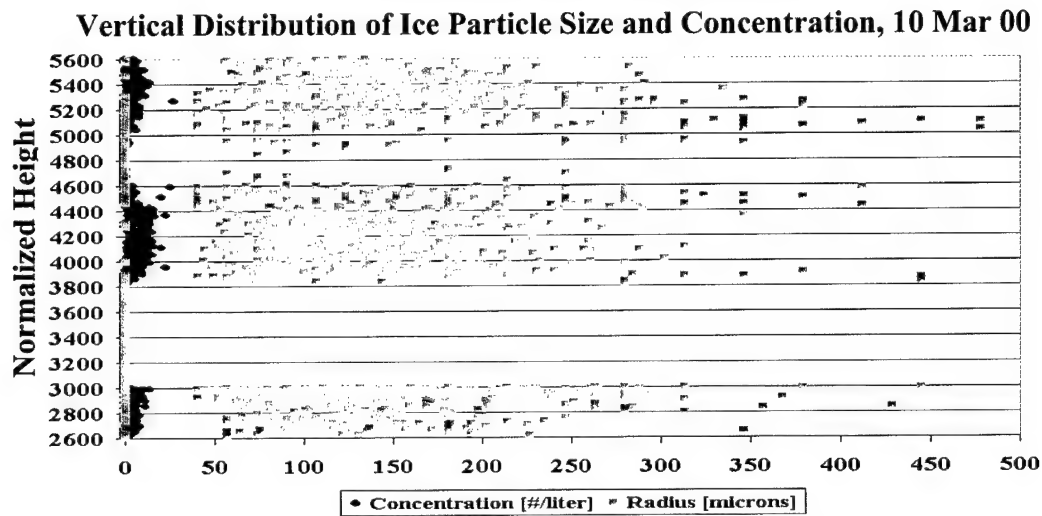
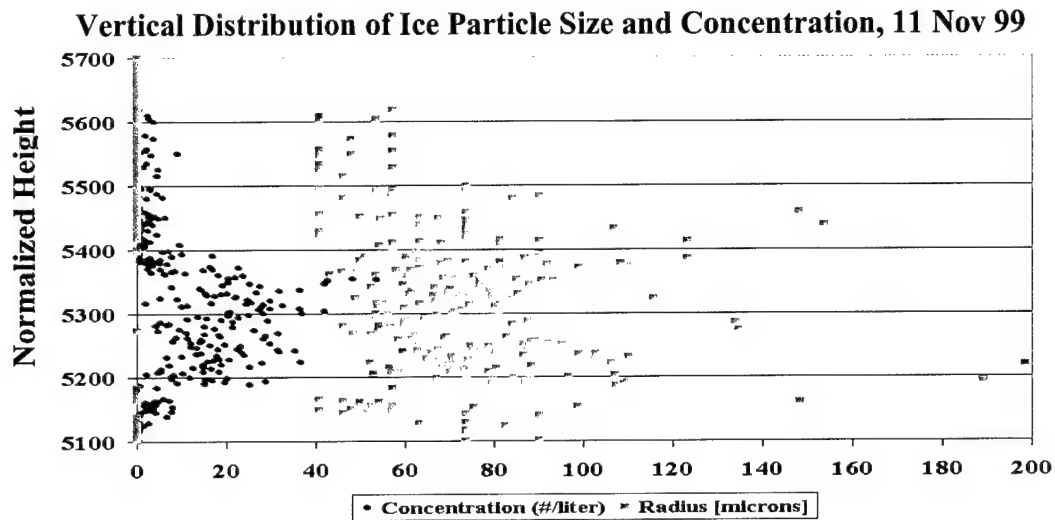


**Figure 5.18 Differences in vertical distribution of particle size and concentration between single layers (top) and multiple layers (middle and bottom). Note the increase in particle concentration at the bottom of the single layer cloud, the uniform distribution of both size and concentration in the 10 Mar 00 case, and the increase in size with decreasing altitude on 12 Apr 00.**

between the multi-layered systems is that the particle sizes remain relatively constant through all layers of the 10 Mar 00 system, but increase steadily in size with decreasing altitude in the 12 Apr 00 case. We speculate on the reasons for these observed similarities and differences in the next section.

#### **5.4 Differences between Single and Multi-layered Clouds: Seeder-feeder?**

For most single-layer, mixed-phase clouds, the aircraft measurements show that lwc is a maximum near cloud top, while iwc is a maximum near the base (e.g. Figures 5.7-5.8). However, a more uniform distribution of iwc is apparent through the vertical samples of both multi-layered cloud systems (e.g. Figures 5.11-5.12). This observed phenomenon is best explained in terms of a seeder-feeder process (e.g., Cotton and Anthes, 1989), which is noted in several previous modeling and observational studies. For example, Harrington et al. (1999) found significant sublimation of ice (moistening) occurred in the dry regions below cloud base, contributing to the formation of lower cloud layers in numerical simulations of theoretical mixed-phase Arctic stratus clouds. Jiang et al. (2000) simulated an actual mixed-phase Arctic stratus cloud and commented on the continuous production of ice that was subsequently removed to the sub-cloud layer. In an observational study, Hobbs and Rangno (1998) described a seeder-feeder mechanism at work, but noted it was mainly altocumulus and altostratus feeding lower level stratus clouds.

The main evidence for a seeder-feeder mechanism in this study is the presence of some ice particles between the layers, as seen in the CPI imagery and the 2D-C

concentrations for the multi-layered systems (Figures 5.11-5.12). Ice particles were observed between all layers on 12 Apr 00 and between the top two layers of the 10 Mar 00 case. However, there was no evidence of ice particles falling from the middle-cloud layer into the bottom layer on 10 Mar 00, despite a homogeneous iwc profile throughout the 400 m depth of the lowest cloud. In this case, it is quite possible that ice particles fell into the lowest layer at an earlier time and were maintained in a colloidally unstable balance in the cloud during the aircraft measurements. Relative humidity between the middle and bottom layer ranged from 65% to near 95%, which would have sustained larger particles traversing the fall distance. It is also possible that a fourth layer existed between the middle and low cloud shortly before we executed the spiral, seeding the cloud and then dissipating or advecting out of the ARM site area ahead of the other layers. There is evidence for this latter supposition, as a thin band (< 70 m thick) of liquid water was observed approximately 140 m above the lowest layer, hinting at a cloud layer there prior to aircraft arrival.

Hobbs and Rangno (1998) offer supporting evidence for one of these two seeder-feeder scenarios. They contend that clouds containing ice with a crystal habit different from the temperature regime in which they are found must have fallen from a higher level (relationships between temperature and ice crystal growth habits have been established by a variety of authors, e.g., Nakaya, 1954; Kobayashi, 1957; Hallett and Mason, 1958), and illustrate this point with a case in which altocumulus clouds with tops warmer than  $-10^{\circ}\text{C}$  contained stellar crystals. Since stellar crystals grow at colder temperatures, they must have formed in higher clouds and been transported to the altocumulus. The temperature of the bottom layer on 10 Mar 00 ranged from  $-0.9$  to  $-4.1^{\circ}\text{C}$ , yet many

particles were not the simple plates or hollow columns one would expect to find at these temperatures. Instead, we observed more stellar-shaped crystals, with many showing signs of considerable riming and aggregation. Since stellar crystals grow at temperatures colder than  $-10^{\circ}\text{C}$ , these crystals must have fallen from higher clouds. The middle-layer cloud was situated at  $-7.7$  to  $-14.7^{\circ}\text{C}$ , so it is probable that the particles formed and grew there before seeding the lowest layer.

The relatively large size of the particles at and near cloud top further supports this idea. Large particles would not be resident at cloud top if normal mixing processes were at work. It is important to realize that if ice particles were not continuously introduced into the top of a layer, sedimentation would cause an iwc maximum to form at cloud base, as observed for the single-layer cases. Finally, the uniform vertical profile of ice particles through each of the layers suggests that the ice crystals were of a similar size distribution upon entering the cloud, which would be the case for particles large enough to achieve a fall speed to reach the next layer and survive sublimation.

Despite the similarities in iwc between the two multi-layered cloud systems, we previously noted a difference in the 2D-C vertical particle size distribution (Figure 5.18). For the 10 Mar 00 case, the mean ice particle size mirrors that of the ice water content; it is fairly homogeneous through the depth of the cloud, with a mean size of approximately  $150\text{ }\mu\text{m}$ . However, the 12 Apr 00 case showed an almost linear increase in size from  $75$  to  $650\text{ }\mu\text{m}$  towards the base of the overall three-layer system. This observation is probably related to the total lwc of the clouds and the distances between the layers. On 10 Mar 00, the liquid water content is an order of magnitude lower than 12 Apr 00, and the distance between the middle and lowest layer is about 800 meters. These two factors

would lead to less growth in a given layer and more sublimation of particles between layers, helping to constrain the size distribution. The 12 Apr 00 layers, on the other hand, were closer together and had higher liquid water contents, allowing particle growth to proceed through the entire depth of the system.

The irregular shapes (Figures 5.7-5.12) found in all of these clouds also suggest the ice particles may have experienced alternating periods of growth and sublimation, as proposed by Korolev et al. (1999) for Arctic stratus clouds. For example, several of the larger particles in the lowest layer had thin necks connecting bigger pieces of the crystal together, and others had a smooth, rounded appearance. Both of these features indicate sublimation. Some of the particles also appeared to have faceted polycrystalline structures, consisting of combinations of different ice crystal habits growing in different directions. This presupposes the ice particles experienced several different temperatures, and thus different growth habit regimes, as they fell through and between cloud layers. The ability to view these irregular shapes, and the role this plays in the analysis of mixed-phase clouds, will be discussed more in the next section.

## **5.5 Role of CPI Imagery to Observe Mixed-Phase Microphysics**

Previous studies of mixed-phase clouds have been hampered by the relatively poor resolution of the FSSP, 1D-C and 2D-C instruments, which project the particle images onto an array to measure the basic two-dimensional sizes and shapes. With these probes alone, it is nearly impossible to ascertain whether a particle is definitely liquid or ice, or whether it has experienced riming versus aggregation growth. Pinto (1998) measured two mixed-phase Arctic stratus clouds and stated the “phase of particles

detected by the 2D-C probe that are less than 100  $\mu\text{m}$  in diameter cannot be distinguished due to inadequate resolution.” Likewise, Gardiner and Hallett (1985) describe FSSP particle size distributions in mixed-phase clouds as spurious, while McFarquhar and Heymsfield (1996) note the distributions are of poor quality when large non-spherical ice is present.

As previously noted, the King liquid water content measurements are also subject to errors in mixed-phase conditions, as ice particles cause a small reduction in the temperature of the hot-wire probe, resulting in an anomalously high lwc measurement. These inherent uncertainties and inability to discriminate liquid from ice made earlier measurements of mixed-phase clouds extremely difficult to process and analyze. These deficiencies of the PMS probes may be one of the leading reasons for the relative lack of observational mixed-phase cloud research in the past.

The Cloud Particle Imager added several new dimensions to our observational study of mixed-phase clouds. The enhanced resolution of this instrument allowed us to ascertain specific sizes and shapes of ice crystals at any point in space and time. From the images shown, it is evident that there are more small supercooled liquid droplets near cloud top, while ice particles dominate the lower part of the single-layer clouds. Sun and Shine (1994) point out that both the albedo and the rate of change of albedo with ice fraction are significantly dependent on the method by which the phases are mixed. They also note that neglecting ice in clouds below the cirrus level may lead to a serious bias in cloud albedo for a given path of condensed water.

Ice crystal habits and the effects of riming were also readily discernible from the CPI imagery, as reported in Lawson et al. (1998). This piece of information was

especially useful in determining if seeder-feeder processes were operating in the multi-layer clouds, as we could discern whether a particle originated in a given layer or was transported there from elsewhere. We also observed particles with multiple habits, such as plate-like growth off a predominantly needle structure, demonstrating the likelihood of cyclic growth through turbulent mixing processes in these clouds.

Many small particles would have been virtually impossible to partition into liquid or ice without the CPI, but the imagery allowed us to reliably determine whether the particles were round liquid droplets or slightly misshapen ice particles. It is also quite apparent that the majority of ice particles are not pristine crystals, but are misshapen due to sublimation, melting, riming, aggregation and other cloud processes, as forwarded by Korolev et al. (1999). Since particle shape is related to density, terminal fall velocity, growth rate and radiative properties of ice crystals, it is important to realize how much the observed shapes deviate from the idealized ones currently used in most models and remote sensing retrievals. Stephens (1990) recognized the scattering properties of clouds are highly dependent upon condensate water path and particle size. Furthermore, McFarquhar and Heymsfield (1998) addressed the uncertainty of satellite retrievals of ice clouds, due to the poorly known scattering properties of complex ice crystals. The precision of single-scatter albedo, asymmetry parameter, and effective radius could all benefit from the high-resolution imagery the CPI brings to the cloud research community. Recognizing the potential utility of their instrument for these purposes, Lawson and Jensen (1998) forwarded the idea of using CPI images to validate measurements of retrievals from remote observations of the radiative properties of mixed-phase clouds.

## 5.6 Thermodynamic Structure

Some interesting and rather surprising features were observed in several of the thermodynamic fields of mid-level, mixed-phase clouds. In the following subsections, the vertical structure of temperature, virtual potential temperature, and wind shear in mid-level clouds are examined and compared with those found in stratocumulus clouds. Temperature is then plotted versus iwc to determine if the two quantities are correlated.

### 5.6.1 Vertical Temperature Structure

One surprising feature involved the temperature structure of these systems. We assumed there would be substantial temperature inversions at the cloud boundaries, especially cloud top, as is frequently noted in studies of stratus and stratocumulus clouds. For example, Albrecht et al. (1988) showed temperature inversions as strong as 7-8° C in their analysis of marine stratocumulus off the coast of California taken during the First International Satellite Cloud Climatology Project Regional Experiment (FIRE). Likewise, Nicholls (1984) reported inversions of 5° C from a study of daytime stratocumulus over the North Sea, and Bretherton and Pincus (1995) observed 2-4° C inversions in temperature soundings from the Atlantic Stratocumulus Transition Experiment (ASTEX). However, the CLEX measurements of mid-level clouds showed an almost linear decrease of temperature with height through the cloud, including the cloud boundaries (Figure 5.19). Note that both figures 5.19 and 5.20 are plotted against normalized vertical height, with “0” defining the cloud base and “1” defining cloud top. In all six cases, there was less than a 1° C temperature inversion at cloud top.

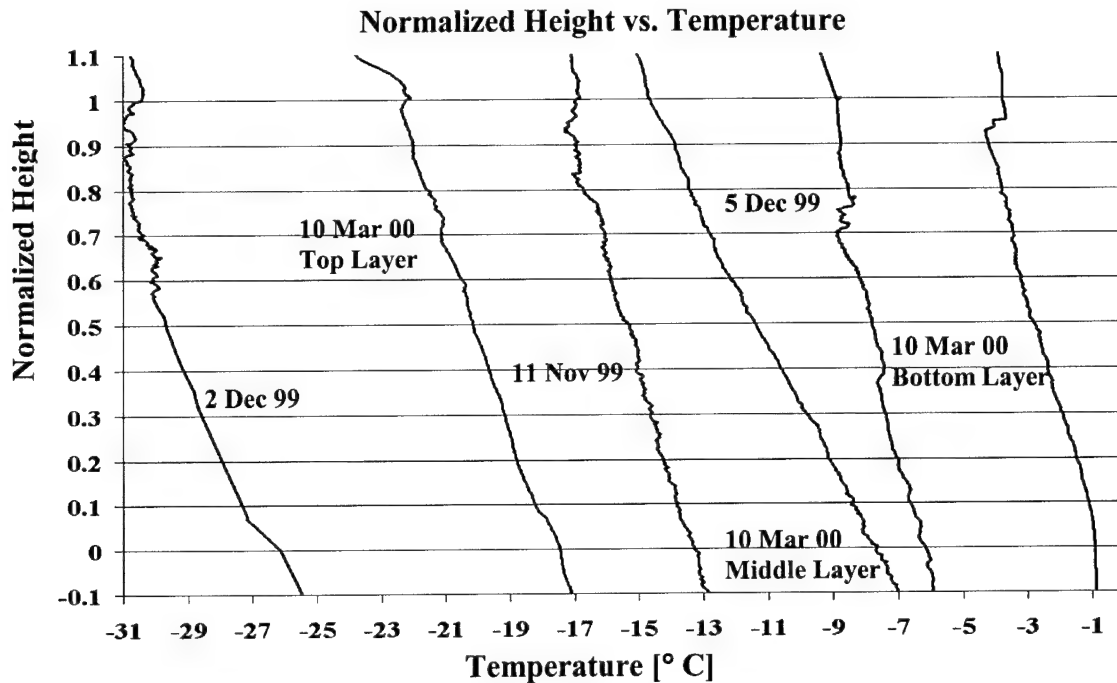


Figure 5.19 Vertical profiles of temperature for four of the cloud cases, including the individual layers of the 10 Mar 00 case. Note the lack of temperature inversions at the cloud boundaries, particularly at cloud top.

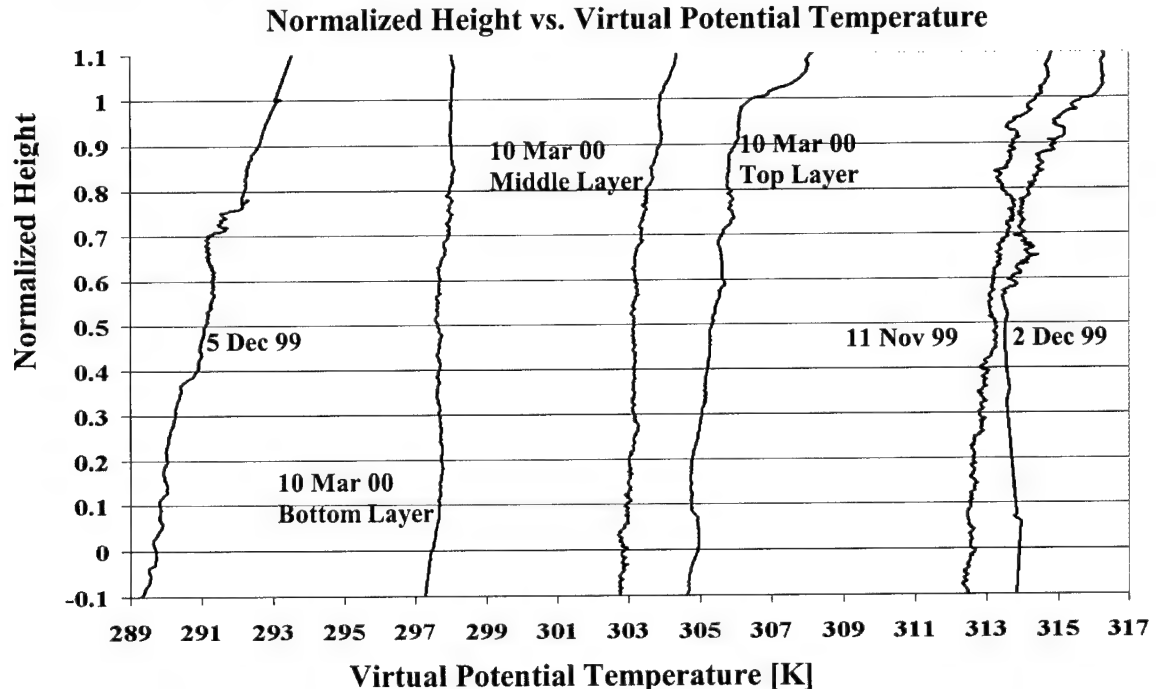


Fig 5.20 Vertical profiles of virtual potential temperature for the same cases as in Figure 5.19. This variable allows for slightly easier determination of mid-level cloud boundaries than temperature inversions, as there is a 1-2 K increase of  $\theta_v$  at cloud top (not seen at the top of the bottom and mid layers of 10 Mar 00 case).

### 5.6.2 Virtual Potential Temperature

One thermodynamic variable for which a contrast was apparent at the cloud interfaces was virtual potential temperature,  $\theta_v$  (Figure 5.20). Virtual potential temperature is the temperature that a parcel of dry air must have in order to have the same density as moist air at the same pressure, if subjected to an adiabatic compression or expansion to a final pressure of 1000 mb (Rogers and Yau, 1989). In most cases, the vertical profile of  $\theta_v$  increased monotonically with height until it reached cloud base, and then remained constant or increased by only 1° C through an entire cloud layer. Just below or right at the cloud top, it typically increased sharply by 1 to 2° C through a depth of about 100 m. For this reason, we suggest that the analysis of the vertical profile of  $\theta_v$  is a more accurate indicator for locating mid-level cloud interfaces than a temperature inversion, which tends to be much more pronounced for boundary layer stratus cloud tops.

### 5.6.3 Inversion Differences Between Mid-level and Stratocumulus Clouds

It is not entirely clear why the mid-latitude, mid-level cloud inversions are so much smaller than those found above stratocumulus, but the following argument is offered to explain the difference. The apparent strength of the stratocumulus temperature inversions may be related to the mechanics of the trade inversion (e.g., Johnson et al., 1999), which is controlled primarily by large-scale subsidence. Subsidence acts to warm the air above the boundary layer, creating a strong capping inversion. Within the boundary layer, radiative and moist convective processes work against the sinking air above the trade inversion, attempting to deepen the layer. Therefore, the large

temperature inversions evident above stratocumulus clouds are due to a combination of thermodynamic and radiative processes, caused by the influences of both the trade inversion and the cloud field. This effect may be enhanced by the longevity and strength of cloud top radiational cooling. Stratocumulus layers are warm and hence emit strongly to space; furthermore, they are quite persistent. These two factors result in the development of a strong temperature inversion. In contrast, mid-latitude, mid-level clouds are generally shorter lived (~ six hours) and maintained primarily by cloud-scale radiative and dynamical processes, preventing the development of strong inversions.

#### 5.6.4 Wind Shear

Inspection of the in-cloud horizontal winds with those found above or below cloud in Table 5.1 show that wind shears were also virtually non-existent at the cloud interfaces for most cases. There were no wind measurements for the 12 Apr 00 case, but the horizontal wind field was examined for both directional and speed shears at the cloud boundaries in the other five cases. One sharp directional wind shear of  $35^\circ$  was obvious at the top of the bottom layer on 10 Mar 00, but otherwise the vertical profiles of the horizontal wind field did not deviate by more than  $10^\circ$  in direction or  $5 \text{ m s}^{-1}$  in speed at the ambient air interfaces. (It is noteworthy that the large directional shear on 10 Mar 00 is coincident with the cloud region where the instruments did not capture any ice particles seeding the lower layer from above).

The lack of shear is also a difference from many stratocumulus clouds, which are coupled by drag forces to the surface and are fairly well mixed in the vertical by turbulence (Geisler and Kraus, 1969). Therefore, there tends to be little shear within the

boundary layer, but a wind speed or directional discontinuity across the inversion (e.g., Brost et al., 1982). Conversely, mid-level clouds are decoupled from surface processes and drift with the mean ambient wind. There are exceptions to this simplified conceptual picture. In their seminal article explaining why supercooled water may exist at the top of cold clouds, Rauber and Tokay (1991) mention that shear can result in part from the downward transfer of jet stream level momentum in the subsiding air above cloud top. However, due to the lack of mechanical wind shear in the clouds observed in this study, it seems unlikely that any wave motions or local circulations were induced by this mechanism. This finding suggests vertical differential heating as a primary candidate for generating the internal cloud motions necessary to maintain mid-level cloud turbulence.

#### 5.6.5 Ice Water Content versus Temperature

Hobbs and Rangno (1998) previously showed that ice particle concentrations in Arctic low- and mid-level clouds were poorly correlated with temperature. They noted that ice particle concentrations were correlated better with the size of the largest droplets and agreed with Pinto (1998) that ice particle concentration may be linked to the age of the cloud, with higher concentrations at later stages of the lifecycle. We found a similar relationship between 2D-C concentrations and temperature (not shown), and then utilized the method of Mitchell (1990) to examine the relationship between iwc and temperature.

Ice water content is a function of both particle concentration and size, and is plotted versus temperature for the combination of all mixed-phase cases (Figure 5.21). The two quantities are not well correlated, providing evidence that model schemes using a simple temperature threshold to determine the vertical structure of cloud ice and liquid

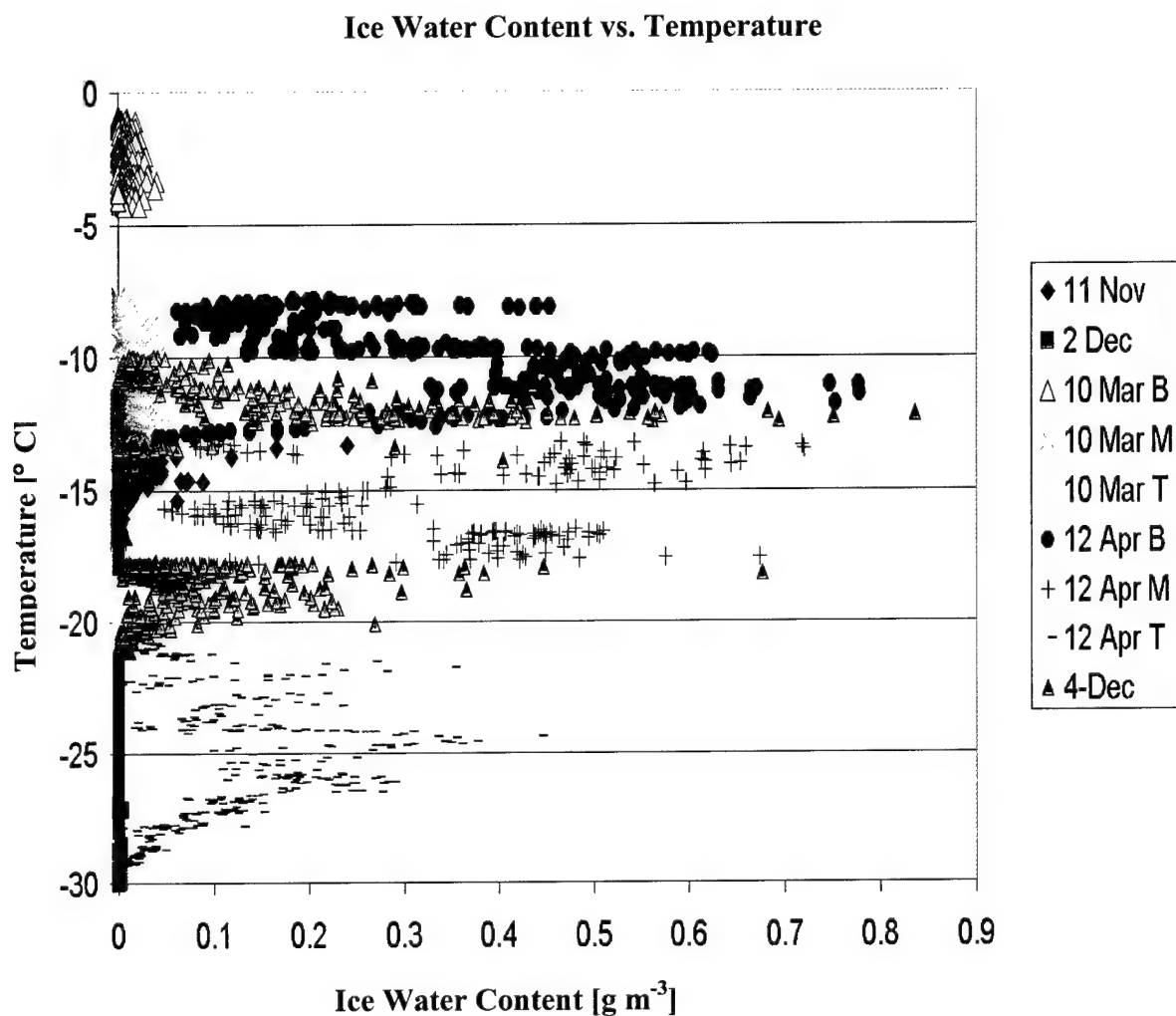


**Fig 5.21** Variation of ice water content with temperature for the five mixed-phase cloud cases. Highest values of iwc are between  $-8$  and  $-20^{\circ}\text{C}$ , corresponding to the maximum in both ice supersaturation and the growth rate of plate-like crystals centered at  $-15^{\circ}\text{C}$ . B, M and T denote bottom, middle and top of cloud, respectively.

are flawed. In fact, we found the least amount of ice at the coldest temperature of  $-30^{\circ}\text{C}$  in the 2 Dec 99 case. Neglecting the top layer of the 12 Apr 00 case for a moment, the iwc peaks in the temperature region between  $-8$  and  $-20^{\circ}\text{C}$ . This is the temperature regime in which the difference between saturation vapor pressure with respect to water and ice maximizes, and also corresponds to the maximum growth habit regime of plates, stellars and dendritic ice crystals centered at approximately  $-15^{\circ}\text{C}$  (Rogers and Yau, 1989). The peak in iwc at  $-25^{\circ}\text{C}$  in the top of the multi-layered 12 Apr 00 case may be due to the influence of the seeder-feeder mechanism described earlier (i.e., fed by ice from a dissipating cirrus cloud aloft). A sensitivity study of the effects of using the incorrect water phase for radiative transfer, and the impact that has on modeling applications, will be examined in more detail in Chapters 9 and 10. Other parameters which may influence the vertical distribution of ice in a mid-level, mixed-phase cloud are discussed in Section 10.5.2.

## 6. Comparison of Findings with Other Observational Studies

As noted in the introduction, several authors have previously completed observational studies of mixed-phase clouds. The general findings are compared to CLEX measurements in Table 6.1 and are summarized in this section. Overall, the cloud depths, temperatures, and liquid water contents of CLEX observations are within reasonable limits of other observational studies, giving us a degree of confidence in the aircraft measurements.

Heymsfield et al. (1991) took aircraft measurements of two clouds near Green Bay, WI in October of 1986. The first was a thin cloud, about 200 m thick, with a base at 7300 m, and the second was on the order of 500 m thick, with a base at 7500 m. Liquid water contents in the first case were only .01 to .02 g m<sup>-3</sup>, while the second case ranged from 0.04 to 0.12 g m<sup>-3</sup>. These values fall within the range of those in CLEX, but are on the low end of our measurements. The temperatures were -29 to -31° C, which is similar to our coldest day on 2 Dec 99. Vertical wind velocities in this study varied from .25 to .75 m s<sup>-1</sup>, which also compares quite favorably with CLEX measurements.

Hobbs and Rangno (1985) reported the findings on aircraft measurements and surface observations of 90 cumuliform and 72 stratiform clouds. One of their illustrative examples is an altocumulus cloud over Washington State with a base at 5 km, temperatures ranging from -8 to -13° C, and a depth of approximately 800 m. The

**Table 6.1. Cloud depth, liquid water content (lwc), and temperature (T) comparison between CLEX and other observational studies of mixed-phase clouds. CLEX values generally fall within the range of all other measurements.**

<i>Author</i>	<i>Cloud Depth</i> [m]	<i>lwc</i> [g m <sup>-3</sup> ]	<i>T</i> [°C]
Heymsfield, et al (91)	200-500	.01-.12	-29 to -31
Hobbs and Rangno (85)	100-1000	<.1 - 1.3	-4.5 to -26
Hobbs and Rangno (98)	30-800	.02 - .14	-1 to -31
Paltridge, et al (86)	300-700	.01 - 1.2	-6 to -11
Pinto (98)	130-290	.005 - .1	-13 to -20
Tulich and Vonder Haar (98)	200-800	.03 - .31	-10 to -23
CLEX	400-1500	.005 - .35	-0.9 to -31

measured maximum liquid water content was 1.30 g m<sup>-3</sup> near cloud top, which is roughly an order of magnitude higher than CLEX and the October 1986 clouds previously discussed. This cloud is probably significantly more convective than the others, with large updrafts producing greater amounts of liquid water.

Airborne measurements of mid-level clouds over the Beaufort Sea in Alaska were reported by Hobbs and Rangno (1998). In this study, they found altocumulus from 30 to 800 m thick, with temperatures in the 1 to -31° C range. Mean liquid water content varied from 0.02 to 0.14 g m<sup>-3</sup>, which is in good agreement with the CLEX

measurements. Droplet concentrations were  $105\text{--}450\text{ cm}^{-3}$ , with an average effective cloud droplet radius of  $10\text{ }\mu\text{m}$ . As previously noted, one of the conclusions of this particular study was that ice particle concentrations were poorly correlated with temperature. Although counterintuitive, this is the same relationship we observed in the CLEX data.

Paltridge et al. (1986) completed a case study of ice particle growth in a mixed-phase altostratus cloud. The system was divided into two layers, with the first from 2600 to 3300 m and the second from 3300 to 3600 m. The lwc varied from zero to  $1.20\text{ g m}^{-3}$ , depending on location within the cloud, which compares favorably with our cases. Temperatures in the cloud ranged from  $-6$  to  $-11^{\circ}\text{C}$ , which is similar to our 5 Dec 99 case. Upward vertical motion was calculated in this study to be approximately  $0.09\text{ m s}^{-1}$ , which is an order of magnitude lower than those we measured or those reported by Heymsfield et al. (1991).

Pinto (1998) analyzed two Arctic mixed-phase boundary layer clouds in the temperature range  $-13$  to  $-20^{\circ}\text{C}$ . He found that liquid water content generally increased with height through the cloud layer, with a maximum just below cloud top, and values on the order of  $0.01$  to just over  $0.10\text{ g m}^{-3}$ . This is in good agreement with our measurements and previously described studies. Total cloud ice generally decreased with height through the layer, with a maximum near cloud base. That trend is also apparent in the single-layer data presented earlier in this paper. Typical large-scale vertical velocities were  $+0.002\text{ m s}^{-1}$  in one cloud and about  $-0.005\text{ m s}^{-1}$  in the other. Due to these low values, Pinto concluded that the sign of vertical velocity is relatively unimportant for boundary layer cloud existence.

Tulich and Vonder Haar (1998) examined the measured structures of a multi-layer cloud in great detail. The cloud system started out as an altostratus layer from 5800 to 6000 m, with an altocumulus layer rising into it from a base of approximately 5125 m. Mean liquid water contents varied from a minimum of  $0.03 \text{ g m}^{-3}$  to a maximum of  $0.31 \text{ g m}^{-3}$  through the center of the cloud system. The mean value for most flight legs was 0.08 to  $0.16 \text{ g m}^{-3}$ . The reason for the relatively high lwc values may be due to the fact that this was a summertime system, and appeared to form from detrained convective moisture. Mean in-cloud vertical motion ranged from  $+0.6$  to  $-0.5 \text{ m s}^{-1}$ , with maximum values of  $+2.2$  and  $-1.8 \text{ m s}^{-1}$ . All values compare well to the CLEX measurements.

## **7. Cloud Processes**

This section will focus on a literature review of the processes that cause mid-level, mixed-phase clouds to form, maintain themselves, and eventually dissipate. The main processes discussed below are presented schematically in Figures 7.1-7.3, respectively.

### **7.1 Formation Processes**

In order for a cloud to form at any level, two ingredients must be present: moisture and lift. Large-scale ascent and radiative processes govern the formation of stratiform clouds in Tiedtke's (1993) ECMWF prognostic equation, and both are generally accepted as the primary mechanisms for generating mid-level clouds. After performing numerical simulations of altocumulus using a cloud resolving model and a mixed-layer model, Liu and Krueger (1998) echo this sentiment, "Moisture for altocumulus formation is transported upward by large-scale ascent or by cumulus convection, instead of by turbulent fluxes as in the stratocumulus-topped boundary layer."

Iselin and Gutowski (1997) state that the characteristic of clouds to form into vertically stratified layers suggests that the water vapor field in which clouds are embedded may also form layers in the vertical. They further propose that cloud layers might appear as part of a "tendency for atmospheric large-scale dynamics to draw fields

## Formation:

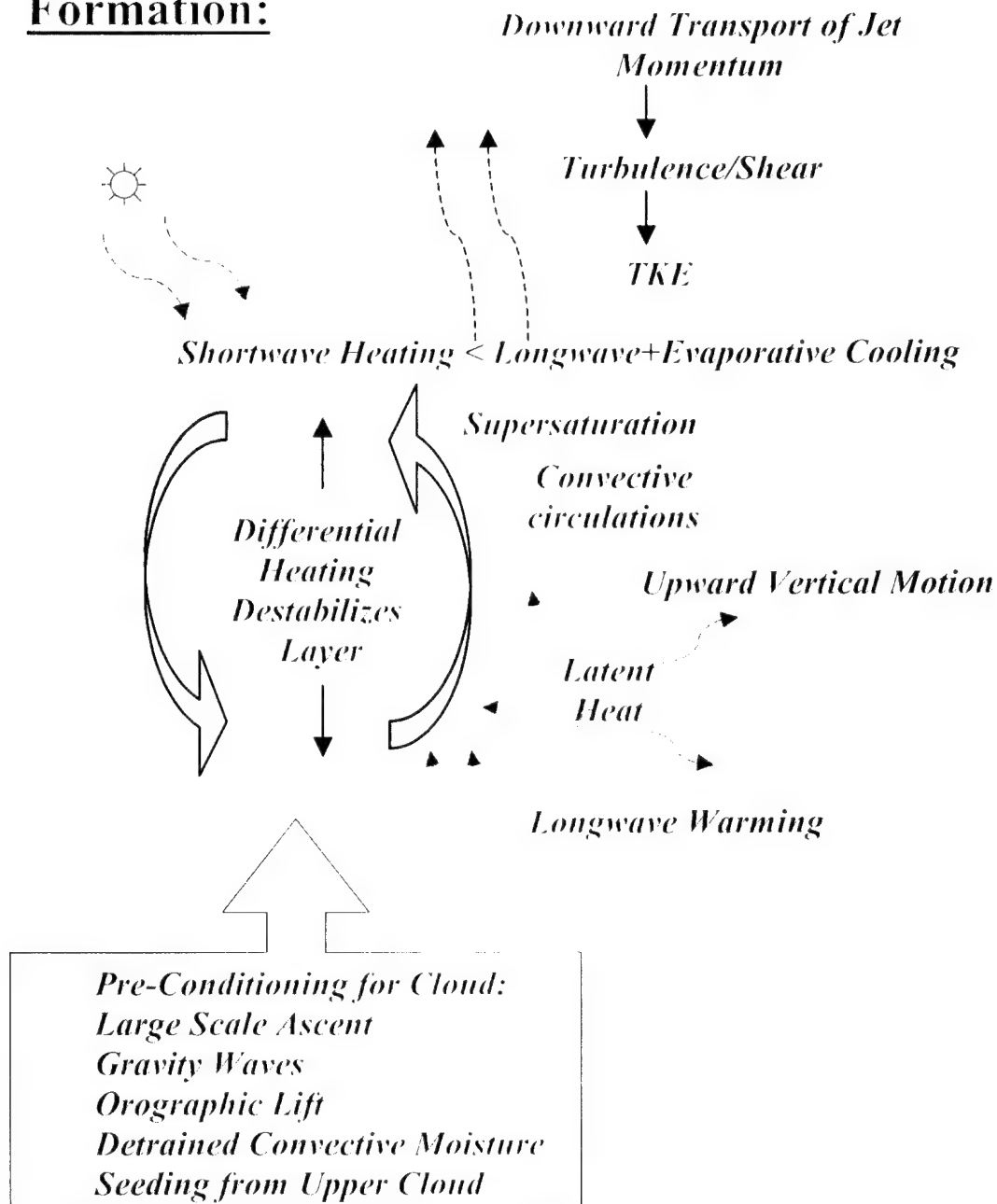


**Fig 7.1 Formative mechanisms and processes for mid-level, mixed-phase clouds. In this stage, a cloud is generally first formed by lifting a moist air layer until it cools and condenses, and then destabilized by vertical differential radiative heating and cooling processes. Evaporative cooling at cloud top and the release of latent heat further destabilizes the layer, causing internal circulations to develop. The added lift may increase the condensation supply rate, causing further cooling and more intense cloud circulations, but also increasing the dry air entrainment rate.**

into narrow structures.” The main large-scale lifting mechanisms are frontal boundaries and associated upper-level jet stream support, orographic forcing, and possibly gravity waves. Detrained moisture from upstream convective events or seeding from upper layer clouds may provide another moisture source for mid-level clouds. The exception to the need for lift is nighttime radiative cooling of a moist layer, which can result in cloud formation without additional lift.

Once the moisture is available and has been lifted and cooled to condensation, a mid-level cloud develops, and other processes begin to control the next stages of formative growth, as shown in Figure 7.1. The radiative heating rate structure of each cloud layer plays an important role in mid-level cloud dynamics (Cotton and Anthes, 1989; Rauber and Tokay, 1991; Tulich and Vonder Haar, 1996). Since shortwave heating rates are generally smaller than longwave cooling rates at cloud top, net cooling occurs there. When coupled with cloud base warming due to the absorption of longwave radiation, the cloud layer is destabilized, causing strong vertical differential heating and internal convective circulations. Cloud top entrainment then causes evaporative cooling, which combines with latent heat release at cloud base to further destabilize the cloud layer. Stephens (1978) adds that the cooling by longwave radiation in mid-level clouds is dominated by the window contribution and modified by changes of cloud height. The greater the height differences between cloud base and the Earth’s surface, the greater the heating at cloud base and the cooling at cloud top.

Although it was not observed in the CLEX clouds, wind shear may also play a role in driving the circulations of some mid-level clouds. Shear results in part from a downward transfer of jet stream-level momentum in the subsiding air above cloud top,

which may induce wave motions and local circulations (Rauber and Tokay, 1991). In an observational study of Arctic mixed-phase clouds, Pinto (1998) found that maximum turbulent kinetic energy occurred both at cloud top, due to radiative cooling, and in the vicinity of the low-level jet, where turbulence was shear induced. It is plausible that upper-level jet shear could induce mid-level cloud circulations in the mid-latitudes, particularly those that form at a higher level in the troposphere; however, radiative destabilization seems to be the primary mechanism.

Recall that the structure of single-layer clouds observed during CLEX had a supercooled liquid layer at the top, with a maximum in the iwc closer to the base of the clouds (e.g., Figures 5.7 and 5.8). Supercooled water develops in a parcel of air containing ice crystals when the relative humidity with respect to water exceeds saturation and the condensate supply rate is greater than the bulk ice crystal mass diffusional growth rate (Rauber and Tokay, 1991). The condensate supply rate increases with given pressure-altitude and temperature, and it decreases at higher altitudes and colder temperatures. The excess condensate supply rate is the key requirement for the formation of a supercooled liquid layer in the uppermost part of many mixed-phase clouds. Strong vertical gradients in water vapor and liquid water content often occur at cloud top, enhancing the radiatively driven instabilities and cloud circulations previously described. This is evidenced in part by the well-mixed layers seen in the  $\theta_v$  profiles.

A discussion of mixed-phase cloud formation would not be complete without mentioning the role of ice. Unfortunately, very little is known, and even less has been documented concerning the formation of ice in mixed-phase clouds. Hobbs and Rangno (1985) postulated that ice particles originate near cloud top in approximate concentrations

of one per liter after droplets reach a size equal to or greater than 20  $\mu\text{m}$  in diameter. Contact nucleation then occurs as thermophoretic forces drive small particles toward evaporating droplets, followed by diffusional growth.

A mean effective radius of 10.2  $\mu\text{m}$  was computed for the 5 Dec 99 case in which the aircraft measured only one ice particle, which is the threshold value for ice formation according to Hobbs and Rangno. The mean effective radii for the other mixed-phase cases were in the 12 to 20  $\mu\text{m}$  range, except for the 2 Dec 99 case. In that cloud, which had relatively low concentrations of big ice particles, the mean effective radius was only 7.8  $\mu\text{m}$ . This cloud may have been mature enough so that the liquid droplets were greater than 10  $\mu\text{m}$  in radius at an earlier time, allowing the ice particles to grow to large sizes at the expense of the liquid water, which depleted their sizes by the measurement time.

Hobbs and Rangno also address the high probability for ice enhancement mechanisms, especially ice splinter production (Hallet-Mossop Process), fragmentation of ice crystals, and further contact nucleation, to produce greater quantities of ice in mixed-phase clouds. These mechanisms can also cause rapid glaciation of clouds, which will be discussed further in Section 7.3.

Finally, Harrington et al. (1999) suggest that ice concentrations are extremely important for the formation of multiple liquid cloud layers, which formed through ice microphysical-radiative-dynamic interactions in their cloud-resolving simulations of Arctic stratus. The sedimentation of ice particles contributes to the formation of lower cloud layers when significant sublimation of ice (moistening) occurs in the dry regions below cloud base. Ice crystal sedimentation from upper layers tends to be dominated by

large ice crystals, so they quickly pass through the newly formed lower liquid layers, with very little impact to the liquid water content.

## **7.2 Maintenance Processes**

Tiedtke (1993) uses the time rate of change of cloud water and ice content to determine the longevity of clouds in the previously mentioned ECMWF forecast model. He proposed that the ice water content in non-convective situations depends on the condensation of water vapor produced in saturated large-scale ascent and the sedimentation of ice particles; Tiedtke states that the "...time evolution of the cloud variables, cloud water content, and cloud cover are determined by the sources and sinks due to the various cloud processes." These various cloud processes include, but are not limited to, radiative cooling, shortwave and latent heating, entrainment of ambient air into the cloud, vertical motion, and sedimentation of ice particles, as shown in Figure 7.2. Large-scale ascent or subsidence can also play a key role in determining cloud lifetimes.

To maintain turbulence in a mid-level, mixed-phase cloud, there must be a balance between the amount of longwave cooling and shortwave heating at cloud top, and the amount of longwave warming at cloud base. Longwave cooling increases with increasing cloud water; this cooling partially offsets the cloud top warming due to the release of latent heat and shortwave heating. Longwave warming at cloud base also increases with cloud water content, causing additional heating that enhances cells. In this way, longwave radiation acts as a positive feedback mechanism to increase buoyancy in convective cells. More vigorous convection results in updraft penetration into stable overlying air, where the detrained cloud water evaporates (Cotton and Anthes, 1989). In

## Maintenance:

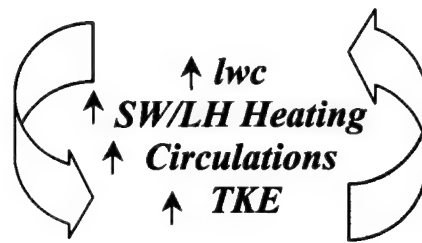
*Strong vertical gradients of  $wv$ ,  $lwc$ ,  $u$ ,  $v$ ,  $w$   
Supercooled liquid layer at least 30 m thick*

*$lwc$  maximum  
ice content minimum*

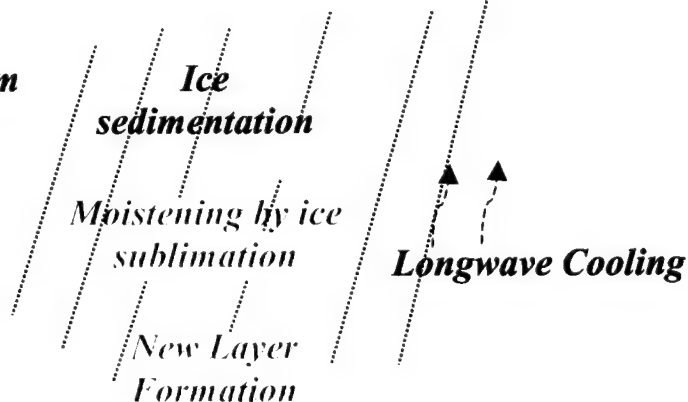
- Contact nucleation
- Diffusional growth

*Bulk ice crystal  
growth rate =  
Condensate supply rate*

*$lwc$  minimum  
ice content maximum*



*Ice content = sedimentation rate*



*Large ice falls through quickly – little impact*

**Fig 7.2 Maintenance processes for mid-level, mixed-phase clouds. In this stage, a delicate balance exists between the condensate supply rate, the bulk ice crystal growth rate, the dry air entrainment rate, and the amount of sedimentation. The circulation has to be strong enough to produce more liquid water, but not so strong that dry air is entrained too rapidly. The amount of ice nuclei also appears to be important for maintaining the cloud against rapid glaciation. Sedimentation of large ice from the base of the cloud may moisten the layer beneath by sublimation to the point where a new cloud layer is formed.**

other words, insufficient differential heating causes the circulations to cease; on the other hand, too much differential heating and the radiatively induced circulations may cause excessive dry air entrainment, leading to cloud dissipation.

Without the lifting to produce more liquid water through condensation, the cloud may glaciare rapidly and ice sedimentation will remove the remaining water from the cloud. Therefore, there must also be a balance between ice water production and sedimentation as indicated by Harrington et al. (1999). During one of their mixed-phase cloud simulations, a cloud underwent rapid glaciation at the four-hour point, as ice was rapidly produced at the expense of the liquid water. The ice was then removed through sedimentation for the next hour, as the lwc slowly increased while iwc remained quasi-constant through the rest of the simulation. This set of processes allowed the cloud to persist in a self-maintaining state for an extended period of time, leading the authors to propose that ice crystal sedimentation is of prime importance to the stability of the cloud layer. Also, deposition rates must be small enough so that the cloud lwc is not depleted; the cloud layer can only persist as long as the lwc is sufficient to continue driving weak eddies through radiative cooling.

The above discussion points to ice concentration as a key ingredient for the maintenance of mixed-phase clouds. Ice concentrations affect the net depositional growth, the production of large ice crystals, and directly and indirectly affect cloud top radiative cooling rates (Harrington et al., 1999). Larger ice concentrations increase in-cloud residence times by reducing ice crystal sizes, causing faster reductions in lwc. Low ice concentrations, on the other hand, reduce the depletion of liquid drops by the Bergeron-Findeison process, allowing the water drops to persist. In this manner, the

condensate supply rate remains greater than the bulk ice crystal mass diffusional growth rate, and the cloud layer stays intact.

Pinto (1998) found that the lifetime for liquid and ice to coexist in a cloud is a function of cooling rate and the concentration of ice-forming nuclei. Specifically, he states that strong cloud top radiative cooling rates (producing water supersaturation), depleted numbers of ice-forming nuclei, and minimum secondary ice particle production allow for the coexistence of both phases for extended periods of time. Liu and Krueger (1998) were able to successfully maintain simulated all-water altocumulus clouds in a mixed-layer model by allowing the cloud base to detrain at a rate that maintained a constant ratio of buoyant consumption of turbulent kinetic energy in the sub-cloud layer to buoyant production in the cloud layer. Finally, Tulich and Vonder Haar (1998) found that smaller-sized liquid water droplets in an observed altocumulus cloud led to substantially larger radiative heating and cooling rates, implying more intense circulations. Therefore, the sizes and concentrations of the liquid drops also affect the longevity of mid-level clouds.

### **7.3 Dissipation Processes**

In the simplest terms, cloud dissipation results when any of the aforementioned formation or maintenance processes breaks down (see Fig 7.3). For example, if warming due to the combination of latent and shortwave heating becomes greater than the longwave and evaporative cooling at cloud top, the layer will become increasingly stable, the internal circulations will cease, liquid water will no longer be produced, and the cloud will dissipate (e.g., Stephens (1978) found that the absorption of shortwave energy can

## Dissipation:

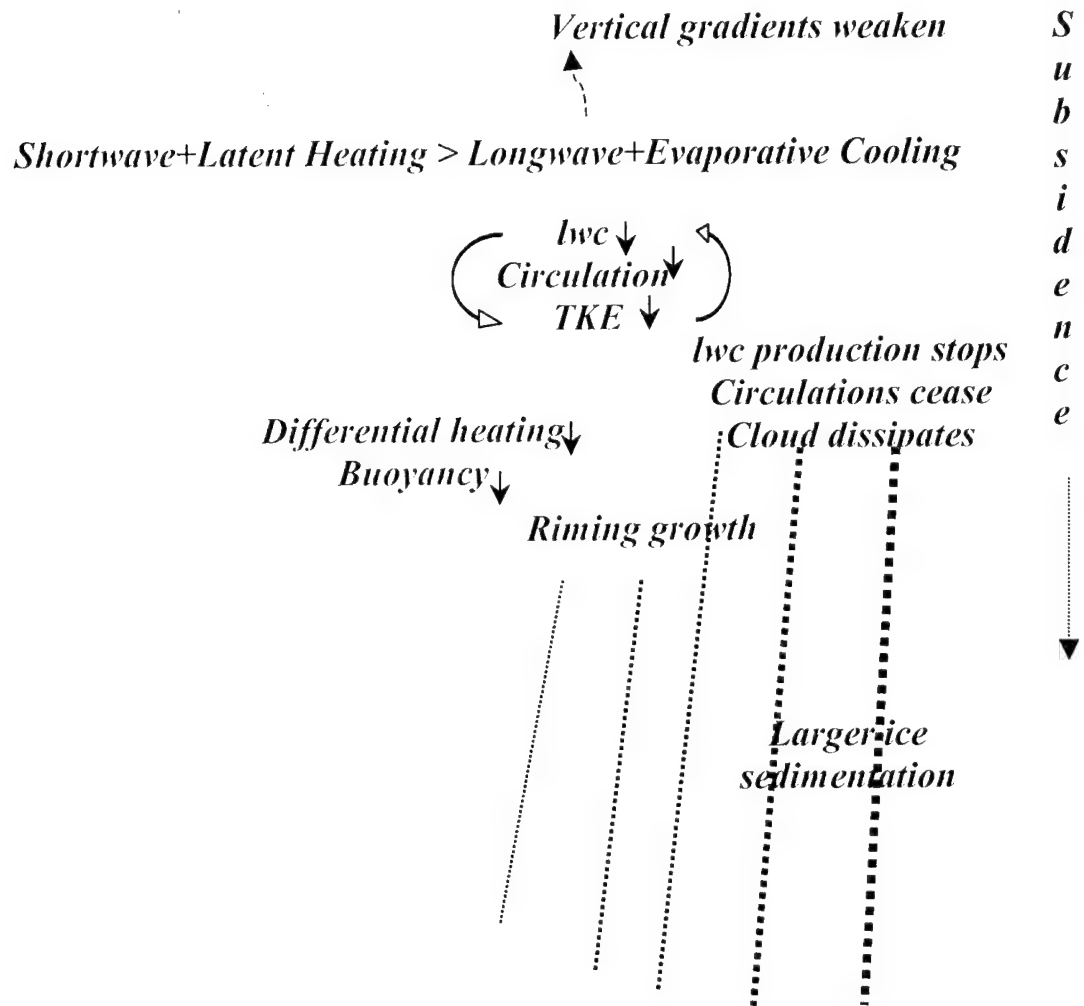


**Fig 7.3** Dissipation mechanisms for mid-level, mixed-phase clouds include large-scale subsidence drying, loss of cloud water mass by excessive sedimentation of ice particles from the cloud, excessive dry air entrainment, or a change in the net radiative heating balance of the cloud. Differential vertical radiative heating is critical for maintaining cloud circulations, so if shortwave and latent heating overcome longwave and evaporative cooling at cloud top, the cloud will dissipate.

produce cloud top heating on the order of 5° C per hour in altostratus clouds).

Alternatively, if the vertical differential heating becomes too large, vigorous convection will result in updraft penetration into the stable overlying air where the detrained cloud water will evaporate, eventually causing the cloud to mix itself out of existence. In short, any mechanism that negates liquid water production or uses the liquid water at a faster rate than it can be produced will lead to cloud dissipation.

Tiedtke's (1993) formulation for cloud dissipation involves evaporative dissipation due to terms involving descent and turbulent mixing. Large-scale subsidence is indeed a key mechanism for causing cloud decay, as demonstrated in the next chapter. Stephens et al. (1990) further showed that dynamic and turbulent motions, induced mainly by radiative warming, also alter clouds. These alterations can act to enhance cloud lifetime or destroy it, depending on the microphysics and the strength of the motions.

One of the main ways to "kill" a mid-level, mixed-phase cloud is through glaciation (e.g., Hobbs and Rangno, 1985). It was previously mentioned that cloud maintenance is highly dependent on the balance between ice water production and sedimentation (Harrington et al., 1999), as well as the concentration of ice-forming nuclei (Pinto, 1998). If the deposition rate becomes too high with respect to the rate of liquid water production, the ice particles may become large enough to initiate riming with high collection efficiency. If this occurs, the ice will quickly grow at the expense of the available liquid water and the cloud will rapidly glaciate. The relatively large ice particles will then be removed from the cloud by sedimentation. Likewise, if the

concentration of ice-forming nuclei is too large, the lwc will erode rapidly and also cause the demise of the cloud. Both of these processes are equivalent to Rauber and Tokay's (1991) bulk ice crystal growth rate becoming larger than the condensate supply rate, which is a death knell for the mixed-phase cloud. It is somewhat amazing that mixed-phase clouds are as prevalent as they seem to be, given the extremely delicate balances between the condensate supply rate, the concentration of ice-forming nuclei, the ice deposition rate, and the sedimentation rate.

## **8. The Death of an Altocumulus Cloud**

The possible mechanisms for mid-level, mixed-phase cloud dissipation were discussed in Section 7.3. This chapter focuses on a subset of mid-level clouds, namely altocumulus clouds, and the specific processes that caused the “death” of the cloud during the 11 Nov 99 Lagrangian aircraft measurement.

### **8.1 Altocumulus Cloud Description and Problem Statement**

Altocumulus clouds reside in the mid-troposphere, contain rounded (often convective) elements, are thin (on the order of one hundred meters), and precipitate little if at all (Heymsfield, 1993). These clouds are of intellectual interest primarily because, unlike many boundary layer clouds, they cannot be maintained by surface moisture fluxes. Therefore, for altocumulus clouds, it is more natural to study the growth and decay problems rather than the steady-state problem. Second, large-scale vertical velocity is a stronger forcing on mid-level clouds than on boundary layer clouds, because vertical velocities become small near the ground. Third, unlike mid-latitude or tropical boundary layer clouds, we have previously shown that mid-level clouds are often mixed-phase. Altocumulus clouds are also of practical interest, as changes in anthropogenic aerosols may change the albedo (Twomey, 1974) and emissivity (Garrett et al., 2001) of altocumulus clouds, thereby affecting the climatic radiation balance.

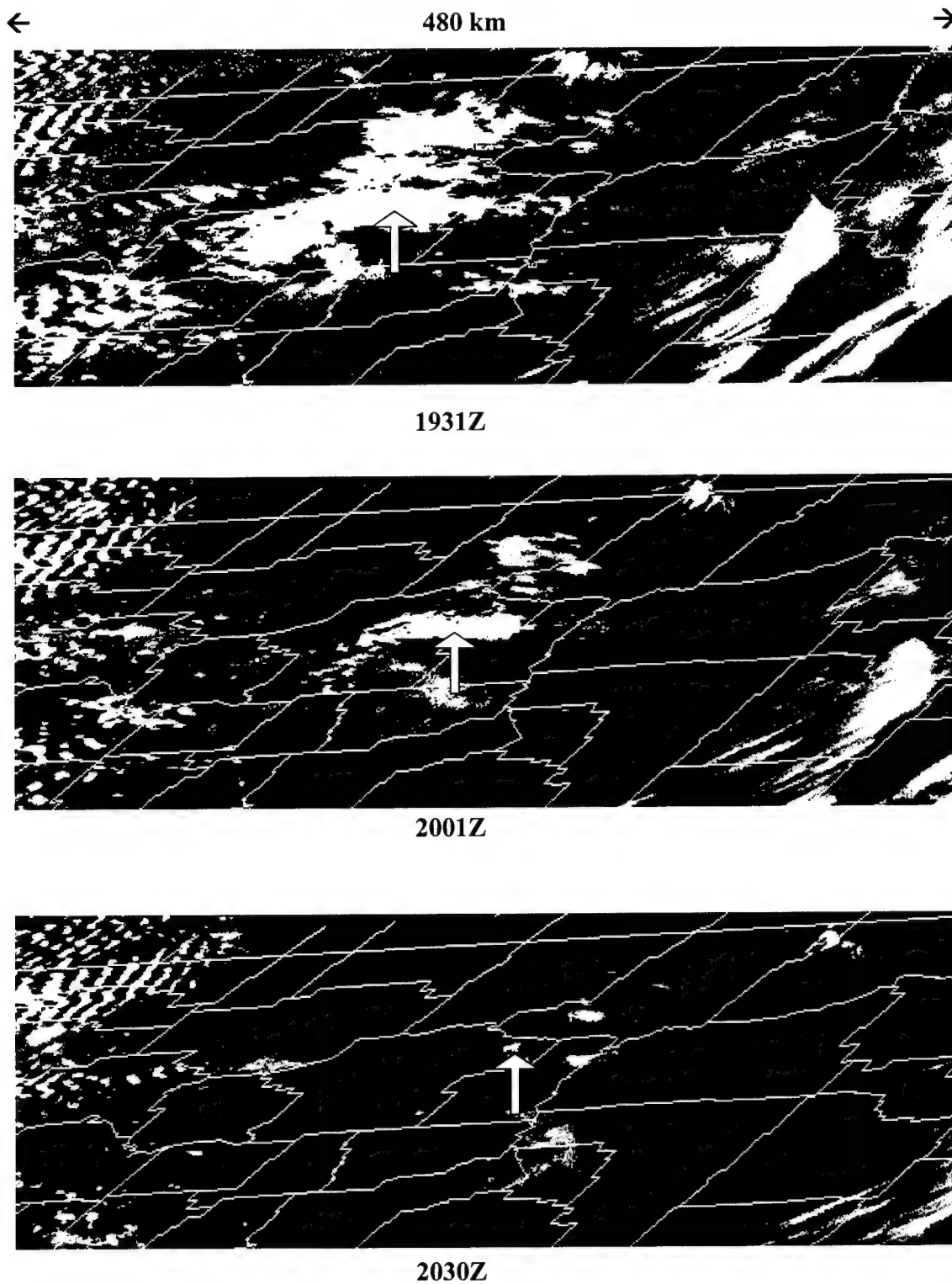


**Fig 8.1** Time series of GOES-8 visible satellite images of the 11 Nov 99 cloud that coincides with the time of the CLEX-5 Lagrangian aircraft measurements. The

**focus of this part of the study was to determine the physical mechanisms responsible for the “death” of the mid-level, mixed-phase cloud shown at the tip of the arrow.**

In this section, we analyze the Lagrangian aircraft measurements of an altocumulus cloud that occurred on 11 November 1999 over Montana. The aircraft arrived during the decay phase and continued sampling until the cloud disappeared. Figure 8.1 shows a series of visible satellite images that roughly coincide with the time of the aircraft measurements. When the measurements commenced, the cloud extended vertically from 5180 m to 5705 m and covered an area of about 6000 km<sup>2</sup>. The cloud was mixed-phase, but predominantly supercooled liquid water, as shown in Figure 5.7.

The primary question we address here is “What caused the death of this mid-level cloud?” There are four possible culprits: large-scale subsidence, radiative heating, entrainment drying, and sedimentation fallout. An estimate is made to determine which of these four processes contributes most to the decay and eventual dissipation of the cloud observed on 11 Nov 99. To accomplish this, a budget is constructed for the vertically averaged specific liquid water content,  $q_l$ . The budget helps elucidate whether the lifetime of the 11 Nov 99 altocumulus cloud is limited by microphysics or dynamics.

## **8.2 Budget of Liquid Water**

Because the ice water content is small in this case and has little effect on radiative cooling, the budget neglects ice for this case, except insofar as it removes liquid via sedimentation. The time-rate of change of specific liquid water content,  $q_l$ , is affected by four primary processes:

$$\frac{dq_l}{dt} = Subs + Entr + Rad + Sed ,$$

where the right-hand side represents subsidence, entrainment, radiation and sedimentation, respectively. We assume the cloud is saturated with respect to water. The subsidence drying is then given by:

$$Subs = \left( \frac{\partial q_l}{\partial p} \right)_{\theta_l, q_l} w_s \frac{dp}{dz},$$

where  $w_s$  is the cloud-average subsidence velocity,  $p$  is pressure,  $\theta_l$  is the liquid water potential temperature, and  $q_l$  is the total specific water content, which includes vapor and liquid, but not ice. We use the entrainment drying equation from Randall (1984):

$$Entr = \left( \frac{\partial q_l}{\partial q_t} \right)_{\theta_l, p} \frac{w_e \Delta q_t}{h} + \left( \frac{\partial q_l}{\partial \theta_l} \right)_{q_t, p} \frac{w_e \Delta \theta_l}{h},$$

where  $w_e > 0$  is the entrainment velocity,  $h$  is the depth of the cloud,  $\Delta q_t$  is the change of  $q_t$  from just above to just below cloud top, and  $\Delta \theta_l$  is the analogous difference for  $\theta_l$ . The radiative cooling term is given by:

$$Rad = \left( \frac{\partial q_l}{\partial \theta_l} \right)_{q_l, p} \left( \frac{p_0}{p} \right)^{\left( \frac{R_d}{C_{pd}} \right)} \dot{Q},$$

where  $\dot{Q}$  is the radiative cooling rate,  $p_0$  is a reference pressure,  $R_d$  is the gas constant for dry air, and  $C_{pd}$  is the specific heat of dry air at constant pressure. Loss of water via sedimentation of ice crystals is given by:

$$Sed = \frac{\sum_i N_{im} m_i v_{t,i}}{\rho_a h},$$

where  $N$  is the number concentration of ice crystals in the  $i$ th 2D-C particle size bin,  $m$  and  $v_t$  are the mass and terminal velocity of a crystal in the  $i$ th 2D-C particle size bin, respectively, and  $\rho_a$  is the density of air.

### **8.3 Methods Used to Evaluate Terms in the Liquid Water Budget**

The above terms in the budget are evaluated using aircraft data and numerical models as follows:

#### **8.3.1 Horizontal Advection**

Horizontal advection of liquid water is not contained explicitly in the liquid water budget, because we used a Lagrangian flight pattern. The flight pattern consisted of a spiral sounding, followed by a series of racetrack-shaped patterns at different altitudes. While executing this pattern, the aircraft drifted with the horizontal wind (see Figure 3.1). Since the racetracks in the figure overlap to a large degree, we can assume that measured changes in liquid water reflect temporal changes following a column of air, not spatial inhomogeneity. Therefore, the horizontal advection term is omitted in the budget.

#### **8.3.2 Large-scale Subsidence**

Large-scale subsidence tends to warm a mid-level cloud, depleting its liquid water. However, the vertical velocity averaged over the area of the mid-level cloud on 11 Nov 99 was too small to be measured by aircraft probes. This quantity could not be computed from radiosonde soundings either, because only two sites were available over Montana.

In order to estimate large-scale vertical velocity over the flight area, we used a numerical model, as in Bretherton et al. (1995). Specifically, the forecast came from the Fifth-Generation NCAR/Penn State Mesoscale Model (MM5) hosted on the University of Utah system. The forecast was initialized at 1200 UTC on 11 November 1999 and was

run at 36-km horizontal grid spacing. The model's vertical velocity field is shown in Figure 8.2. When the cloud formed at approximately 1500 UTC, the air motion was upward at several  $\text{cm s}^{-1}$ . By 1800 UTC, when the cloud began to decay, the vertical velocity was downward at about  $-3 \text{ cm s}^{-1}$ . The velocity was still roughly  $-3 \text{ cm s}^{-1}$  at 2100 UTC, after the cloud dissipated.

The gentle upward and subsequent downward motion appears to be associated with an upper-tropospheric patch of high potential vorticity (PV) that breaks off from a trough and is advected eastward over Montana (see Figure 8.3). Beneath the high PV anomaly, isentropes bow upward. Therefore, as high PV aloft approaches from the west, a mid-level parcel rises along an isentrope. Later, as the PV patch moves off to the east, the parcel descends back to nearly its original altitude (Hoskins et al. 1985).

### 8.3.3 Entrainment

To compute the entrainment velocity ( $w_e$ ), we use the flux-jump method; that is, we set  $w_e = \overline{w'q'_t} / \Delta q_t$ , where  $\overline{w'q'_t}$  is the turbulent flux of  $q_t$  just below cloud top. Since there was no detectable jump in  $\theta_t$  or  $q_t$  at the base of the cloud, entrainment into the base can be neglected. To compute  $\overline{w'q'_t}$ , we use the two legs (3a and 3b) of a racetrack sampled at 100 m below cloud top. The data are conditioned following Bretherton et al. (1995) and Stull (1988). For leg 3a,  $w_e = 1.1 \text{ cm s}^{-1}$ , and for leg 3b,  $w_e = 0.75 \text{ cm s}^{-1}$ . The uncertainty of up to a factor of two in the entrainment rate is introduced by poor sampling due to the short leg lengths (Lenschow and Kristensen, 1985). In the liquid water budget below, we use  $0.9 \text{ cm s}^{-1}$ , which is the average of  $w_e$  over legs 3a and 3b.

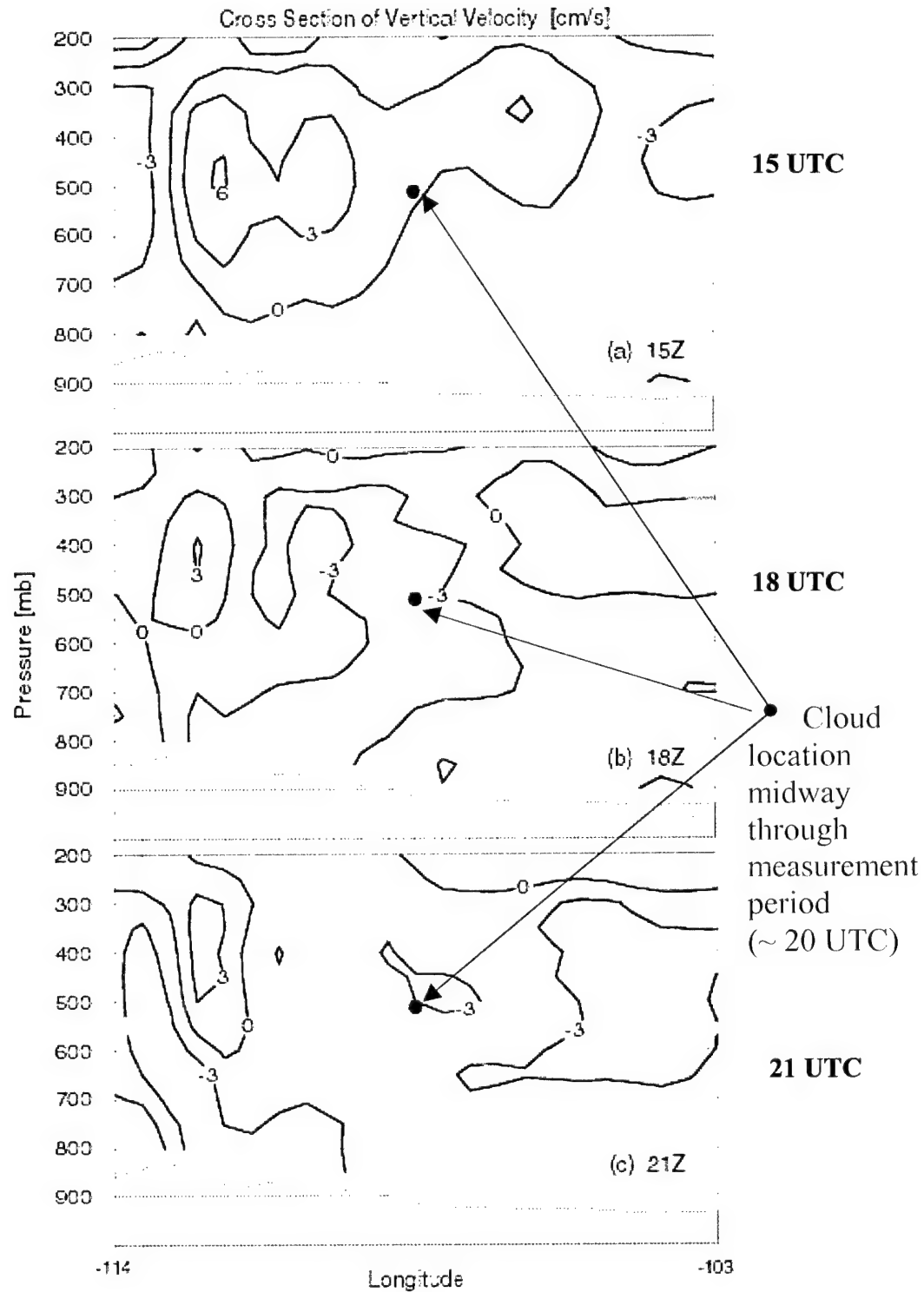


**Fig 8.2** Cross-section of MM5 forecast vertical velocity ( $\text{cm s}^{-1}$ ) initialized 12 UTC on 11 November 1999. The air motion is upward at several  $\text{cm s}^{-1}$  at 1500 UTC, decreases to downward at about  $-3 \text{ cm s}^{-1}$  by 1800 UTC as the cloud starts to decay, and remains at  $-3 \text{ cm s}^{-1}$  by 2100 UTC, after the cloud dissipates.

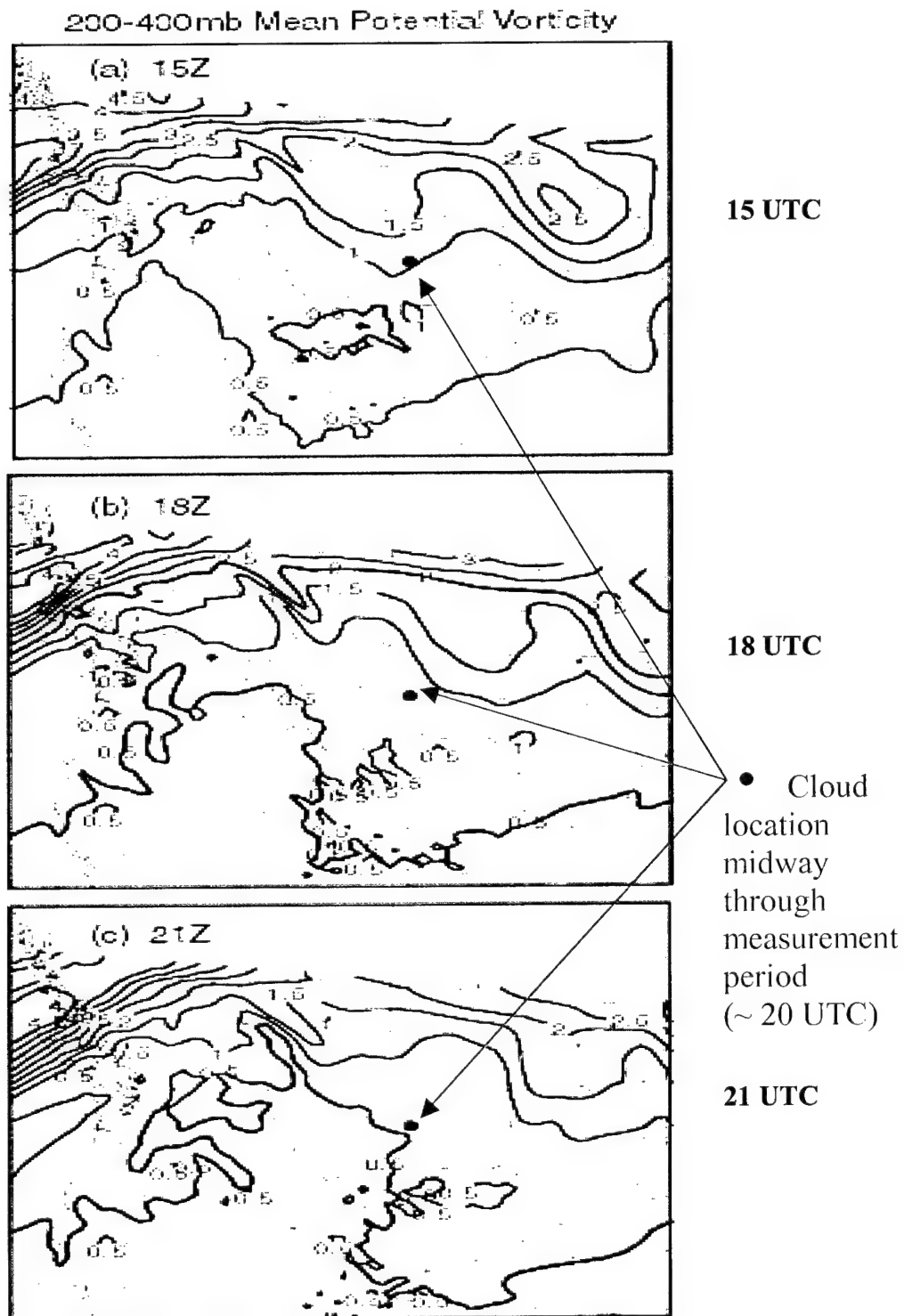


**Figure 8.3** The change in vertical velocity seen in Fig 8.2 is associated with an upper-level patch of high potential vorticity that breaks off from a trough and is advected eastward, as shown in the above MM5 forecast output. Mean 200-400 mb PV values decrease through the period from 1.1 at 15Z to just over 0.5 at 21Z.

### 8.3.4 Radiative Cooling

A new two-stream radiative transfer model (Stephens et al., 2000) is used to obtain the cloud-averaged heating due to solar and infrared radiation. This model is described in more detail in Chapter 9. As input, the aircraft liquid and ice water content profiles through the cloud are merged with a routine radiosonde sounding launched from Great Falls, Montana at 0000 UTC on 12 November 1999. The net total cloud-averaged heating rate is  $-7.6 \times 10^{-5} \text{ K s}^{-1}$ . A sensitivity analysis of the heating rate to liquid water content showed that the value changed by about 25% if the liquid water was doubled or halved everywhere.

### 8.3.5 Sedimentation

Due to sedimentation, ice crystals of several hundred micron diameters fell from the cloud base. The CPI revealed that these particles were typically unrimed broad-branched crystals (P1c), although a few crystals were needle-shaped and/or slightly rimed. The broad-branched habit is consistent with the observed cloud temperature range of  $-12$  to  $16^\circ \text{C}$ . The sedimentation rate is computed using 2D-C data obtained from four in-cloud aircraft legs (2a, 2b, 7a, and 7b) near the cloud base. Using the ice crystal mass and terminal velocity formulation of Mitchell (1996), a maximum sedimentation rate of  $4.4 \times 10^{-7} \text{ kg m}^{-2} \text{ s}^{-1}$  was found for leg 7a, a minimum rate of  $2.9 \times 10^{-9} \text{ kg m}^{-2} \text{ s}^{-1}$  from leg 7b, and an average rate over all four legs of  $1.3 \times 10^{-7} \text{ kg m}^{-2} \text{ s}^{-1}$ . This gives a sense of the uncertainty due to sampling error, as the values vary by a couple of orders of magnitude.

Uncertainty in the sedimentation rate is also introduced by the mass and terminal velocity formulations. Following the method of Kajikawa (1989), the average

sedimentation rate was found to be nearly four times larger, or  $3.9 \times 10^{-7} \text{ kg m}^{-2} \text{ s}^{-1}$ . In the liquid water budget below, we chose to use the average sedimentation rate as computed by Mitchell (1996), because it does not represent particles as spheroids, it is general for any ice particle shape and size, it is conceptually and mathematically simple, it appears accurate, and it provides for physical insight. Most importantly, though, this method allows fall speeds to be determined from aircraft measurements of ice particle mass and projected area, rather than directly measuring fall speeds.

Finally, uncertainty is introduced by the fact that the 2D-C probe cannot detect particles larger than 1056 microns in diameter, and a few particles larger than this were seen in the CPI imagery. However, the number of missed particles is estimated by smoothly extrapolating the ice spectrum to large sizes, assuming an exponential ice number concentration. In the extreme, use of the 2D-C values in this formulation may cause a factor of two underestimation of the sedimentation rate.

#### **8.4 Discussion of the Magnitude of Terms in the Liquid Water Budget**

The main result of the liquid water budget analysis is shown in Table 8.1, which lists the rate at which each of the four aforementioned processes tends to deplete cloud liquid water. Accounting for all four processes, assuming the liquid water decreases at a constant rate, and taking the initial liquid water content to be the vertical average of the aircraft sounding, the cloud decay time is calculated to be 61 minutes. This is consistent with the observed decay time between the aircraft sounding and the death of the cloud, which was approximately 74 minutes.

**Table 8.1 Results of liquid water budget analysis. Large-scale subsidence was the dominant mechanism causing the dissipation of the 11 Nov 99 cloud system.**

<b>Budget Term</b>	<b><i>Liquid Decay Rate [kg/kg /s]</i></b>	<b><i>(Term Decay Rate) / (Subsidence Decay Rate)</i></b>
<b>Subsidence</b>	$-3.3 \times 10^{-8}$	1.0
<b>Radiation</b>	$+1.0 \times 10^{-8}$	-0.30
<b>Entrainment</b>	$-1.5 \times 10^{-8}$	0.44
<b>Sedimentation</b>	$-3.6 \times 10^{-10}$	0.011

The largest term in the liquid water budget is subsidence drying. The magnitude of the model-produced vertical velocity ( $-3 \text{ cm s}^{-1}$ ) is corroborated by the fact that this subsidence rate is consistent with the observed decay time of the cloud and the other terms in the liquid budget. Even if the model subsidence velocity were overestimated by a factor of two, subsidence drying would still be the dominant term.

The next two largest terms are entrainment, which tends to dry the cloud, and radiation, which tends to cool the cloud and hence increase liquid water. To a large degree, these two terms offset each other. This is interesting, because in this cloud it appears that the turbulence and resulting entrainment were generated by radiation, not shear. Therefore, radiation increases liquid water by direct cooling, but this moistening effect is compensated by radiatively induced entrainment. This is further complicated by

entrainment causing the cloud top to rise, cool, and hence experience increased liquid water. Given the uncertainty in our measurements and calculations, it is not obvious whether the net effect of radiation is to prolong or curtail the lifetime of the cloud.

By far the smallest term in the budget was drying due to sedimentation fallout of ice particles. This was somewhat surprising, because the flight scientists observed virga, and the cloud top height decreased rapidly at the end of the cloud lifetime, possibly due to sedimentation. Because the biggest ice particles are most subject to sedimentation, a relatively large amount of mass is removed from the cloud via this mechanism. However, even assuming imperfect measurements, it is unlikely that the sedimentation term exceeded 20% of the subsidence term.

## **8.5 Post-Mortem of the Death of an Altocumulus Cloud**

The picture that emerges from the liquid water budget analysis is that the evolution of the 11 Nov 99 cloud was governed primarily by large-scale ascent and then subsidence. The largest contributor to decay of liquid water is subsidence drying and the smallest contributor is sedimentation. The role of radiative cooling is interesting: radiative cooling directly increases liquid water, but radiatively induced entrainment drying offsets this increase. For this reason, it is difficult to ascertain whether the net effect of radiative cooling is to maintain the cloud or cause its dissipation. It may depend on some critical threshold strength of the circulation. If the circulation is under this threshold, the condensate supply rate allows the cloud to persist; once it exceeds the critical threshold, dry air entrainment overcomes the rate of liquid water production and the cloud begins to decay.

Because radiation and entrainment in this altocumulus case partially offset each other, and because sedimentation was weak, a similar cloud-decay time would have been obtained if all of the terms except subsidence had been ignored. Therefore, it appears that a fundamental difference between altocumulus and boundary layer clouds is that the link between large-scale vertical velocity and cloud lifetime is stronger for altocumulus clouds than for boundary layer clouds. Clouds near the ground are often maintained by surface moisture fluxes and experience relatively small large-scale vertical velocities. For example, the mid-level subsidence rate during dissipation of the 11 Nov 99 cloud was approximately  $3 \text{ cm s}^{-1}$ , compared to subsidence rates of less than  $1 \text{ cm s}^{-1}$  for boundary layer clouds measured during the ASTEX Lagrangian flights (Bretherton et al., 1995).

It would be rash to generalize on the basis of a single case study, but if the lifetime of most altocumuli is governed by large-scale ascent and descent, then this has implications for the improvement of numerical models of mid-level clouds. Namely, it indicates that special attention should be devoted to the large-scale velocity and moisture fields, whereas most past observational studies of altocumuli have focused more on the cloud microphysics.

## **9. Radiative Effects and Sensitivities**

The cloud radiative properties were studied theoretically using the longwave and shortwave fluxes and heating rates calculated for each of the mid-level, mixed-phase clouds observed during the CLEX-5 experiment. The “BUGSRAD” single-column radiation code from the Colorado State University General Circulation Model (CSU-GCM, e.g. Randall, 1989) was chosen to perform the calculations because it allows for the explicit input of both liquid and ice profiles in the scheme. This is an advantage over the other radiation codes that were examined, because most models generate fluxes and heating rates based solely on the total liquid water content of the system, rather than the actual water phase.

This chapter includes a brief description of the BUGSRAD radiative transfer model, the fluxes and heating rates calculated using observed cloud data, and several sensitivity studies that examine the variability of the cloud radiative transfer to selected macro- and microphysical parameters. The final section discusses and lists some measured and calculated mid-level cloud radiative parameters for use in modeling and remote sensing studies.

### **9.1 BUGSRAD Model Description**

An overview of the theory, rationale, and parameterizations used to develop the CSU-GCM BUGSRAD code can be found in Stephens, et al. (accepted 2001). In

general, the model uses the two-stream method of solution to calculate radiometric fluxes and heating rates for six spectral bands in the shortwave and twelve in the longwave. Specifically, the radiation code utilizes Ritter and Geleyn's (1992) delta-Eddington approximation to the two-stream equation in the shortwave, and the constant hemispheric approximation to the two-stream equation in the longwave, as well as the adding method of Stephens and Webster (1979). The BUGSRAD radiation scheme includes gaseous, cloud, and surface absorption and scattering in a plane-parallel atmosphere. In addition, the scheme uses relations from Stephens et al. (1990) for computing cloud optical properties. The k-distribution from Fu and Liou (1992) and the AER CKD Version 2.1 water vapor continuum data (Clough, et al., 1989) are used in the gaseous absorption routines.

Aircraft microphysical measurements from the aircraft spiral soundings were used as model input through the depth of the cloud and extending a few hundred meters above and below cloud. Nearby radiosonde measurements were used to extend the vertical sounding through the troposphere and lower stratosphere. Climatological McClatchey (1972) atmospheric profiles were used to further extend the sounding from the top of the radiosonde data to a peak altitude of 70 kilometers. Vertical grid spacing of 30 meters was used through the cloud layer, and a slight amount of smoothing was used at the interface between the two datasets to ensure that no sharp discontinuities were artificially introduced into the model. The resulting BUGSRAD input profiles for the control cases are shown in Figure 9.1.

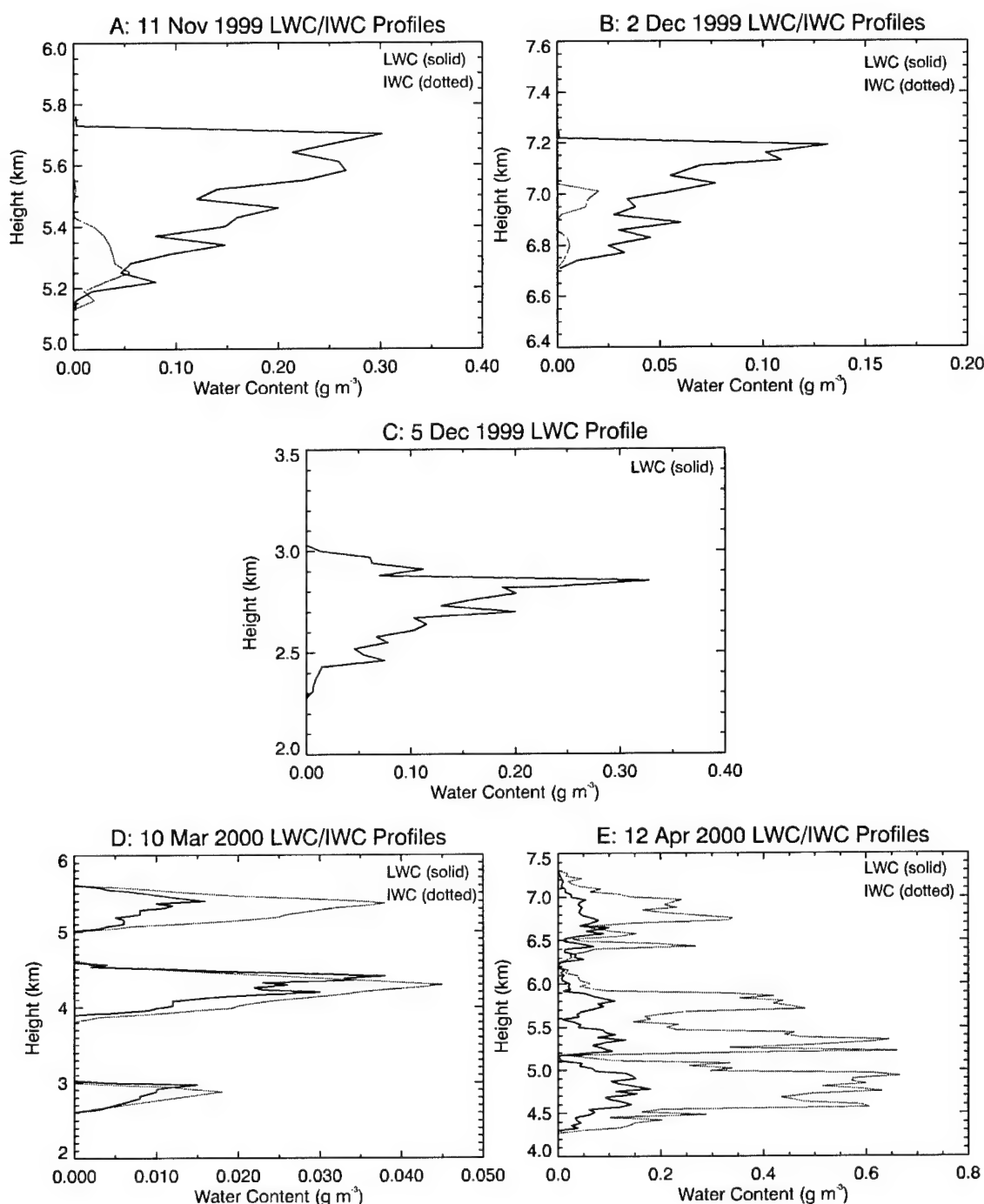


**Figure 9.1** BUGSRAD model lwc and iwc input profiles for A) 11 Nov 99, B) 2 Dec 99, C) 5 Dec 99, D) 10 Mar 00 and E) 12 Apr 00. The model profiles use observed lwc and iwc values at 30 m vertical grid spacing and capture the main features of the observed profiles shown in Figures 5.7–5.12.

## 9.2 Model Results

The results of the model calculations using the observed mid-level cloud profiles are plotted in Figures 9.2 through 9.6. For all of the flux diagrams, downward fluxes are depicted as solid lines; thick red lines for longwave and thin blue lines for shortwave. Similarly, upward fluxes are represented by dotted lines; again, red for longwave and blue for shortwave. The units of flux are given in Watts per square meter ( $\text{W m}^{-2}$ ) and are plotted against height from approximately one kilometer below cloud base to one kilometer above cloud top. The longwave and shortwave heating rates are shown for the same vertical distance above, through and below the respective cloud heights, in units of Kelvin per hour ( $\text{K hr}^{-1}$ ). Again, the thick red lines depict the longwave heating rates and the thin blue lines depict the shortwave heating rates. Positive values signify levels of radiative heating (flux convergence), while negative values are associated with radiative cooling (flux divergence) in a layer. The overall profiles show longwave cooling at cloud top and longwave heating in the bottom parts of the cloud. Generally, there is also a small amount of shortwave heating at the top of the cloud. The radiative profiles of the individual cases will now be examined in more detail.

Starting with the 11 Nov 99 case, the fluxes most affected by the mid-level cloud between about 5200 and 5700 m are the upward and downward shortwave fluxes, which each vary by more than  $300 \text{ W m}^{-2}$  from the top to the bottom of the layer. Much of this solar energy is reflected at cloud top or scattered by the cloud droplets, but there is a small amount of flux convergence that results in a maximum shortwave heating rate of  $2.5 \text{ K hr}^{-1}$  near the cloud top. Downward longwave fluxes increase by over  $220 \text{ W m}^{-2}$  toward the base of the cloud, while the upward longwave flux decreases by  $150 \text{ W m}^{-2}$ , as

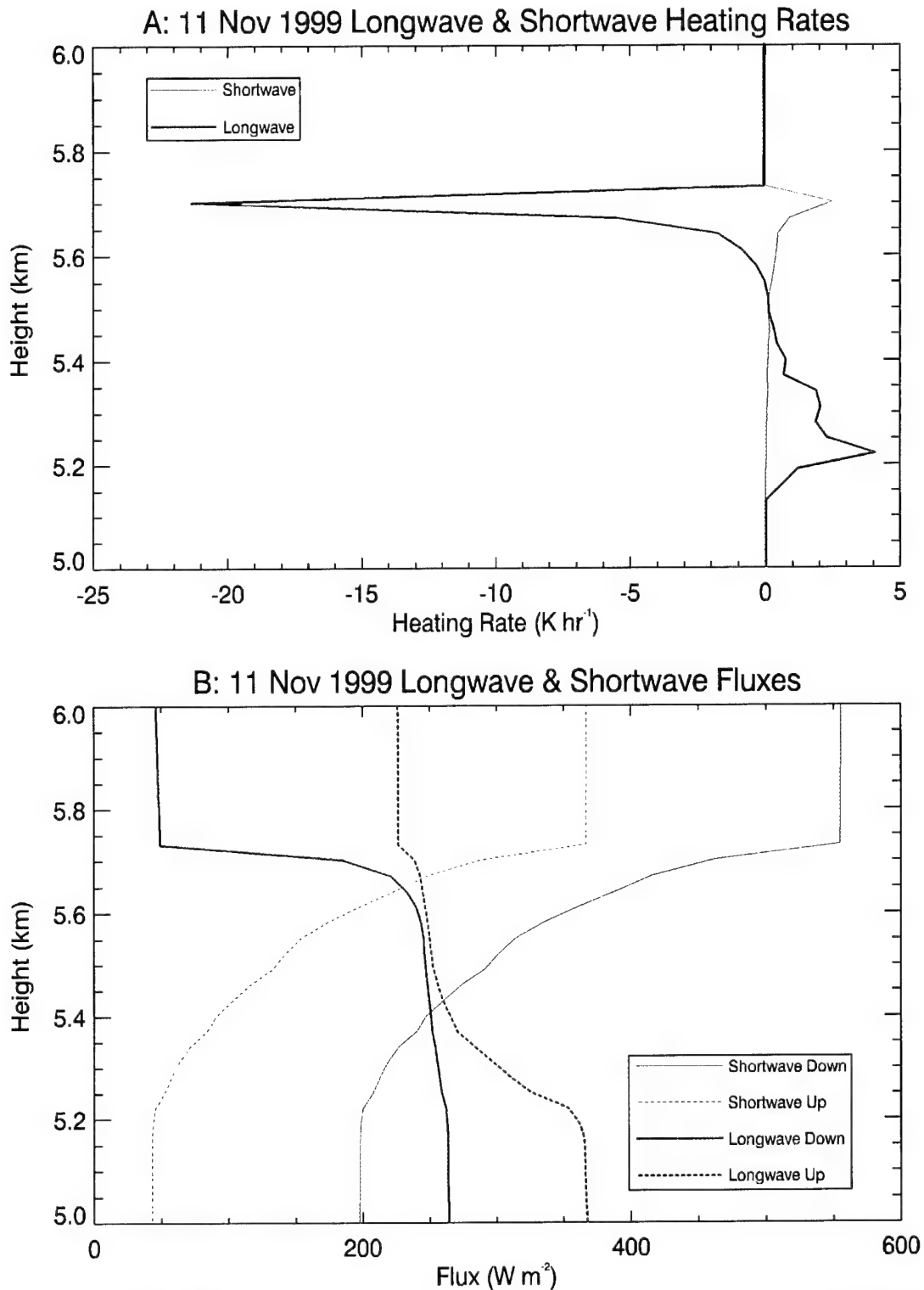


**Figure 9.2 BUGSRAD model longwave and shortwave heating rates (A) and fluxes (B) for the 11 Nov 99 cloud case. Longwave plots are red; shortwave plots are blue. Note the strong longwave cloud top cooling rate of  $21.3 \text{ K hr}^{-1}$  at 5700 m due to flux divergence. In contrast, the shortwave heating rate of  $2.5 \text{ K hr}^{-1}$  is relatively small.**

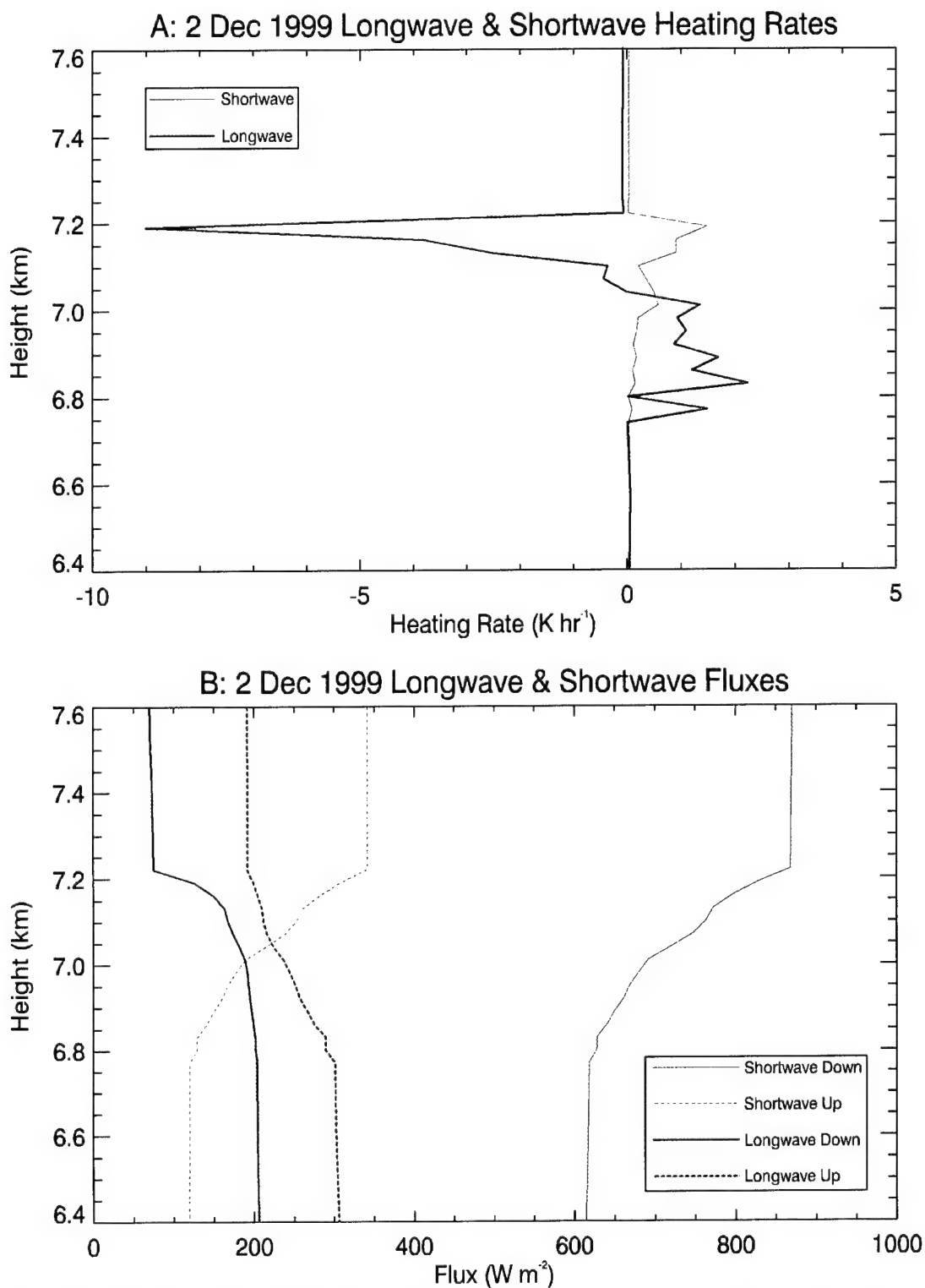


**Figure 9.3** Same as Fig 9.2 except for 2 Dec 99 heating rates and fluxes. Note the different scales. The maximum lwc for this case is half that of 11 Nov 99, resulting in smaller longwave and shortwave heating and cooling rates.

energy is mainly absorbed and reemitted by cloud droplets through the layer. This flux pattern results in a heating rate of  $4.1 \text{ K hr}^{-1}$  in the bottom third of the cloud, but is dominated by a  $21.3 \text{ K hr}^{-1}$  cooling rate at the cloud top. Recall that this cooling rate is associated with a relatively high liquid water content of  $0.30 \text{ g m}^{-3}$ , a cloud top temperature of  $16^\circ \text{ C}$ , and a height of  $5700 \text{ m}$ .

In comparison with the 11 Nov 99 case, the 2 Dec 99 cloud was over  $1500 \text{ m}$  higher and had about half the liquid water content. Notice that the downward shortwave flux is over  $300 \text{ W m}^{-2}$  higher than the 11 Nov case, due to the latitude and time (solar zenith angle) differences between the flights over Montana and Oklahoma. Although both the longwave and shortwave heating rates are nearly the same as the former case, the longwave cooling rate at cloud top is less than half, at just over  $9 \text{ K hr}^{-1}$ . Net radiational processes lead to longwave heating of the bottom half of the cloud at a rate of  $2.2 \text{ K hr}^{-1}$ , while the top half cools at about  $7.5 \text{ K hr}^{-1}$ , for a net heating to cooling ratio of three to one. This is in contrast to a ratio of about five to one for the 11 Nov 99 case.

Despite the relatively high lwc in the 5 Dec 99 case, the cloud top longwave cooling and cloud base heating rates of approximately  $3.4$  and  $0.23 \text{ K hr}^{-1}$ , respectively, are relatively small compared to the previous two cases. The shortwave heating rate for this case is especially small ( $0.08 \text{ K hr}^{-1}$ ) is because the flight occurred shortly after sunrise, resulting in a very low solar elevation angle. This effect is apparent in the flux profiles, as the downward shortwave flux is less than  $80 \text{ W m}^{-2}$ . The cloud top cooling occurs over a broad depth of  $150 \text{ m}$ , as opposed to a point maximum at the extreme cloud top seen in previous cases. The difference is due to the entrainment drying caused by a weak temperature inversion about  $200 \text{ m}$  below cloud top, as discussed in Chapter 5. The

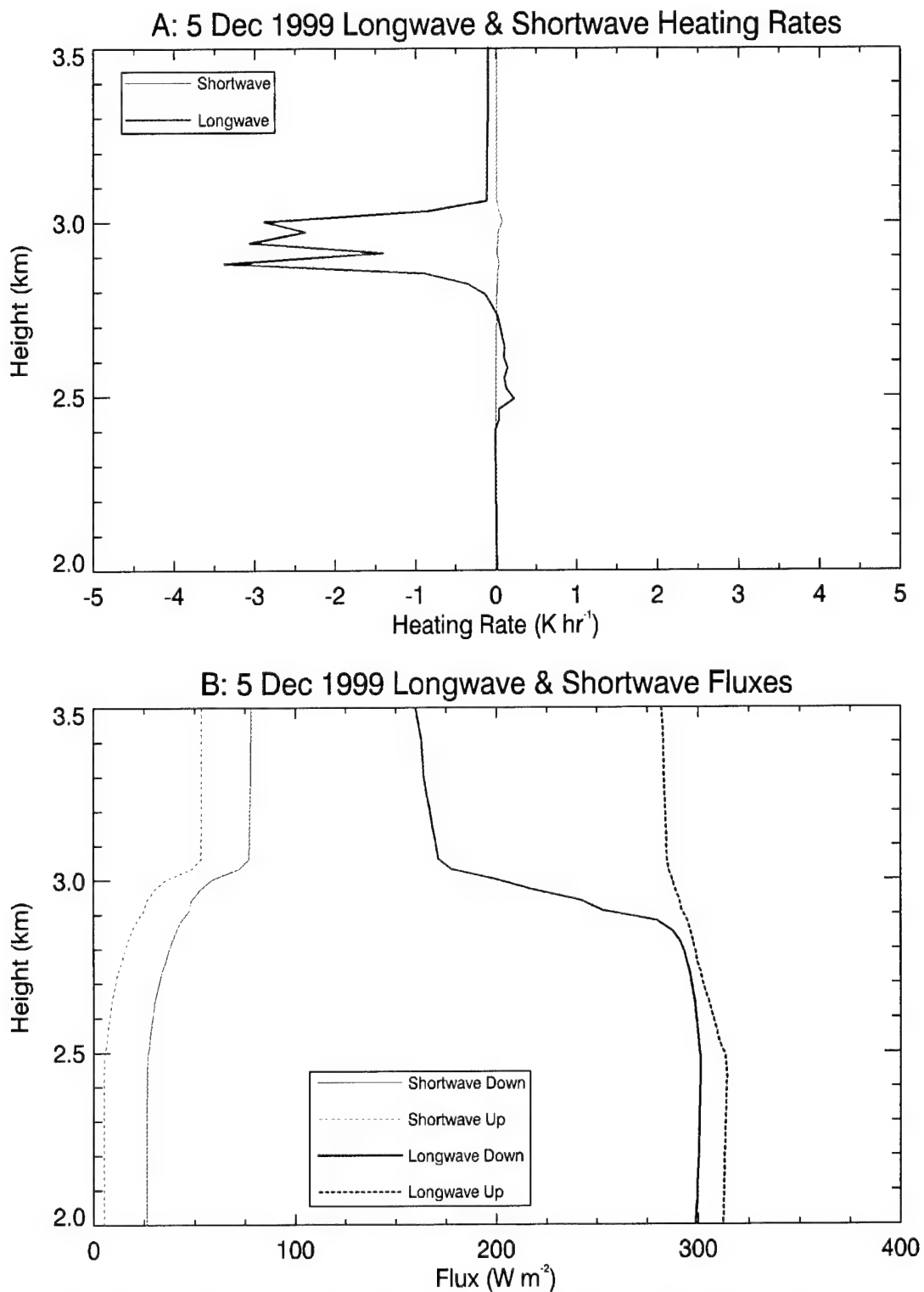


**Figure 9.4** Same as previous two figures except for 5 Dec 99. Despite having the largest maximum lwc of any case, the maximum cooling rate is a relatively modest  $3.4 \text{ K hr}^{-1}$ , because of a dry air entrainment-induced reduction in lwc at cloud top.

inversion decoupling resulted in an lwc maximum at 2880 m, instead of at the cloud top, which is where the maximum cooling occurs. As the lwc decreases above the inversion, so does the flux divergence; consequently, the radiative cooling to space decreases by nearly  $1 \text{ K hr}^{-1}$  at cloud top.

The increased downward shortwave flux of over  $880 \text{ W m}^{-2}$  on 10 Mar 00 is indicative of the change in seasons from near winter solstice during the December measurements to the near vernal equinox during the March flight. Both the radiative heating and cooling rates are very small in this case, with a maximum cooling rate of  $1.4 \text{ K hr}^{-1}$  at the top of the uppermost layer in the multi-layered cloud system. A secondary peak in the longwave cooling rate of approximately  $0.75 \text{ K hr}^{-1}$  is also evident at the top of the middle layer, but the bottom layer is barely discernible in the cooling rate profile. Small shortwave heating rates of  $0.35$  and  $0.21 \text{ K hr}^{-1}$  are also apparent in the top and middle layers, respectively.

In general, the reason for the low radiative heating and cooling rates in this system is the extremely low total liquid water content. This effect is most readily seen at the top of the uppermost layer, where there is no interference from other layers, yet the cooling rate is small. There are also some radiative transfer interactions between cloud layers, as lower layers absorb upwelling radiation from beneath them, as well as downward directed radiation from upper layers, and reemit the energy at their own effective cloud temperature. Radiation is also scattered multiple times from one cloud layer to another, creating a complicated overall radiative transfer picture.

Finally, the 12 Apr 00 case is interesting from two perspectives. First, it is another multi-layered cloud system; and second, it has relatively high liquid and ice water

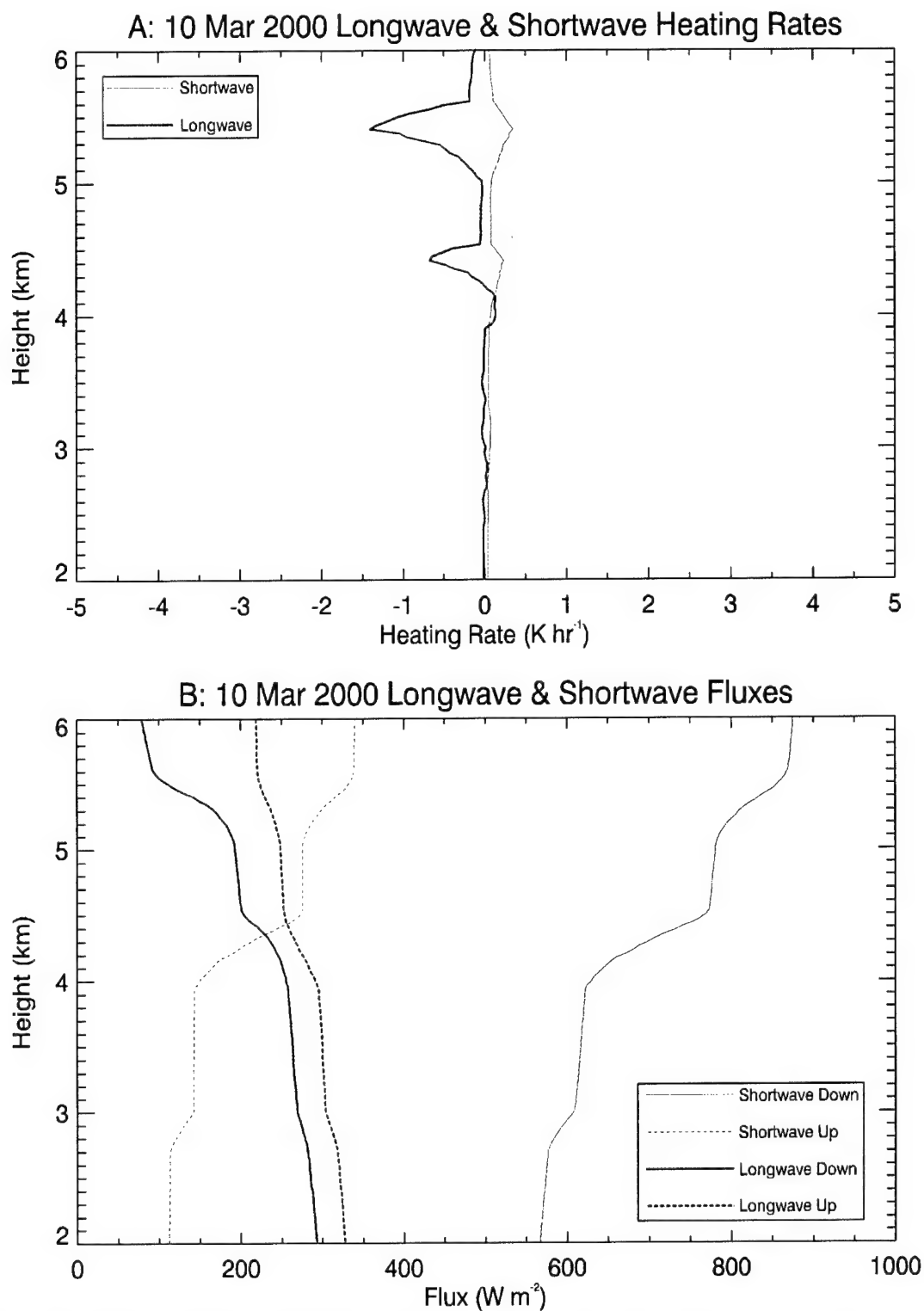


**Figure 9.5** Same as the previous three figures except for the multi-layered cloud of 10 Mar 00. Small lwc and iwc values result in small amounts of flux convergence and divergence, which equates to small net heating rates.

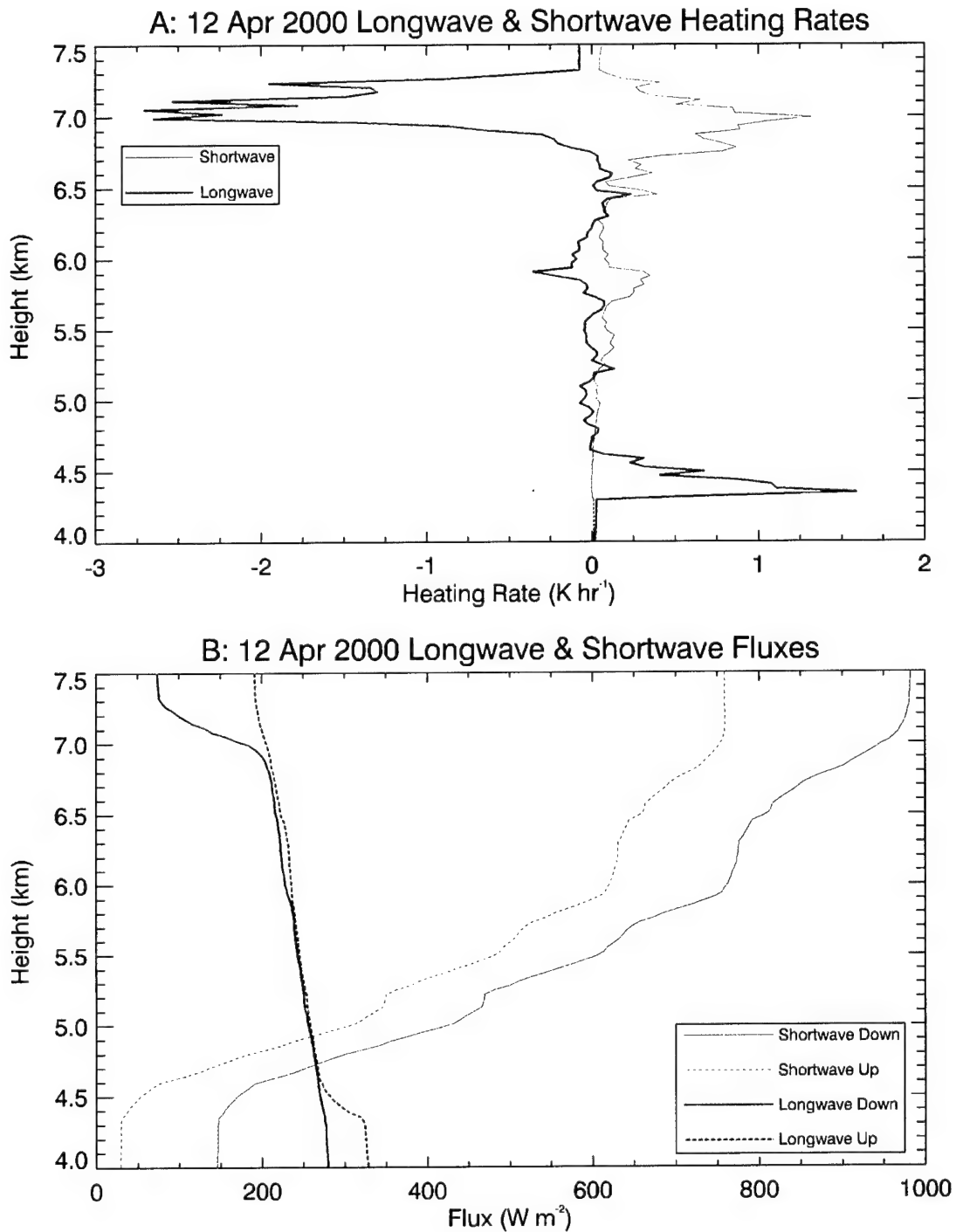


**Figure 9.6** Same as previous four figures except for 12 Apr 00. Despite relatively high amounts of lwc and iwc through this system, the maximum longwave cooling and shortwave heating rates are only  $2.7$  and  $1.3 \text{ K hr}^{-1}$ , respectively. This is due to lwc decreases at the top of the cloud and radiative interactions between the layers.

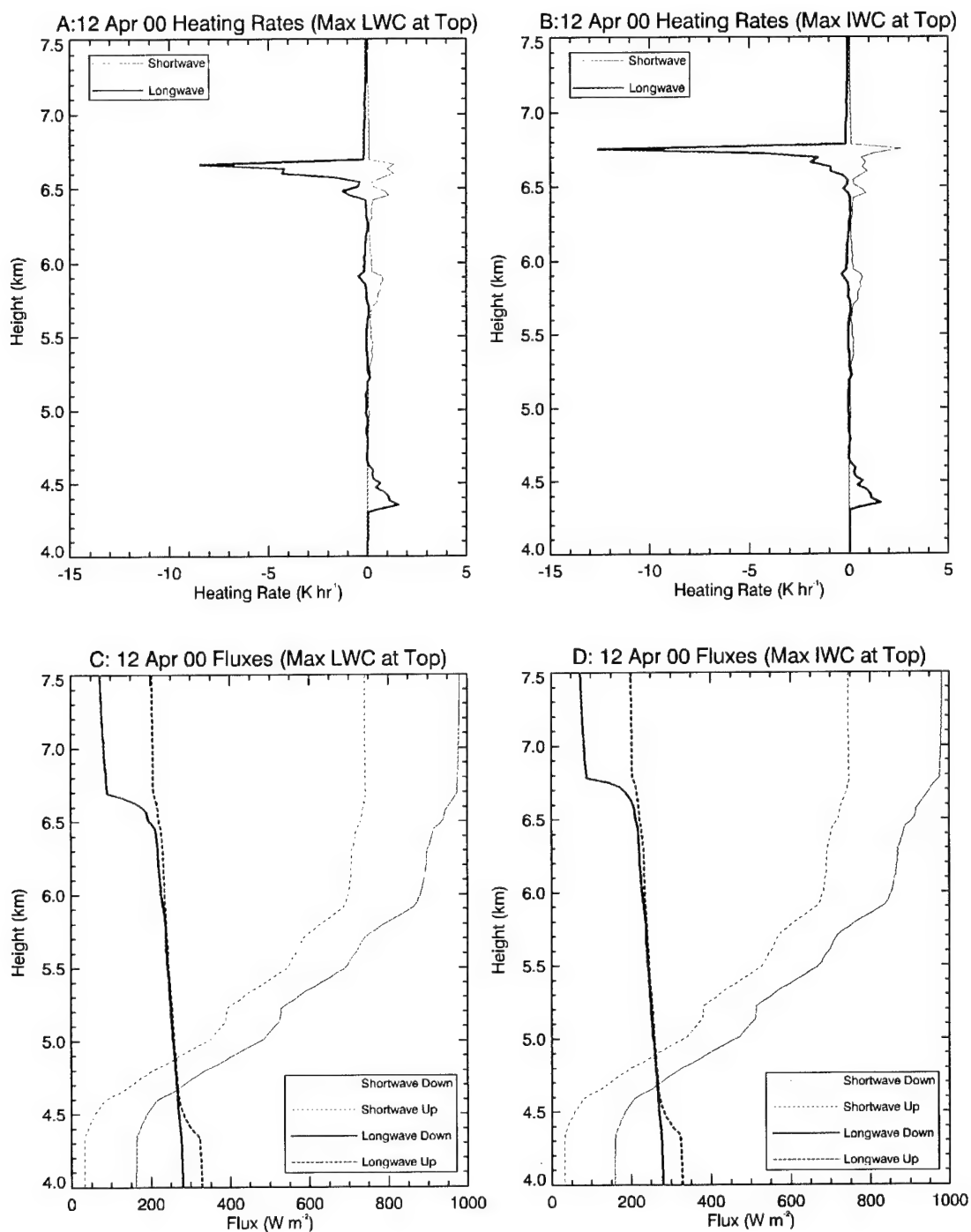


**Figure 9.7 Results of a sensitivity study on the 12 Apr 00 case (Fig 9.6) showing the increase in heating rate (top) and flux (bottom) when the maximum lwc is located at cloud top (A,C) or the maximum iwc is located at cloud top (B,D). Note that the maximum longwave cooling approximately triples for A and quadruples for B.**

contents throughout the depth of the profile. Also, unlike the single-layer cases, the lwc does not peak at the top, but tapers off to near zero over the top 250 m of the profile, as seen in Figure 9.1. Despite a liquid water content of  $0.18 \text{ g m}^{-3}$  at 6660 m, the maximum cooling rate is a relatively meager  $2.7 \text{ K hr}^{-1}$  at approximately 7000 m, where the lwc is only  $0.04 \text{ g m}^{-3}$ . The maximum shortwave heating rate ( $1.3 \text{ K hr}^{-1}$ ) is also at 7000 m, with no significant radiative heating or cooling below 6800 m to the bottom of the three-layer system, where there is a maximum longwave heating rate of  $1.6 \text{ K hr}^{-1}$ .

The radiative interactions above and below 6660 m cause the net heating effect to be nil at that level, despite the maximum lwc located there. This is due to downward-directed thermal emission from the layer above, which offsets the large cooling that would occur at the maximum lwc level if it were able to radiate directly to space. To make this point more clear, Figure 9.7 shows that the maximum cooling rate would increase to  $8.5 \text{ K hr}^{-1}$  if the maximum lwc were coincident with the cloud top, and to an even higher rate of  $12.6 \text{ K hr}^{-1}$  if the maximum iwc were located at cloud top. The small liquid water contents measured at cloud top are still sufficiently large to absorb and reemit energy, but at a much lower radiative rate. The result of this effect is that the maximum cloud top cooling and heating rates in this system are only 21 to 32% of what they would be if the maximum lwc or iwc were at cloud top. Therefore, the overall effect of small lwc and iwc amounts above a larger maximum is to “damp” the radiative cooling rate at the top of the cloud system.

### 9.3 Sensitivity Studies

Several sensitivity studies were done on the modeled cloud fields, in order to examine changes in the radiative heating and cooling rates due to variations of the macro- and microphysical profiles. The first modification was to double and halve the lwc and iwc from the original measured values for each case, which is described in section 9.3.1 and 9.3.2, respectively. Section 9.3.3 illustrates the sensitivity of radiative processes to the correct parameterization of liquid and ice water content in a cloud model. The solar elevation angle and the cloud height were then varied for the 2 Dec 99 cloud case in sections 9.3.4 and 9.3.5, respectively, to determine the impact of shortwave heating and density changes on the cloud radiative heating profile. Finally, section 9.3.6 addresses the effect of cloud layering on the radiative profiles, by examining changes that occur when various combinations of layers are removed from the original three-layered systems measured on 10 Mar 00 and 12 Apr 00.

#### 9.3.1 Sensitivity Study 1 – Doubling and Halving the Liquid Water Content

In order to determine the effect that the amount of liquid water has on the radiative flux and heating rate profiles, the lwc was both doubled and halved for each case, while holding all other parameters (including ice water content) at the same value as used in the measured lwc control run. These profiles were then used as input for more BUGSRAD model runs, with the results shown in Figures 9.8 through 9.12. As expected, the heating and cooling rates increased when the lwc was doubled and decreased when it was halved. The values for maximum longwave radiative cooling rate are shown in Table 9.1 for the control case, and the lwc doubling and halving cases,

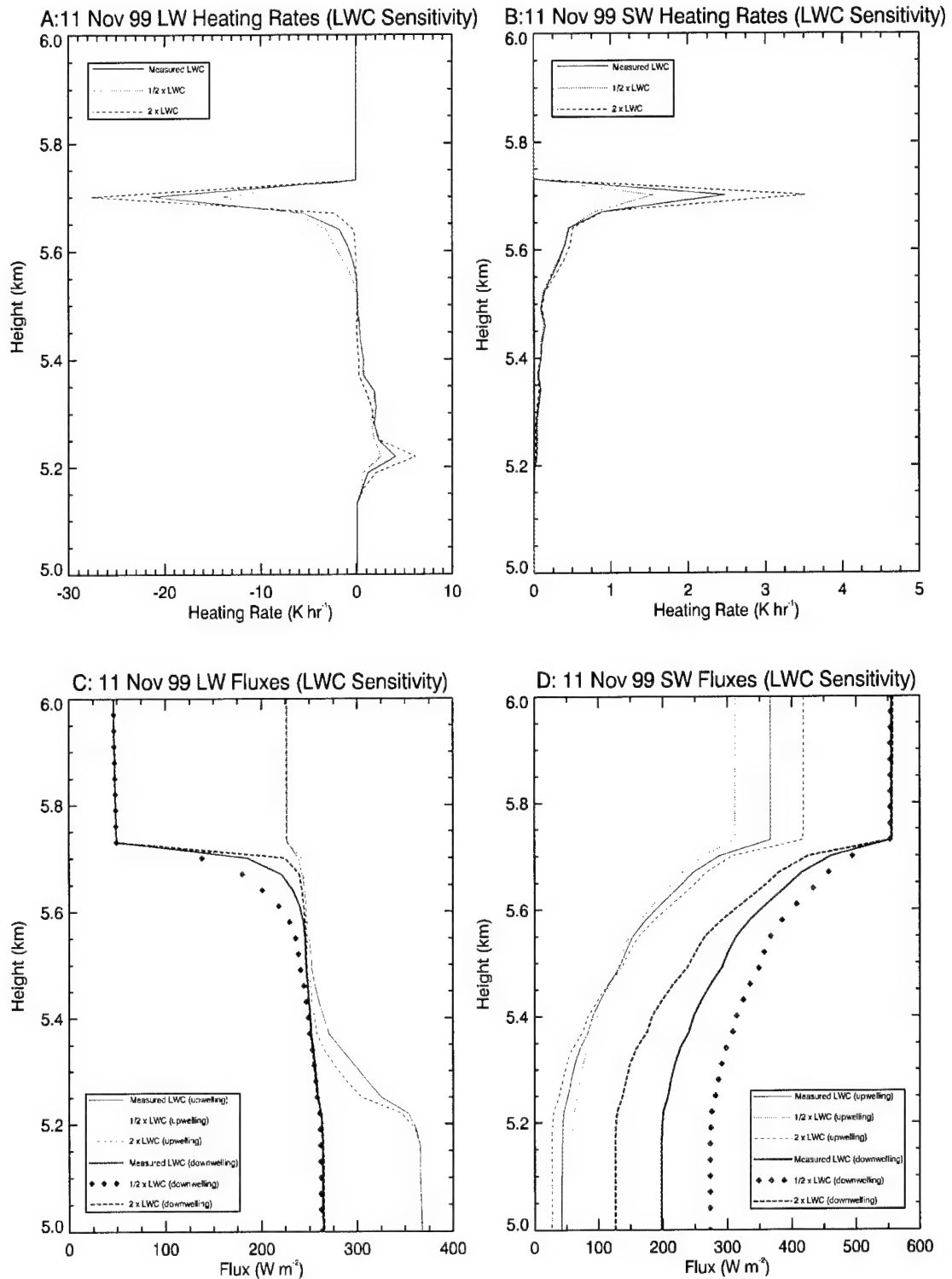


**Figure 9.8 Sensitivity of longwave and shortwave radiative heating rate and flux to the amount of lwc for the 11 Nov 99 case. BUGSRAD model results for doubled and halved lwc are compared to the measured lwc value (see legend). Quantitative values and percent changes for the three plots are shown in Tables 9.1 and 9.2.**

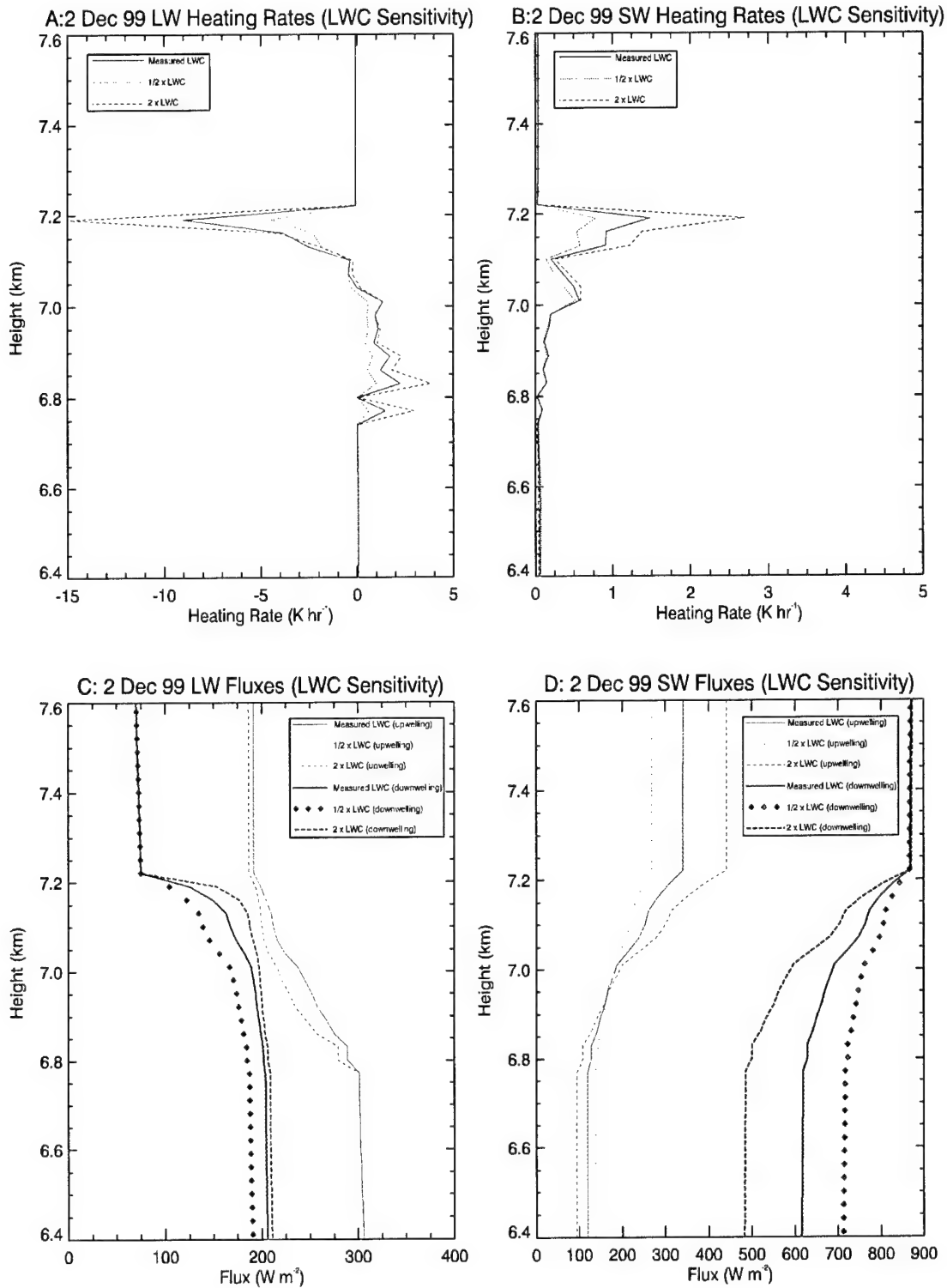


**Figure 9.9** Same as previous figure except for 2 Dec 99 case. Longwave cooling and shortwave heating both occur at or near cloud top, while longwave heating occurs near cloud base. Note the change in scale and refer to Tables 9.1 and 9.2 for the values of radiative heating and cooling when the lwc is doubled and halved.

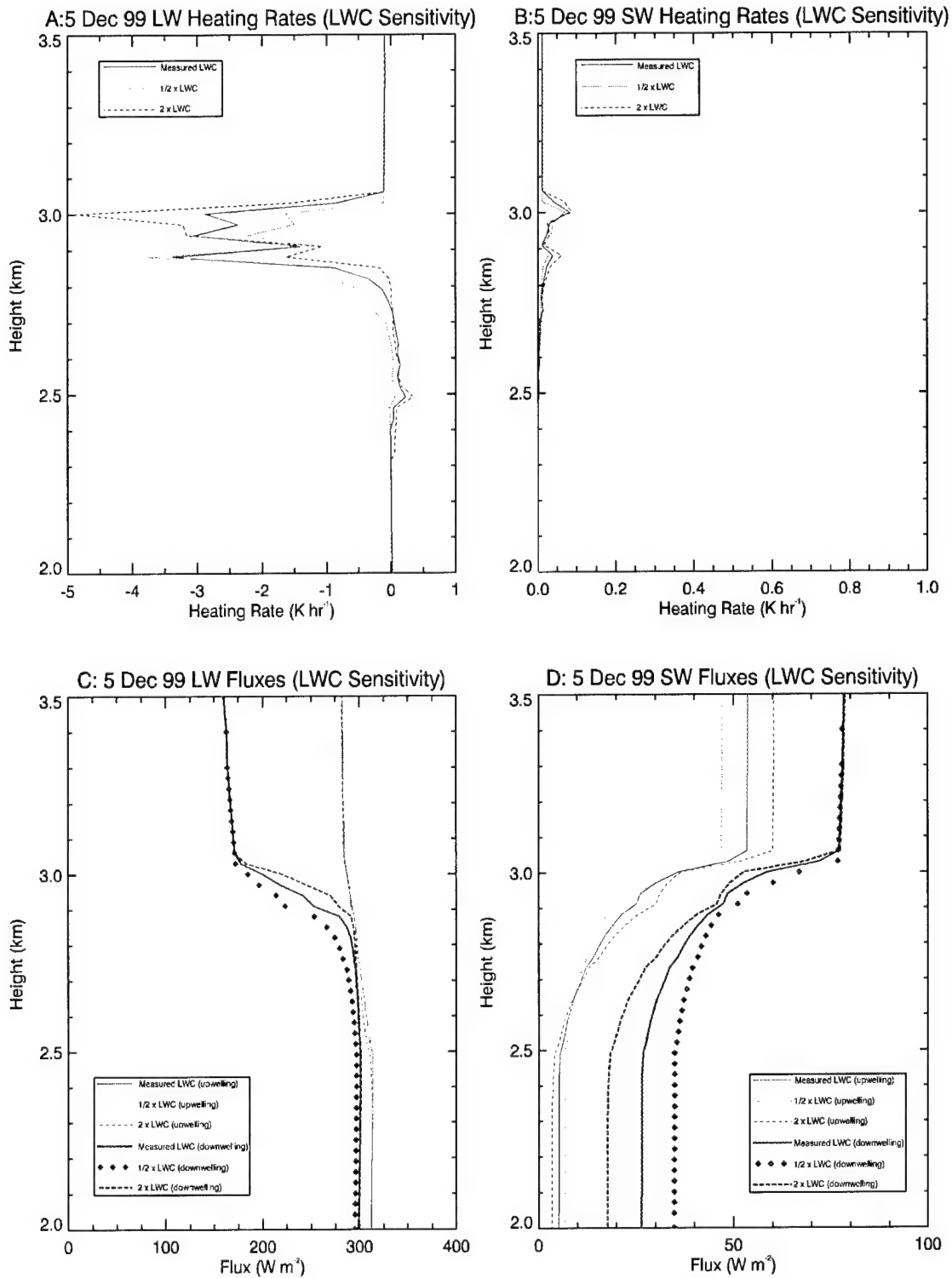


**Figure 9.10** Same as previous two figures except for 5 Dec 99. The variation of longwave cooling near the cloud top is due to the effects of dry air entrainment; the cooling rate associated with maximum lwc is at 2880 m, but decreasing amounts of lwc above that level interact with the fluxes to cause reduced cloud top cooling rates.

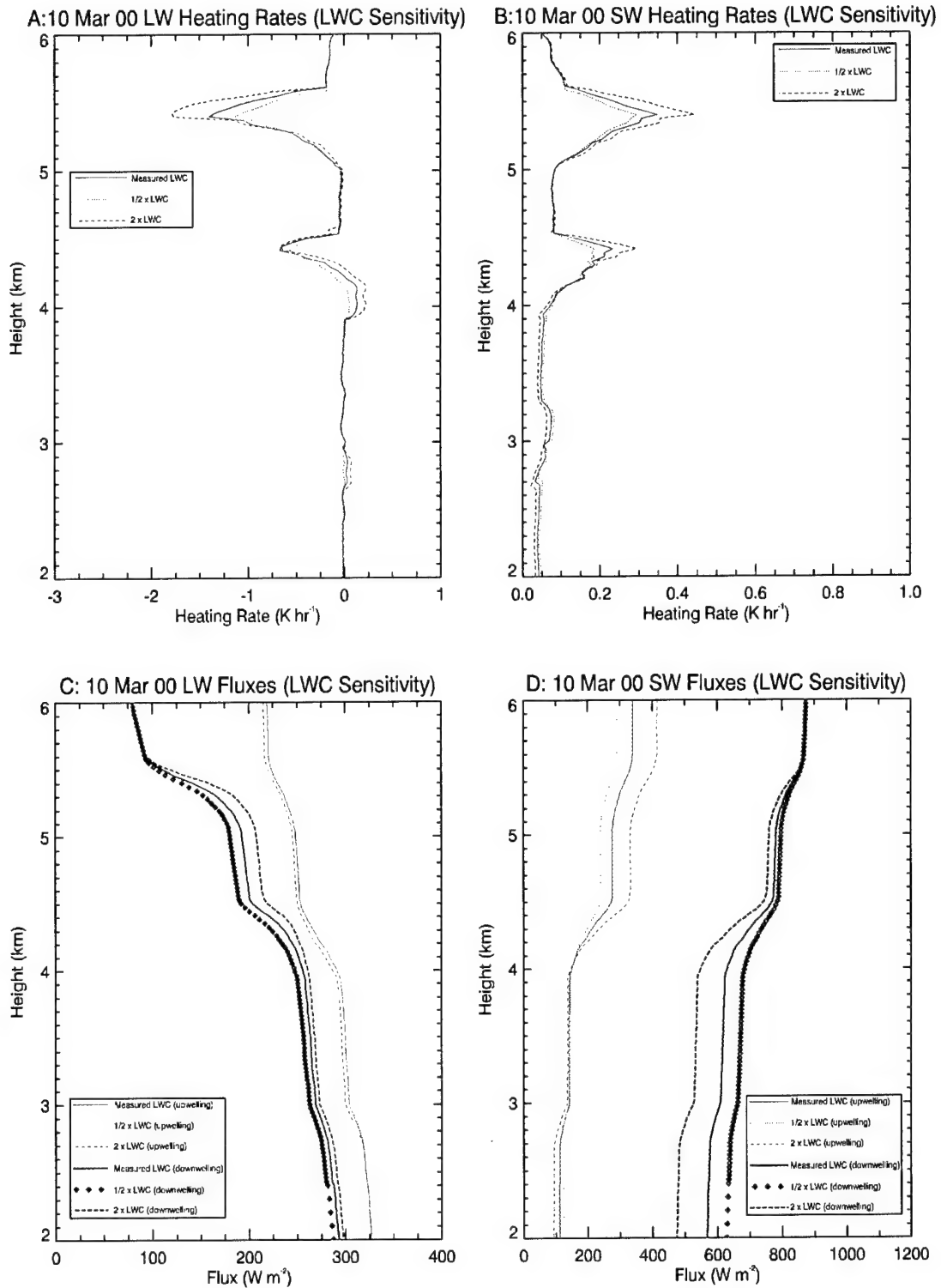


**Figure 9.11** Same as previous three figures except for 10 Mar 00. Small lwc amounts ( $< 0.04 \text{ g m}^{-3}$ ) result in small flux changes and a small net heating rate. Note the change in scale from the other figures. Refer to Tables 9.1 and 9.2 for quantitative values of heating rate and the percent changes from the control case.

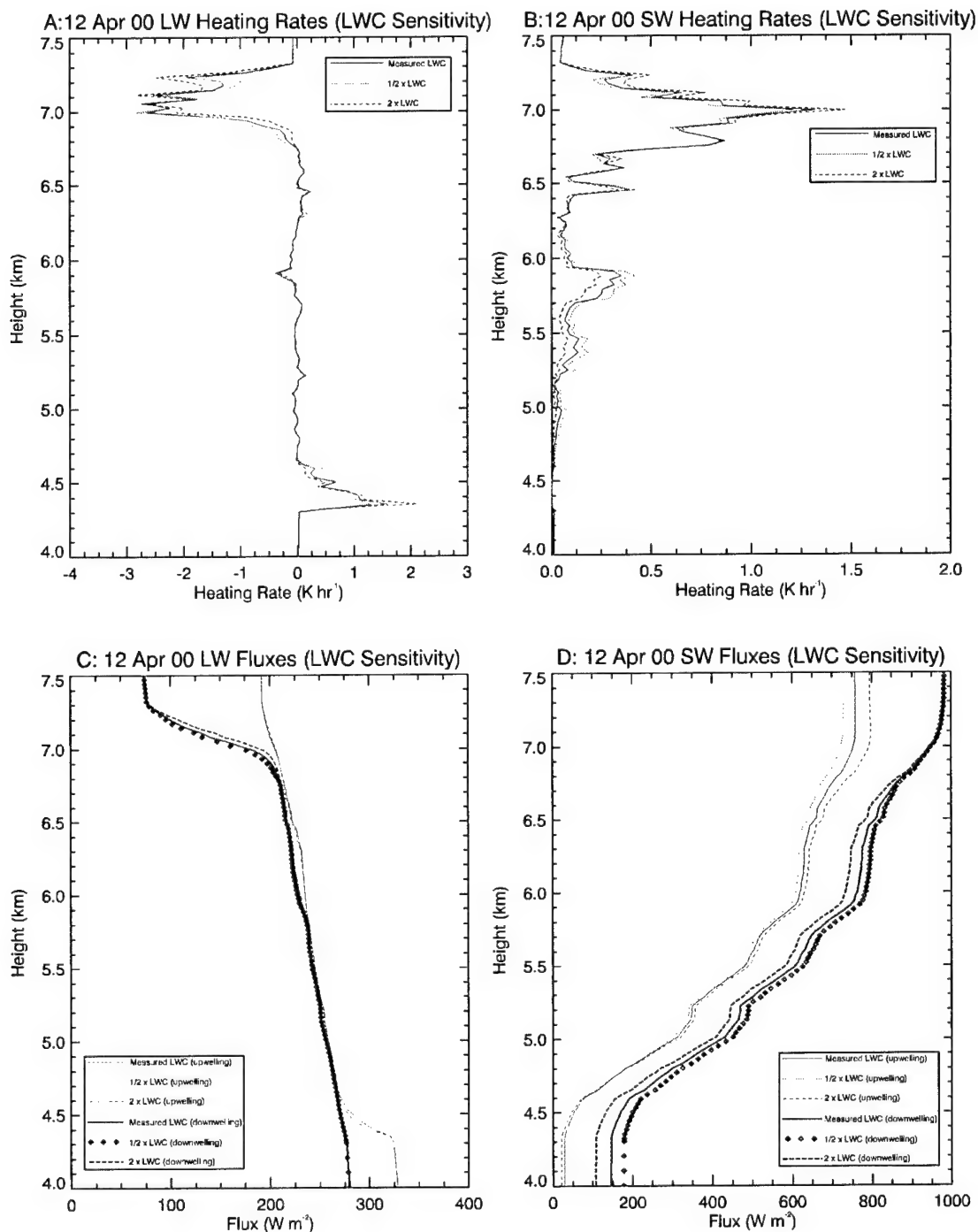


**Figure 9.12** Same as previous four figures except for 12 Apr 00. Note the small changes in fluxes and heating rates when the lwc is doubled and halved; this is due both to decreasing lwc with height at the cloud top, similar to that seen in Fig 9.10 for the 5 Dec 99 case, and to the radiative interactions with adjacent cloud layers.

along with the percent increase or decrease in the cooling rate. There was no clear trend in the data, but the radiative cooling rates increased from about 20 to 40% when the lwc was doubled, and decreased by about 10 to 50% of the control run rates when the lwc was reduced to half of the original amount measured in the cloud. Table 9.2 is similar to Table 9.1, except it lists values and percent changes for the maximum shortwave and longwave heating rates due to doubling and halving the lwc amounts. The increases and decreases in heating rates were similar in magnitude to those found for the longwave cooling cases, although when halving the lwc there were small changes to small values, resulting in some larger changes of up to a maximum of 74% for the 5 Dec 99 case.

At first glance, the shortwave fluxes seemed to be the most sensitive to the changes in liquid water content (e.g., Figure 9.8b). When the lwc is doubled in the 11 Nov 99 case, the downward shortwave flux below the cloud decreases by about  $75 \text{ W m}^{-2}$  more than the control run, while the amount of upward shortwave flux above the cloud increases by  $55 \text{ W m}^{-2}$ . Similarly, when the lwc was cut in half, the downward shortwave flux through the cloud increased by about  $75 \text{ W m}^{-2}$ , while the upward shortwave flux above the cloud decreased by about  $55 \text{ W m}^{-2}$ . The longwave fluxes remain almost unchanged in magnitude above and below the cloud in both cases.

However, it is the convergence or divergence of flux that determines the heating or cooling rates, and not the values at a given point. Therefore, despite the larger changes in the magnitude of the shortwave fluxes, the largest percentage change in the heating and cooling rates was for the longwave radiation, as small flux differences in the interior of the cloud caused greater increases in the convergence and divergence of flux. This is

**Table 9.1 Effect of doubling and halving the measured lwc and iwc on longwave cooling rate. Values involving iwc are in parentheses and the units are enclosed in brackets in the table. Shown are the measured mean lwc (iwc) content for the spiral sounding; the cooling rate based on the measured values (CR-1); the cooling rate based on doubling the lwc (iwc) profile (CR-2); the percent change between CR-1 and CR-2 (PC 1-2); the cooling rate with half the lwc (iwc) of the measured case (CR-3); and the percent change between cooling rates 1 and 3 (PC 1-3).**

Date	Mean lwc (iwc) [g m <sup>-3</sup> ]	CR-1 [K hr <sup>-1</sup> ]	CR-2 [K hr <sup>-1</sup> ]	PC 1-2 [%]	CR-3 [K hr <sup>-1</sup> ]	PC 1-3 [%]
11 Nov 99	0.088 (0.015)	21.3	27.5 (21.3)	23 (0)	13.8 (21.3)	36 (0)
2 Dec 99	0.038 (0.006)	9	14.9 (9.1)	40 (1.0)	4.5 (9.0)	50 (0)
5 Dec 99	0.087	3.4	4.9	31	3.8	11
10 Mar 00 (top layer)	0.005 (0.011)	1.4	1.8 (1.8)	22 (22)	1.1 (1.2)	21 (14)
12 Apr 00 (top layer)	0.048 (0.112)	2.7	2.8 (3.2)	4 (16)	2.8 (3.0)	4 (10)

**Table 9.2 Same as Table 9.1 except for shortwave/longwave heating rate (HR).**

Date	Mean lwc (iwc) [g m <sup>-3</sup> ]	HR-1 [K hr <sup>-1</sup> ]	HR-2 [K hr <sup>-1</sup> ]	PC 1-2 [%]	HR-3 [K hr <sup>-1</sup> ]	PC 1-3 [%]
11 Nov 99	0.088 (0.015)	2.5/4.1	3.5/6.2 (2.5/4.3)	29/34 (0/5)	1.6/2.5 (2.5/3.9)	36/39 (0/5)
2 Dec 99	0.038 (0.006)	1.5/2.2	2.7/3.8 (1.5/2.3)	44/42 (0/4)	0.8/1.0 (1.5/2.2)	47/55 (0/0)
5 Dec 99	0.087	0.08/0.23	0.09/0.34	11/32	0.07/0.06	12/74
10 Mar 00 (top layer)	0.005 (0.011)	0.35/0.14	0.45/0.23 (0.47/0.20)	22/39 (25/30)	0.29/0.06 (0.29/0.08)	17/57 (17/43)
12 Apr 00 (top layer)	0.048 (0.112)	1.3/1.6	1.5/2.1 (1.7/2.2)	13/24 (24/27)	1.2/1.3 (1.0/1.2)	8/19 (23/25)

apparent upon inspection of the fluxes within the cloud layer, as the upward and downward flux lines move closer together when the lwc is doubled and further apart when it is halved.

### 9.3.2 Sensitivity Study 2 – Doubling and Halving the Ice Water Content

A series of BUGSRAD model runs similar to those accomplished in section 9.3.1 were performed for doubled and halved ice water content for each case, as shown in Figures 9.13 through 9.16. The peak values of heating and cooling rate are shown in parentheses in Tables 9.1 and 9.2. Recall that the 5 Dec 99 case did not contain any ice. In the single-layer cases of 11 Nov and 2 Dec 99, changing the iwc did not significantly alter the longwave cooling or shortwave heating profiles. The largest effect was on the 11 Nov 99 longwave heating rate, which changed by only five percent when the iwc was doubled or halved. The amount of iwc had no effect on the shortwave heating rate for either of the single-layer cases. The apparent negligible impact of ice on the single-layer radiative heating profiles makes sense in light of the small amounts of ice compared to liquid water, and the location of that relatively small quantity of ice in the lower parts of those clouds.

However, the results were very different for the two multi-layered cases, which showed cooling and heating rate changes of the same order of magnitude as those for the changes in liquid water content. The reason for this difference is twofold. First, the mean iwc value was over twice as large as the mean measured lwc for both 10 Mar 00 and 12 Apr 00. For the single-layer cases, the iwc was relatively small compared to the

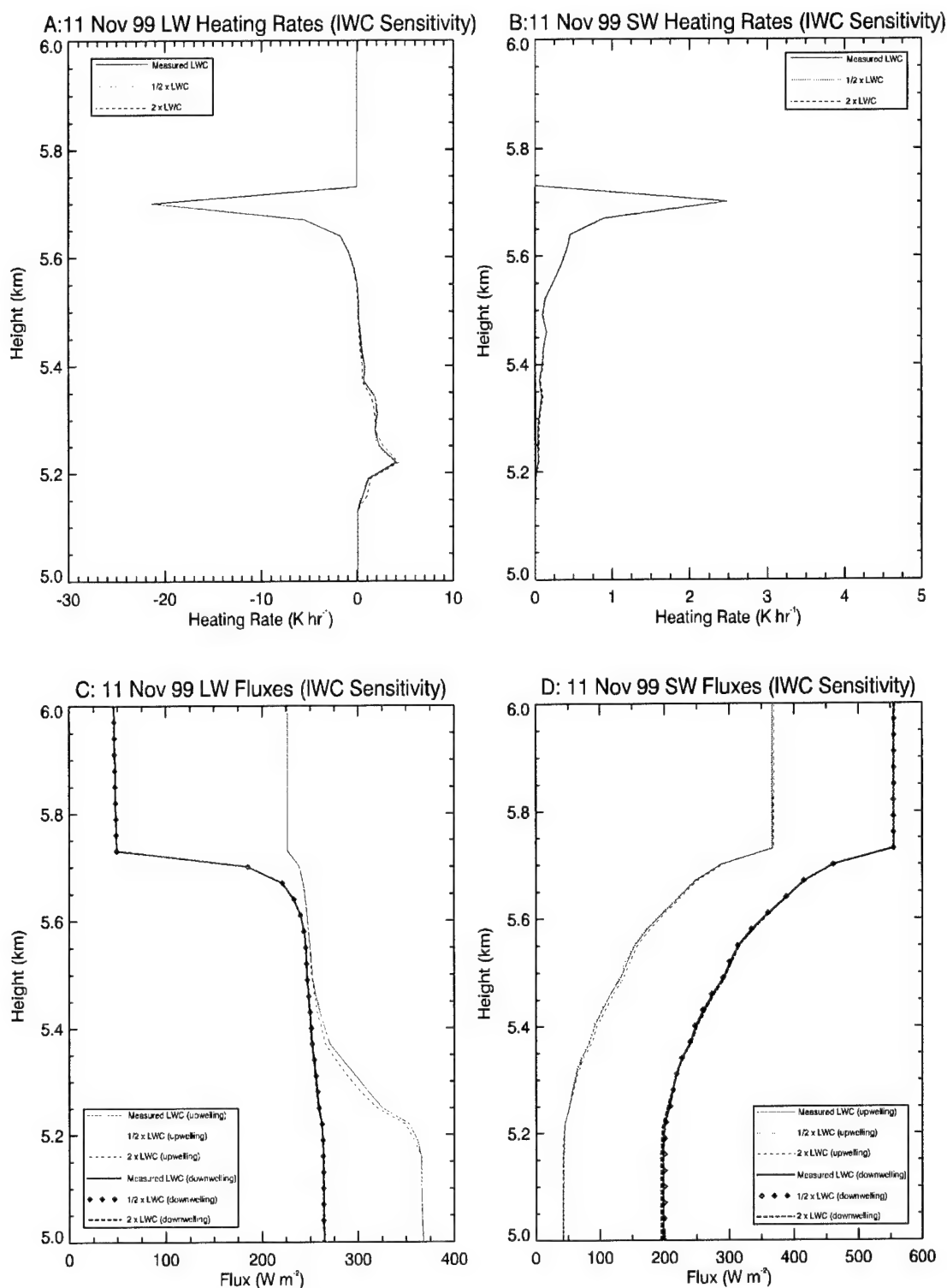


**Figure 9.13** Same as Fig 9.8 except for sensitivity to iwc instead of lwc. The heating and cooling rate values and percent changes are shown in parentheses in Tables 9.1 and 9.2. Note the almost indiscernible changes in flux and heating rate when the iwc is doubled and halved, in contrast to the larger radiative interactions with lwc.

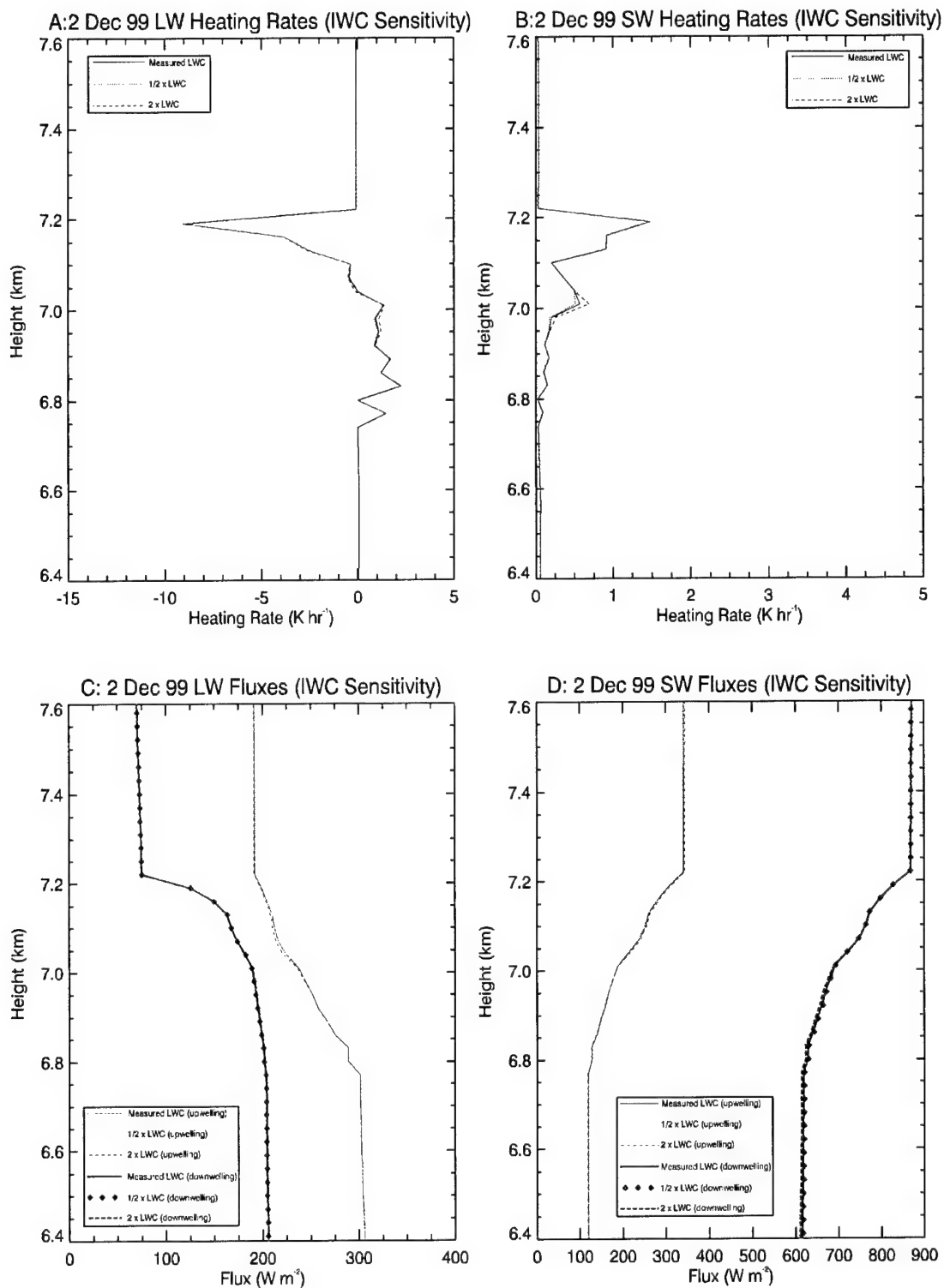


**Figure 9.14** Same as previous figure except for 2 Dec 99 sensitivity to iwc. Again, note that there is very little impact to the fluxes and heating rates when doubling and halving the iwc, due to the relatively small amounts of ice in the bottom parts of the single-layer clouds.

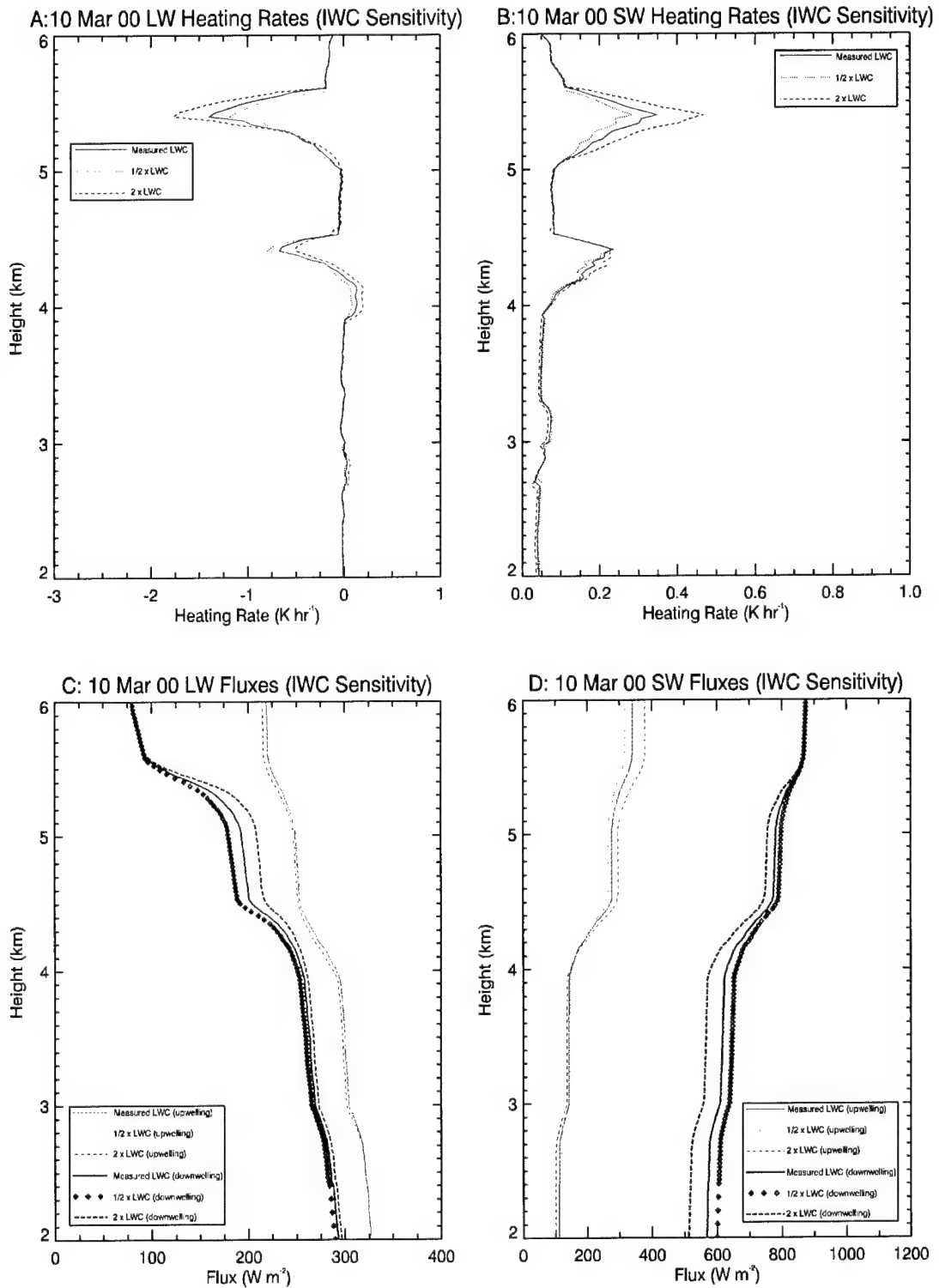


**Figure 9.15** Same as previous figure except for the 10 Mar 00 multi-layered case. The effects of doubling and halving the iwc are much more apparent here than in the previous two cases, because the cloud iwc was uniformly distributed and of the same order of magnitude as the lwc. Values are shown in Tables 9.1 and 9.2.

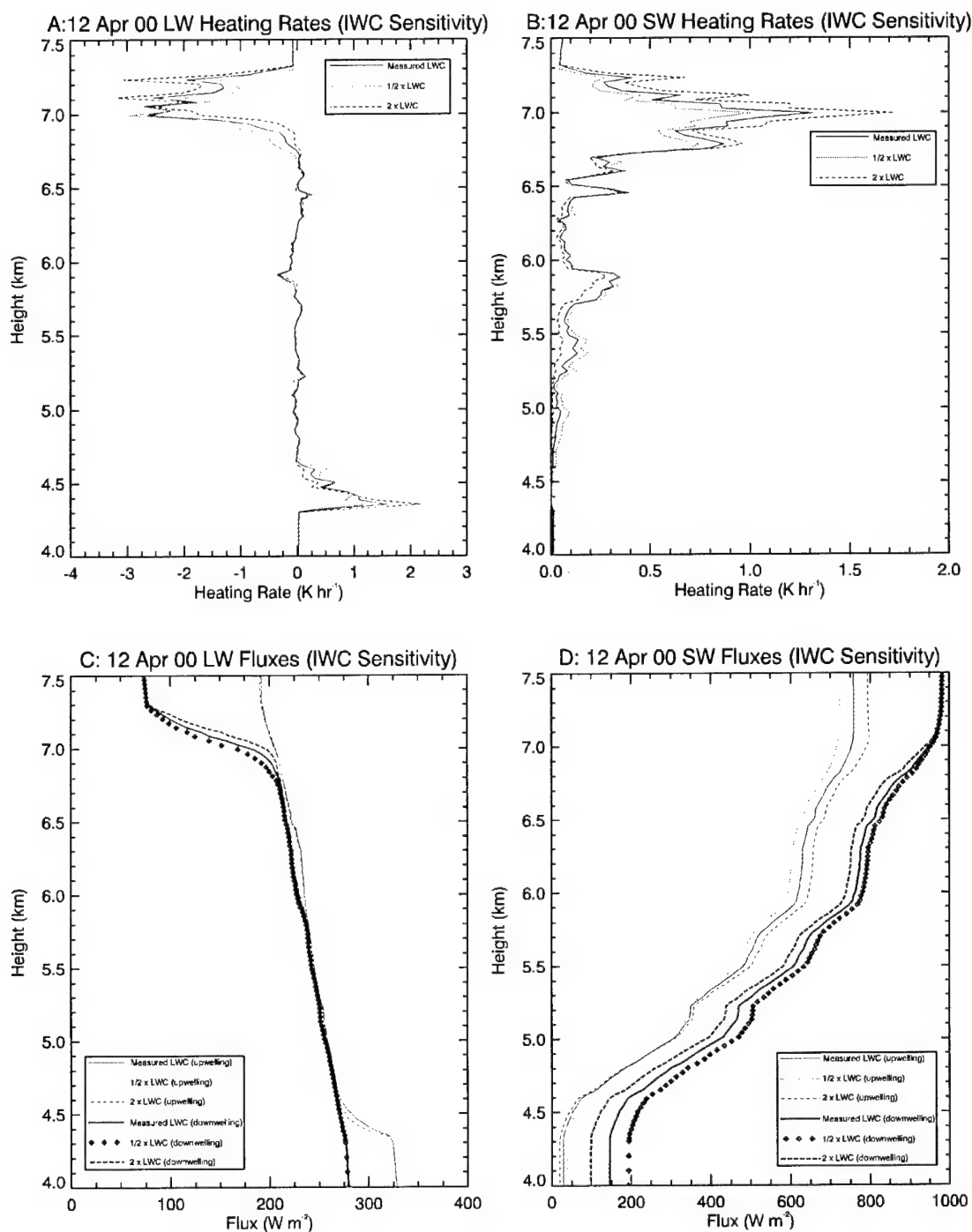


**Figure 9.16** Same as previous figure except for 12 Apr 00. The sensitivity to iwc is also evident in this cloud, as the iwc values were relatively large and the ice particles were more evenly distributed with height than in the single-layer cases. For both multi-layer cases, heating rates changed 25-30% when iwc was doubled or halved.

lwc. Second, the iwc was evenly distributed through all three layers in both multi-layered cases, whereas the iwc increased towards the bottom of the single-layer clouds.

There were also some differences between the multi-layered systems. In contrast to the 10 Mar 00 system, the 12 Apr 00 cloud layers contained much higher values of ice water content. The mean iwc of all three layers of the 10 Mar 00 cloud (in contrast to the top layer value shown in Tables 9.1 and 9.2) was about  $.02 \text{ g m}^{-3}$ , compared to a mean iwc of  $0.22 \text{ g m}^{-3}$  for the 12 Apr 00 cloud. Despite this contrast, the overall longwave cooling rates at cloud top for the 12 Apr 00 case are not substantially higher than the 10 Mar 00 case, due to the previously discussed damping effect of smaller lwc amounts above the maximum quantity. The integrated radiative effects are undoubtedly larger, due to the thicker clouds and the larger amounts of liquid and ice in the lower parts of the 12 Apr 00 cloud, but the cloud top cooling rates are very similar. On the other hand, the shortwave heating rates are an order of magnitude larger than for 10 Mar 00. This is due to the large amounts of ice, as evidenced by the minimal impacts to shortwave heating near cloud top when the lwc amounts are doubled and halved, and especially by noting the changes in shortwave heating when the ice water content is set to zero.

These factors point to the importance of knowing the liquid to ice ratio in a cloud, as well as the distribution of these two quantities through a cloud system. Since differential heating due to radiative processes seems to be a primary driving mechanism for cloud circulations, and the amounts of these quantities obviously affect the amount of heating and cooling in the cloud, it is important to know the microphysics accurately in order to understand the cloud dynamics. This has implications for forecasting mid-level clouds, as the strength of the circulations probably translates into the length of time a

system is able to maintain itself against dissipation (e.g., Harrington et al., 1999). In terms of the effects of microphysics on radiative processes, incorrect parameterizations of cloud phase could lead to significant errors in climate or general circulation models. The consequence of using the wrong cloud phase in a model parameterization is highlighted in the next sensitivity study.

### 9.3.3 Sensitivity Study 3 – Effects of Incorrect Cloud Phase Parameterizations

In Chapter 1, we argued that a better understanding of the structure of mixed-phase, mid-level clouds would lead to forecast improvements. During that discussion, the prognostic scheme of Tiedtke (1993) was used as an example of current methods that distinguish between cloud liquid water and ice solely on the basis of temperature. We have already shown that *iwc* is not correlated with temperature, yet for lack of a better method, several models (e.g., ECMWF and CSU GCM) use a temperature of  $-20^{\circ}\text{C}$  as the absolute threshold for delineating ice from liquid; everything colder than this temperature is assumed to be ice. For the first part of this sensitivity study, the 2 Dec 99 cloud is used to demonstrate the effects of using this particular temperature threshold to delineate liquid from ice. In the second sensitivity study, the 11 Nov 99 cloud field is inverted in the vertical to further demonstrate the errors associated with parameterizing mid-level cloud phase using temperature.

#### 9.3.3.1 The Use of a $-20^{\circ}\text{C}$ Threshold to Delineate Cloud Liquid from Ice

The single-layer cloud observed on 2 Dec 99 was situated in temperatures between  $-27$  and  $-30^{\circ}\text{C}$ , yet it was composed primarily of supercooled liquid droplets, as

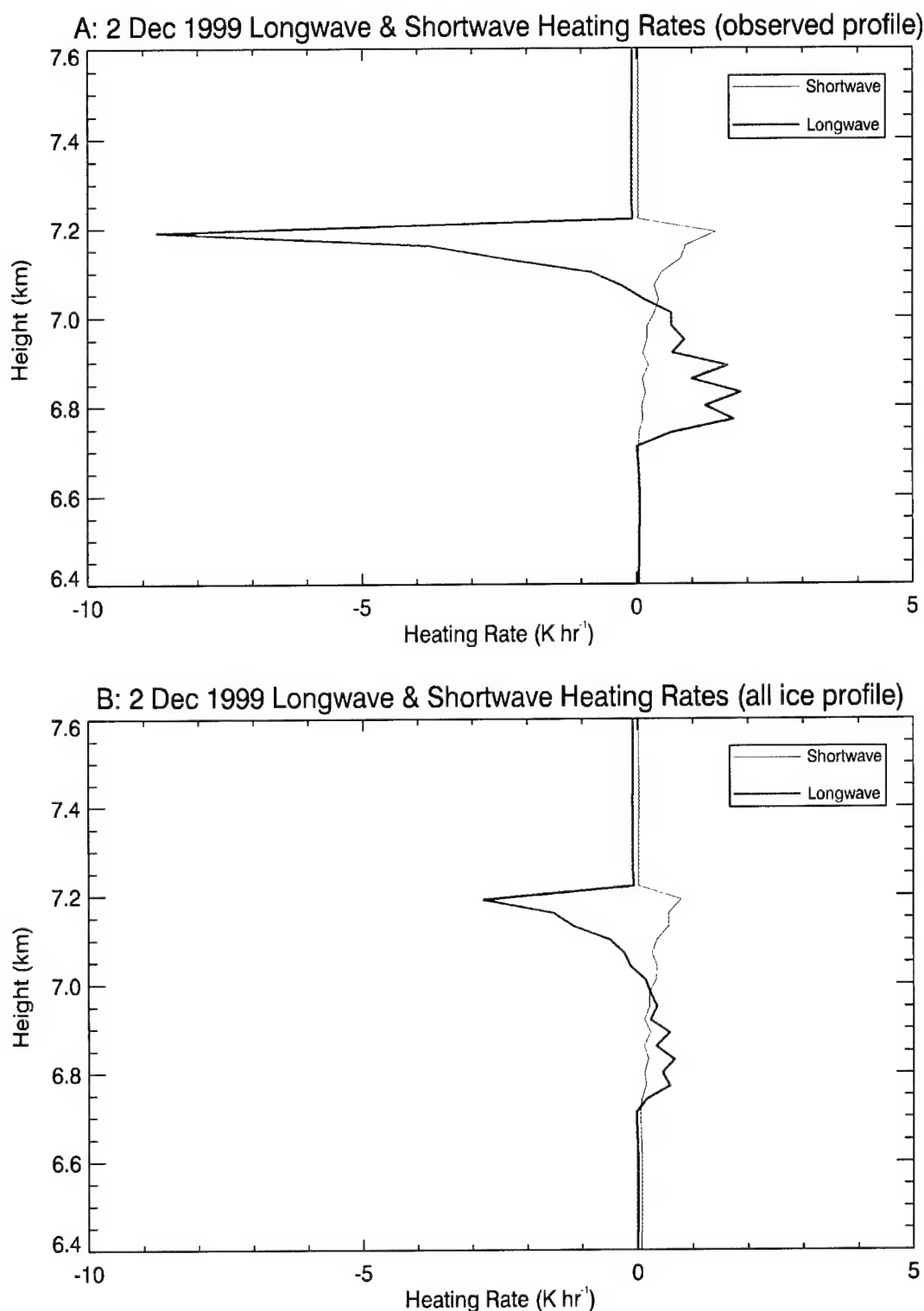


**Figure 9.17 Sensitivity of heating rate profiles to model parameterization of cloud phase. (A) shows the heating rate profile using the measured lwc and iwc values; (B) shows the same profile when the cloud is converted completely to ice, as it would be in current models that determine water phase by temperature.**

shown in Chapter 5. In models that use temperature as a phase discriminator, this cloud would be well within the region characterized as entirely ice. Figure 9.17 shows a comparison of two radiative heating rate profiles for the 2 Dec 99 cloud. The top profile uses the observed microphysics; but in the bottom profile, the cloud liquid water is completely converted to ice water content, as it would be in a model using temperature to parameterize cloud phase. The longwave cooling and heating rates in the all ice case are 2.8 and 0.67 K hr<sup>-1</sup>, respectively, or about one third of the value found when using the actual lwc and iwc. The shortwave heating rate of 0.79 K hr<sup>-1</sup> is just over half of the value found when using the observed microphysics.

#### 9.3.3.2 Inverting the Moisture Structure in the 11 Nov 99 Cloud

To further demonstrate the errors associated with using temperature to parameterize water phase, the lwc and iwc fields were inverted in the 11 Nov 99 cloud so that the ice would be in the coldest part of the cloud. The resulting radiative heating and flux profiles from the BUGSRAD model are compared with the observed profiles in Figure 9.18. Note that the resulting fluxes above and below the cloud at 5 and 6 km are identical in both profiles, but the manner and location in which the radiation interacts with the cloud are quite different.

These differences in flux convergence and divergence change the shape of the net heating profile. Comparing the observed to the inverted case, the cloud top longwave cooling decreases from 21.3 to 8.2 K hr<sup>-1</sup> and the longwave heating at cloud base increases from 4.1 to 10.6 K hr<sup>-1</sup>. The decrease in cloud top cooling and increase in cloud base heating are due to the change in location of the maximum lwc, as it interacts more

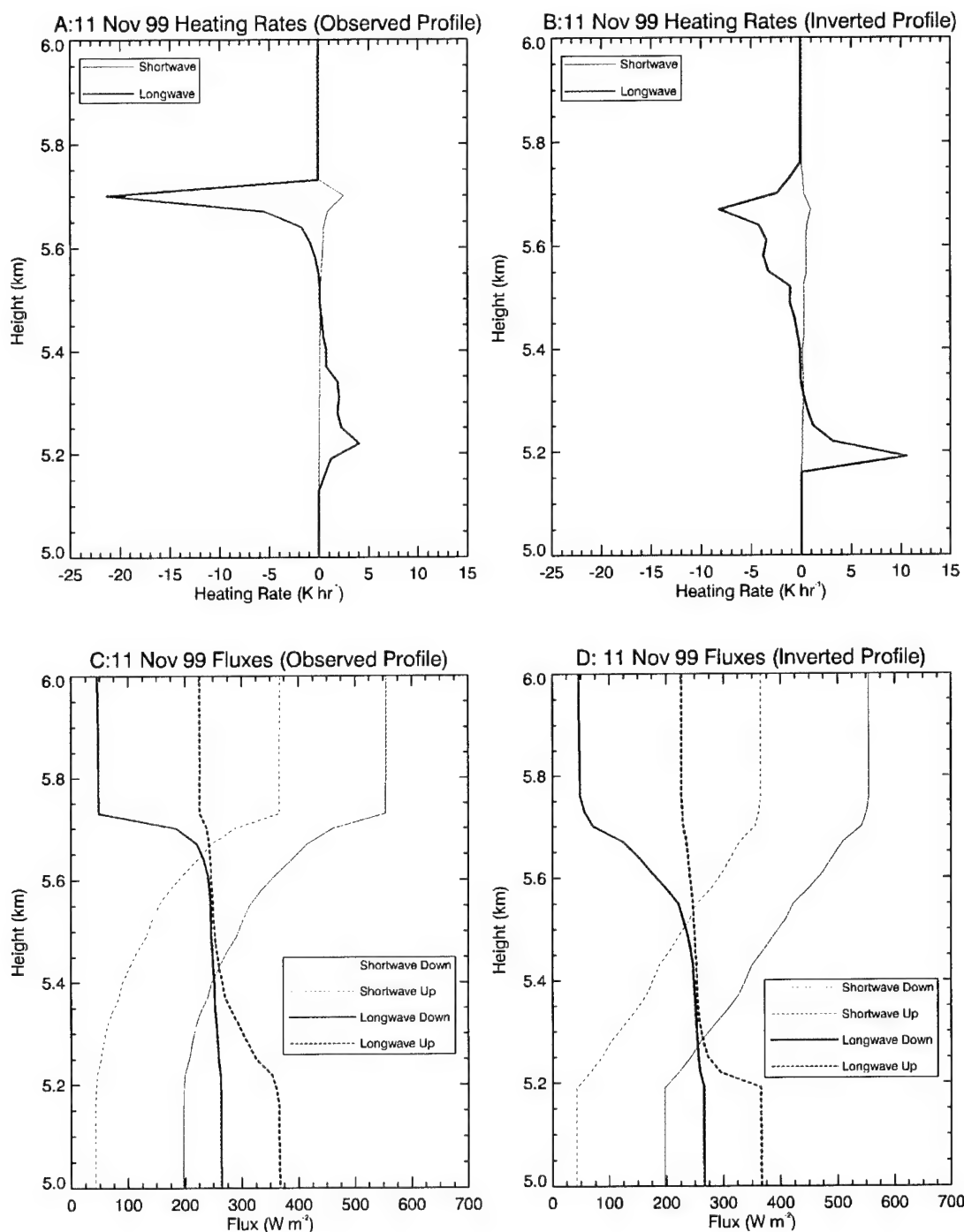


**Figure 9.18 Sensitivity of heating rate profiles to model parameterization of cloud phase. (A) and (C) show the observed heating and flux profiles using measured lwc and iwc values for 11 Nov 99; (B) and (D) show the same profile when the cloud lwc and iwc profiles are inverted in the vertical. This is another possible effect of using temperature to determine water phase, as iwc would increase toward cloud top.**

strongly with the longwave radiation than the ice. The shortwave heating profile is less affected by inverting the cloud moisture field, but the maximum does decrease from 2.5 to 1.0 K hr<sup>-1</sup> between the observed and the inverted case. Finally, the net vertical differential heating decreases from 23 to about 18 K hr<sup>-1</sup>, which has some implications for radiatively driven cloud circulations in models, as discussed below.

#### 9.3.3.3 Implications of Inaccurate Phase Parameterizations for Modeling

The results of these sensitivity studies have important implications for forecast, climate, and general circulation models. The microphysics determines the radiative processes, which in turn affects the dynamics of the cloud circulations. For the 2 Dec 99 cloud, the net vertical differential radiative cooling rate using the actual data is about 5.5 K hr<sup>-1</sup>, whereas the model with all ice gives a rate of about 1.4 K hr<sup>-1</sup>. This means the net radiatively-induced circulation forcing of the mixed-phase cloud is approximately four times stronger than that of the strictly ice cloud. Likewise, inverting the moisture structure of the 11 Nov 99 case so that ice increases towards cloud top also changed the net circulation forcing by about 5 K hr<sup>-1</sup>. If the wrong phase is used, inconsistencies in the radiative forcing may adversely affect the conclusions drawn from forecast and climate models, particularly for large-scale studies in which the integrated effects of many mid-level clouds may combine to give a substantial overall error.

#### 9.3.4 Sensitivity Study 4 – Sun Angle Variations

As an illustrative example of the sensitivity of shortwave heating rates to variations in solar zenith angle, we chose to plot the two quantities against cloud depth

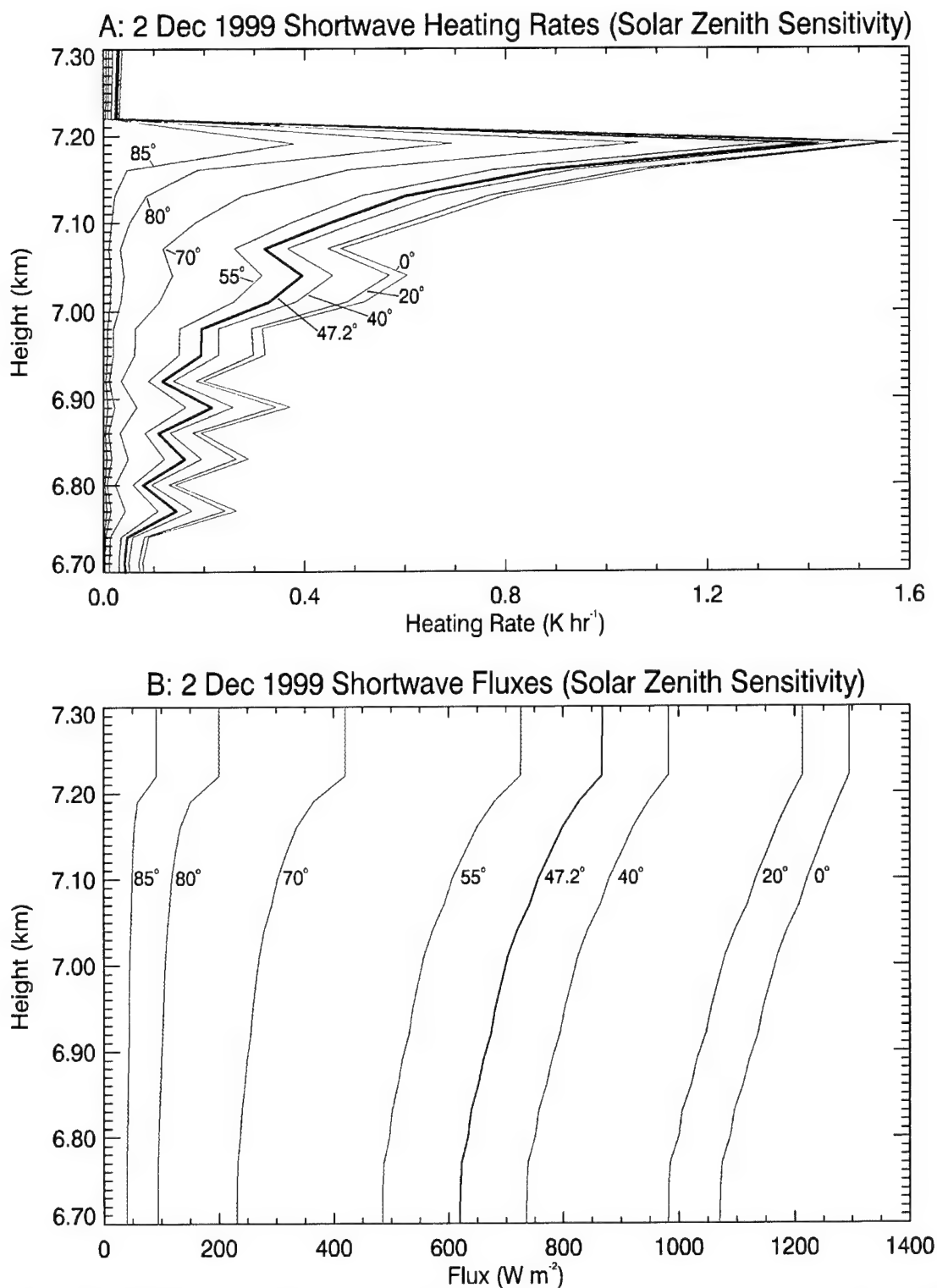


**Figure 9.19 Sensitivity of shortwave heating rate to solar zenith angle for 2 Dec 99. The black curve marks the observed heating rate and flux at the observation time; the other curves represent zenith angles as annotated in the diagram. Small angle changes after sunrise may offset nocturnal radiative cooling and cause dissipation.**

for the 2 Dec 99 case. The results are shown in Figure 9.19, and include the downward shortwave fluxes through the layer. The relatively rapid increase in shortwave heating rate at cloud top for small decreases in solar zenith angle may be indicative of the effect of sunrise and sunset on cloud radiative and dynamic processes. Just before sunrise, the shortwave heating rate is, of course, zero; when the solar zenith angle reaches  $80^\circ$ , the heating rate exceeds  $0.5 \text{ K hr}^{-1}$ . With small increases in solar zenith angle, the heating rate continues to quickly rise to greater than  $1 \text{ K hr}^{-1}$  at  $70^\circ$ . At the actual aircraft measurement time, a shortwave heating rate of near  $1.5 \text{ K hr}^{-1}$  is evident with a zenith angle of  $47.2^\circ$ , and the gains in heating rate are very small for increasingly larger zenith angles.

If we generalize this result, assuming all other factors are constant, we find that the shortwave heating rate makes the greatest strides to offset the longwave-cooling rate relatively quickly after sunrise. From the cloud processes discussion in Chapter 7, recall that differential vertical radiative heating is one of the main drivers for internal circulations. If a mid-level cloud is being maintained in a stable balance overnight, this added amount of shortwave heating at cloud top may be enough to weaken the vertical motions to the point at which the condensate supply rate is no longer large enough to sustain the cloud, causing dissipation. Although we did not gather the data necessary to prove it conclusively, forecasters viewing satellite imagery during the field experiment often saw clouds quickly erode after sunrise. We speculate that this mechanism may be a fairly common way for relatively thin clouds to dissipate, such as those formed by convective detrainment, but probably does not affect the thicker clouds formed by larger synoptic or mesoscale lifting mechanisms.

By a similar argument, the solar angles again become large late in the day, and the shortwave heating at cloud top rapidly drops off in the waning hours of the day to zero at sunset. The increased net radiative cooling at the top of a moist layer, or even a thin mid-level cloud, may then become large enough to destabilize the layer and increase the internal circulations, resulting in new layer formation or thickening mid-level clouds overnight. The altocumulus modeling work of Liu (1998) supports this idea, as he found cloud depth and liquid water path decreased with solar heating on mid-level cloud layers during the morning hours, and increased again after sunset.

The net result of these two processes, increased net cooling towards sunset and increased net heating beginning at sunrise, is a diurnal fluctuation of mid-level clouds. Evidence for these processes can be seen in Figure 9.20, in which percent frequency of occurrence of mid-level cloud over North Dakota is plotted versus time for the months of September through November. The cloud information is derived from ten years of three-hourly infrared data taken from the International Satellite Cloud Climatology Program (ISCCP) D2 database. The lower panel shows the satellite-derived surface temperatures for the same times. A clear diurnal cycle is especially prominent in October, with frequency of occurrence of mid-level clouds peaking at greater than 40% just before sunrise, and then sharply dropping to around 20% after just three hours. After 1800 UTC the frequency stabilizes at 17%, and then clouds begin increasing after sunset, as net radiative cooling processes begin to dominate the cloud dynamics. The other months show a similar trend but are not as pronounced as October.

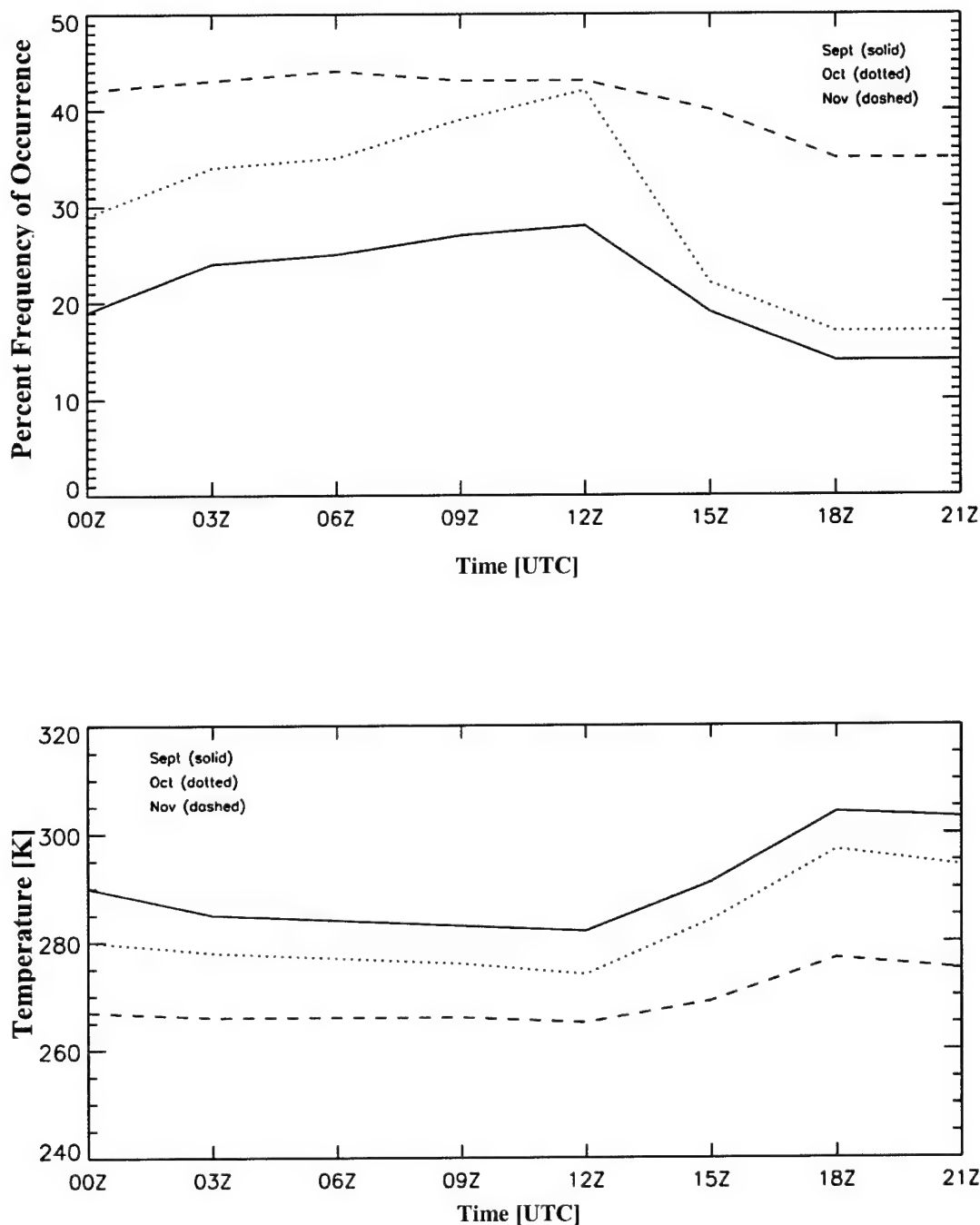


**Figure 9.20 Diurnal variation of mid-level clouds over North Dakota.** The top panel shows percent frequency of occurrence of mid-level clouds versus time of day for September, October and November. The plots are derived from a three-hourly infrared ISCCP database over a ten-year period of record. The bottom panel shows the satellite-derived surface temperature over the same time period. Clouds increase overnight in response to radiative cooling but decrease after sunset, as net radiational cooling decreases in response to shortwave heating at cloud top.

The diurnal pattern of mid-level cloudiness is further reinforced by a climatological study of clouds over the Southern Great Plains Atmospheric Radiation and Measurements (ARM) program, Cloud and Radiation Testbed (CART) site by Lazarus et al. (2000). They found that the diurnal signal of altocumulus clouds was strongest in the summer, when the solar elevation angles are the greatest, strengthening our argument concerning the affect of solar elevation angle on the net radiative heating at cloud top. During the winter months, there is almost no diurnal cycle of mid-level cloudiness, and the percent frequency of occurrence of only six to eight percent is the lowest of any time of year.

#### 9.3.5 Sensitivity Study 5 – Cloud Height Variations

In section 9.3.1, we demonstrated that increases and decreases in cloud lwc at a given height affect the amount of radiational heating and cooling. The current sensitivity study examines the effects on radiational processes of changing only the “height” of the 2 Dec 99 cloud. Since this cloud had the highest top of all those in the CLEX study (7220 m), it represents the upper limit of what would generally be considered a mid-level cloud. With the background atmospheric profile held constant, the actual cloud microphysical values were simply inserted into three increasingly lower levels of the atmosphere, in one-kilometer increments. Specifically, the observed lwc was used to calculate a new mixing ratio at successively lower altitudes to account for density differences from one level to another.

The resulting fluxes and heating rates for this set of BUGSRAD runs are shown in Figures 9.21 and 9.22 for the original cloud at 7220 m, and the simulated cloud top

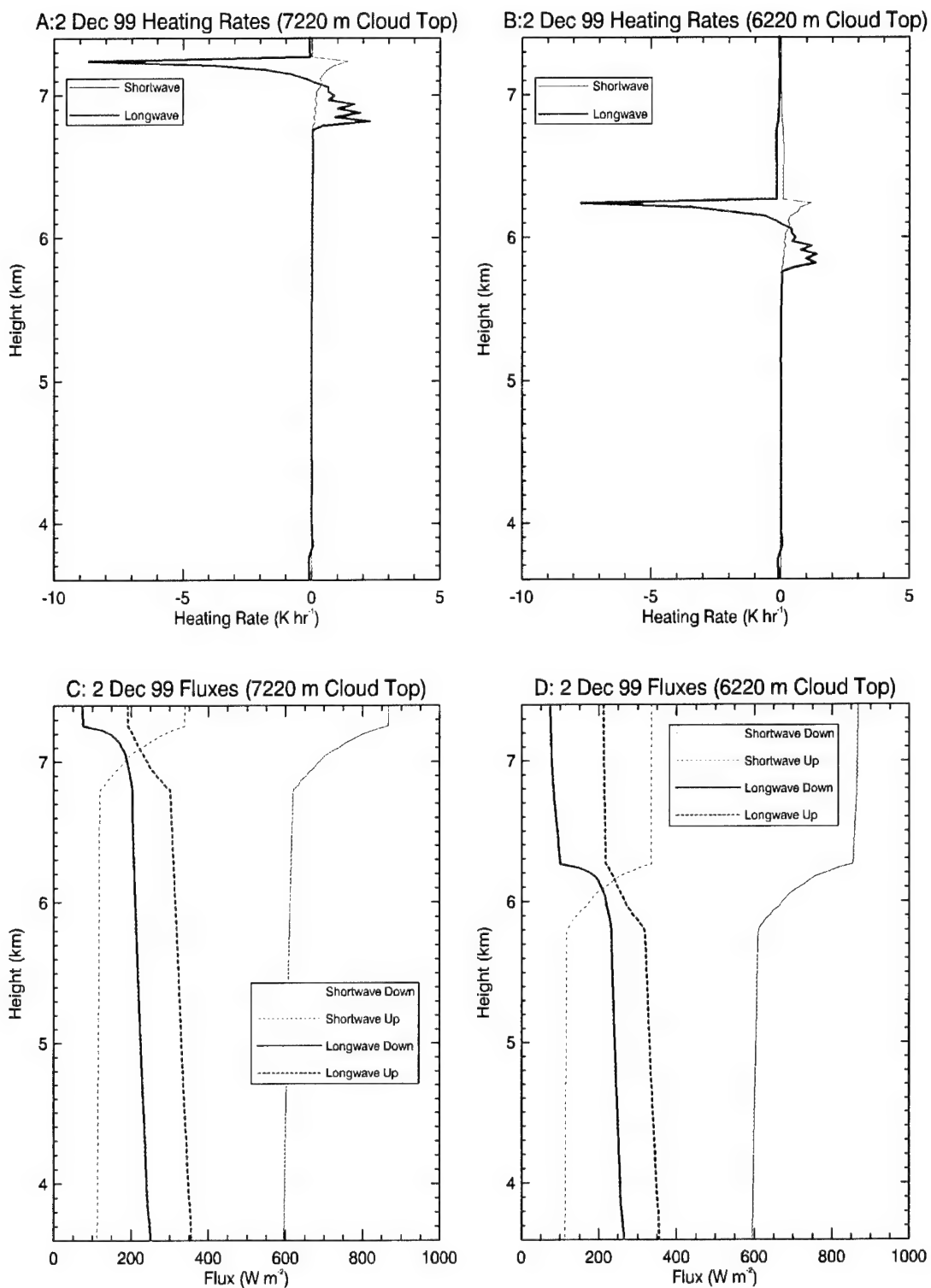


**Figure 9.21** Sensitivity of radiative heating rates (A, B) and fluxes (C, D) to changes or errors in cloud height. Plots A and C show the heating rates and fluxes at the actual measurement height, while B and D use the same cloud profile, but at 1 km lower height. The resulting heating rates are about  $1 \text{ K hr}^{-1}$  for the lower cloud.

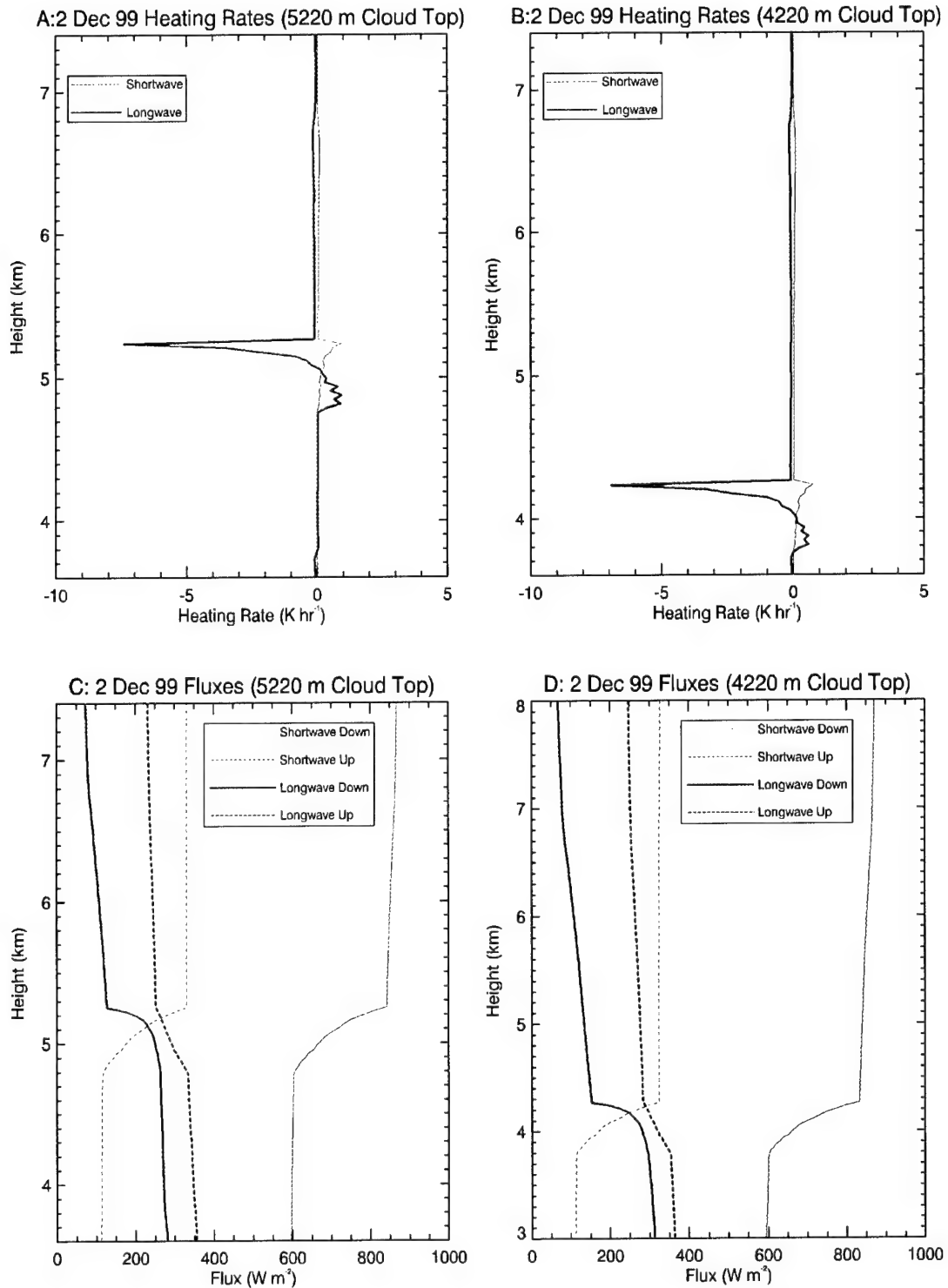


**Figure 9.22** Same as Fig 9.21 except at lower heights of 5.2 km (A,C) and 4.2 km (B,D). Note that smaller height differences between cloud base and the Earth's surface result in less heating at cloud base and cooling at cloud top, as forwarded by Stephens (1978). For this reason, cloud height accuracy is important for GCMs.

heights of 6220, 5220, and 4220 m. The maximum longwave radiative cooling steadily decreased from  $9.0 \text{ K hr}^{-1}$  to 7.7, 7.4 and  $6.9 \text{ K hr}^{-1}$  as the cloud was moved to lower altitudes. The shortwave heating and cooling showed a similar decrease in magnitude with lower cloud heights. Because flux is related to the temperature of a body by the Stefan-Boltzman law, this result is not very surprising, but it does have implications for general circulation models. The penalty for a one-kilometer error in model cloud height in this case was a longwave cloud top cooling and cloud base warming error of about  $1 \text{ K hr}^{-1}$  for each value. Depending on the horizontal and temporal extent of the cloud, height errors could result in substantial variations or errors in global radiative cooling values. Perhaps more importantly for climate considerations, the outgoing longwave radiation increases as the cloud heights are moved to lower heights, giving an overall cooling effect when viewed from space.

#### 9.3.6 Sensitivity Study 6 – Effects of Cloud Layering

The 10 Mar 00 and 12 Apr 00 control cases are used as the baselines for this sensitivity study, with various combinations of the three cloud layers removed from the input profile in order to assess the impact of layering on the net radiative heating of the system. In each case, the radiosonde sounding data was used to replace the omitted cloud layer(s), and BUGSRAD was run to see how the fluxes and heating rates responded to the remaining cloud layer(s). The results are shown in Figures 9.23 through 9.25 for the 10 Mar 00 case, and Figures 9.26 thorough 9.28 for 12 Apr 00, with the binary three-digit code corresponding to the top, middle and bottom layer, respectively. For example, “101” means the middle layer is excluded, and only the top and lowest layer are included

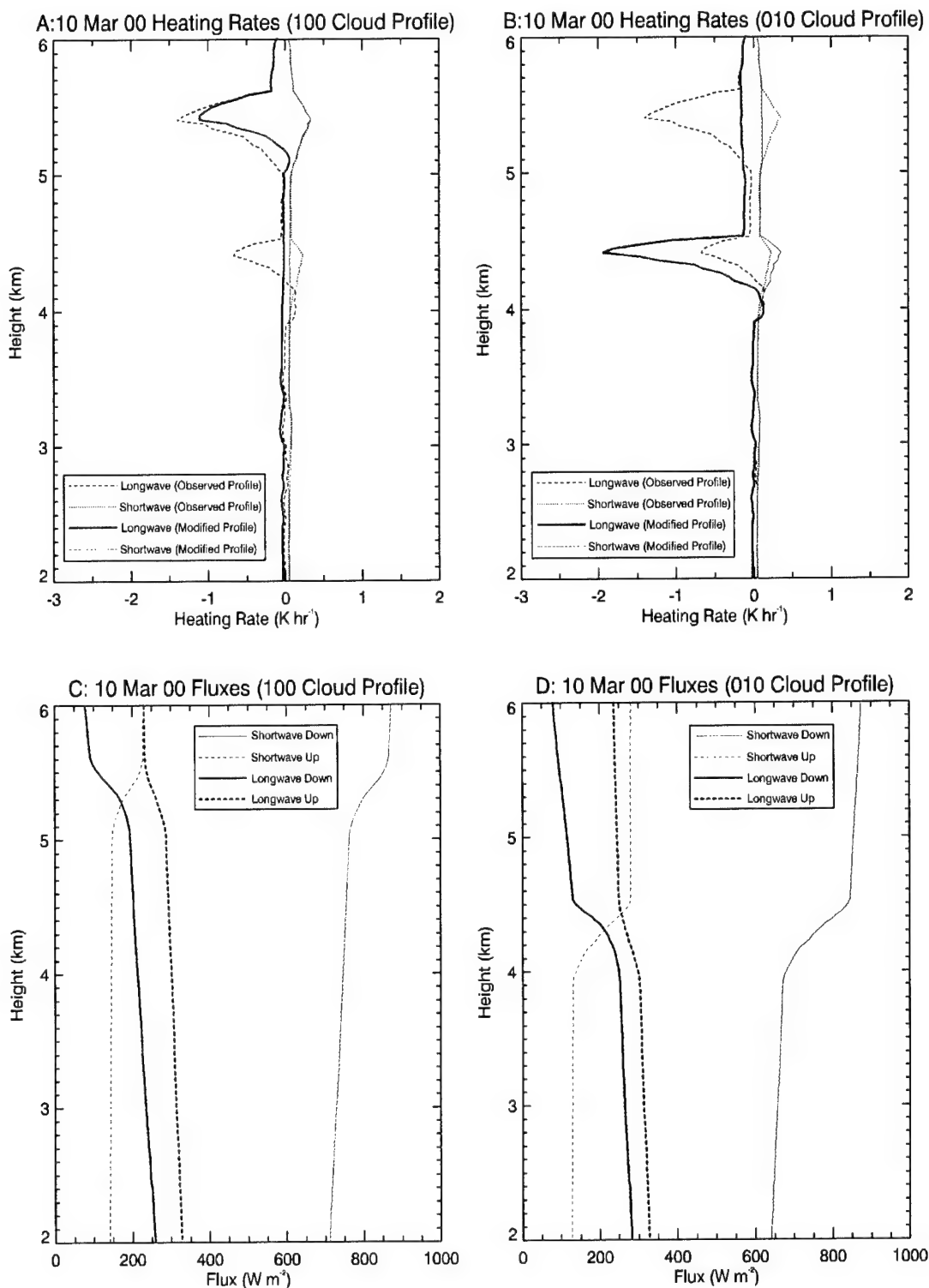


**Figure 9.23 Sensitivity of radiative heating rates and fluxes to changes in cloud layering.** The three-digit binary code corresponds to the layers included in each plot, i.e., only the top layer is included in “100”. The 10 Mar 00 control case (all three layers) is shown in Figure 9.5 and is represented by a dashed line in each plot.

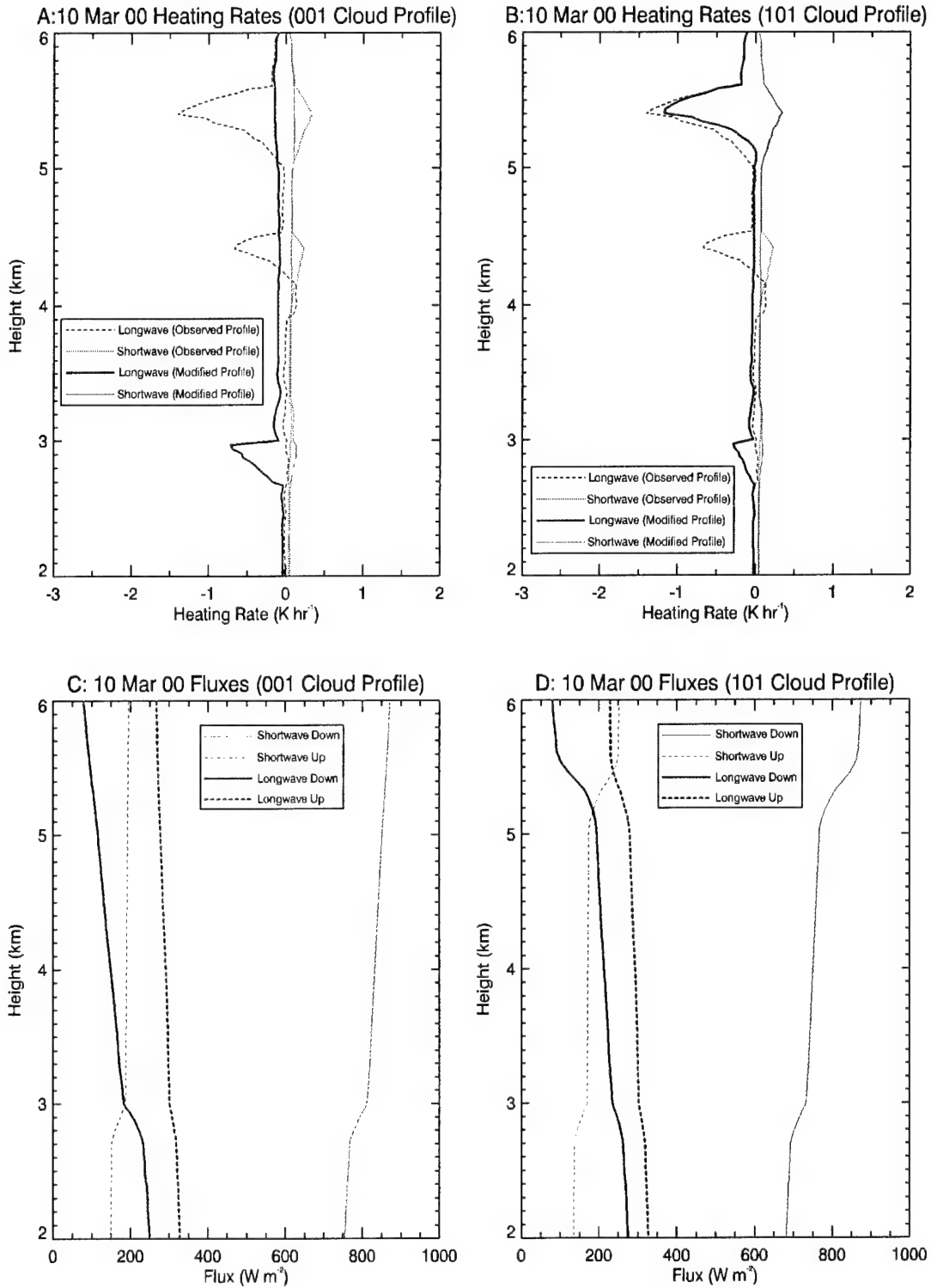


**Figure 9.24** Same as Fig 9.23 except for cases in which only the bottom layer is included (001) and only the top and bottom layers are included (101). Note the longwave cooling in the bottom layer in the absence of intervening layers aloft.

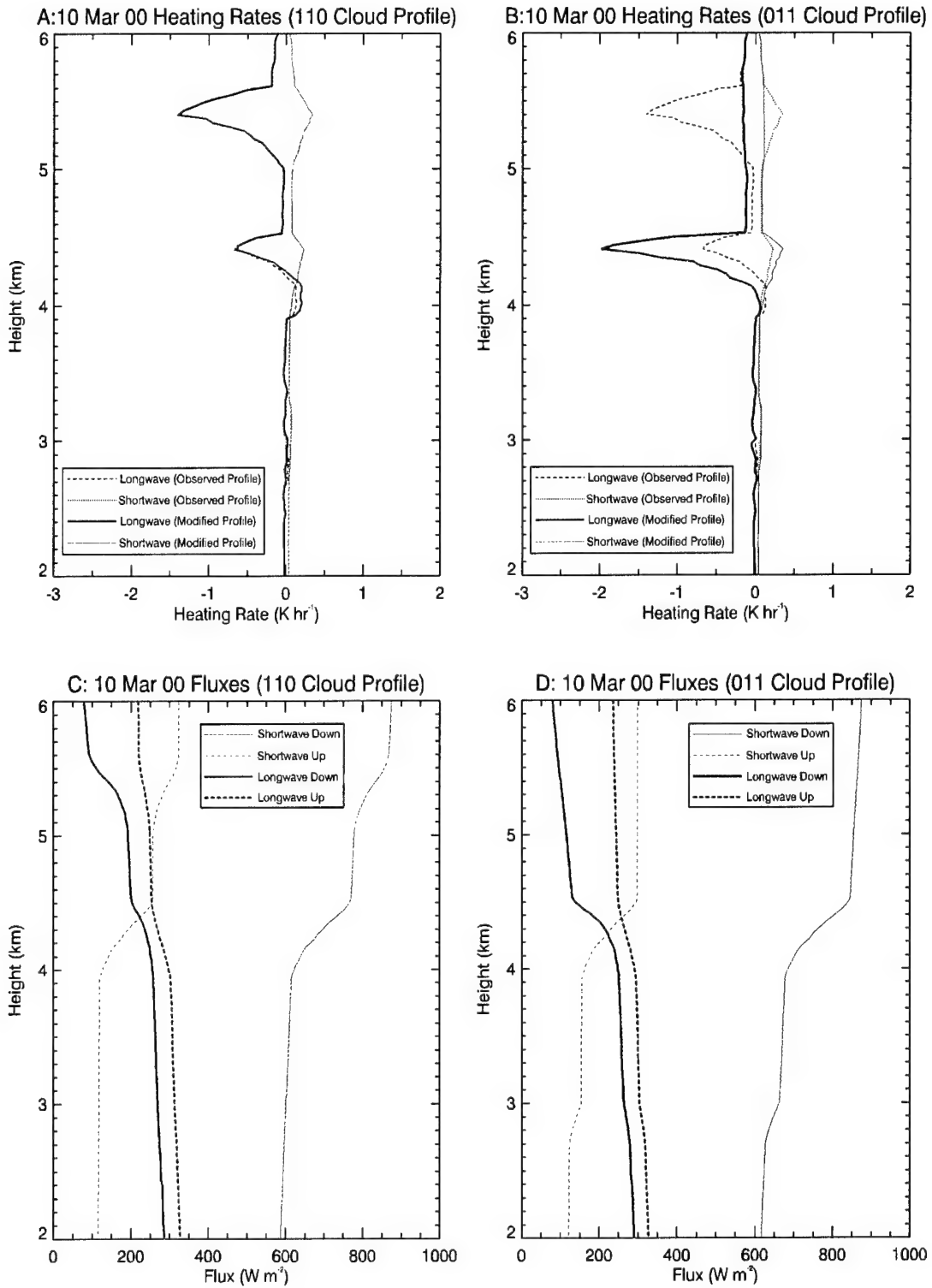


**Figure 9.25** Same as the previous two figures except for cases in which only the top two layers (110) and the bottom two layers (011) are included in the profile. The “110” profile in (A) nearly mirrors that of the observed case, while the longwave cooling in the middle layer dominates the “011” profile in (B).

in the profile; “001” includes only the bottom layer, etc. “111” is the control case with all layers included, as shown in Figure 9.6, and is included as a dashed line on the other cases for ease of comparison.

Starting with the 10 Mar 00 cloud case, recall that the system consisted of relatively thin layers of small lwc and iwc, with the iwc homogeneously distributed through the system. In the control case, the peak longwave cooling/shortwave heating rate for the top two layers is  $1.4/0.35 \text{ K hr}^{-1}$  and  $0.67/0.23 \text{ K hr}^{-1}$ , respectively. When the lowest two layers are removed in the “100” case, the shortwave heating rate remains unchanged, but the cooling rate drops from 1.4 to  $1.1 \text{ K hr}^{-1}$ , due to less longwave flux divergence. However, when the top and bottom layers are removed (010), the longwave cooling and the shortwave heating of the middle layer increase to  $1.94$  and  $0.35 \text{ K hr}^{-1}$ , respectively. This threefold increase in cooling occurs because the former middle cloud can now emit energy directly to space, instead of reabsorbing a portion of this energy from the emitting cloud layer above. In this way, the flux divergence is greater when no clouds are present above a given layer. Note that the net cooling effect of the isolated middle layer is greater than that of the top layer alone; the reason for this difference is mainly due to a higher lwc in the middle layer than the top layer.

Because the bottom layer is extremely thin and contains little liquid water or ice, it has a negligible effect on the net radiative heating rate profile of most cases. The two cases in which there is evidence of its existence are the case in which the top two layers have been removed (001) and the “101” case, where the middle cloud is excluded. In the first instance, where the bottom layer is isolated, there is a fairly large increase in the longwave cooling rate, from less than 0.10 to just over  $0.70 \text{ K hr}^{-1}$ . This is still a

relatively small rate quantitatively, but is interesting due to the prominence of the feature when compared to the tiny effect it has when the upper layers are included. There is also a small shortwave heating rate of  $0.14 \text{ K hr}^{-1}$  seen when only the bottom layer is present, but is near zero when the total three-layer cloud profile is used. In the “101” case, the longwave cooling rate of the bottom layer decreases from  $0.70$  to  $0.28 \text{ K hr}^{-1}$ , due to some radiative feedback from the top layer. However, the bottom layer “shields” the top layer from the warmer source region below, and allows the top layer to cool at approximately  $0.10 \text{ K hr}^{-1}$  faster than it did when the middle and bottom layer were absent from the profile.

Turning to Figures 9.26 through 9.28 for the 12 Apr 00 cloud case, the most noticeable effects of multiple layering are found when isolating each of the three layers. Note that the longwave cooling and shortwave heating rates at the top of the “100” case are the same as for the profile in which all of the layers are included. However, with the bottom two cloud layers removed from the profile, the longwave heating rate becomes  $2.7 \text{ K hr}^{-1}$  at 6400 m, near the base of the remaining layer. This amount of longwave heating is in contrast to the negligible net heating at this level in the “111” case, due to the differences in flux convergence when the bottom of the cloud is allowed to interact more directly with the upwelling flux from the surface of the Earth, rather than the two intervening cloud layers beneath it.

A similar but reverse situation is true for the “001” case; the longwave heating rate at cloud base remains the same as for the all-layers case, but with the upper layers removed, the top of the layer exhibits a longwave cooling rate of  $6.2 \text{ K hr}^{-1}$  and a shortwave heating rate of  $1.5 \text{ K hr}^{-1}$ . This is again in contrast to the near-zero net heating

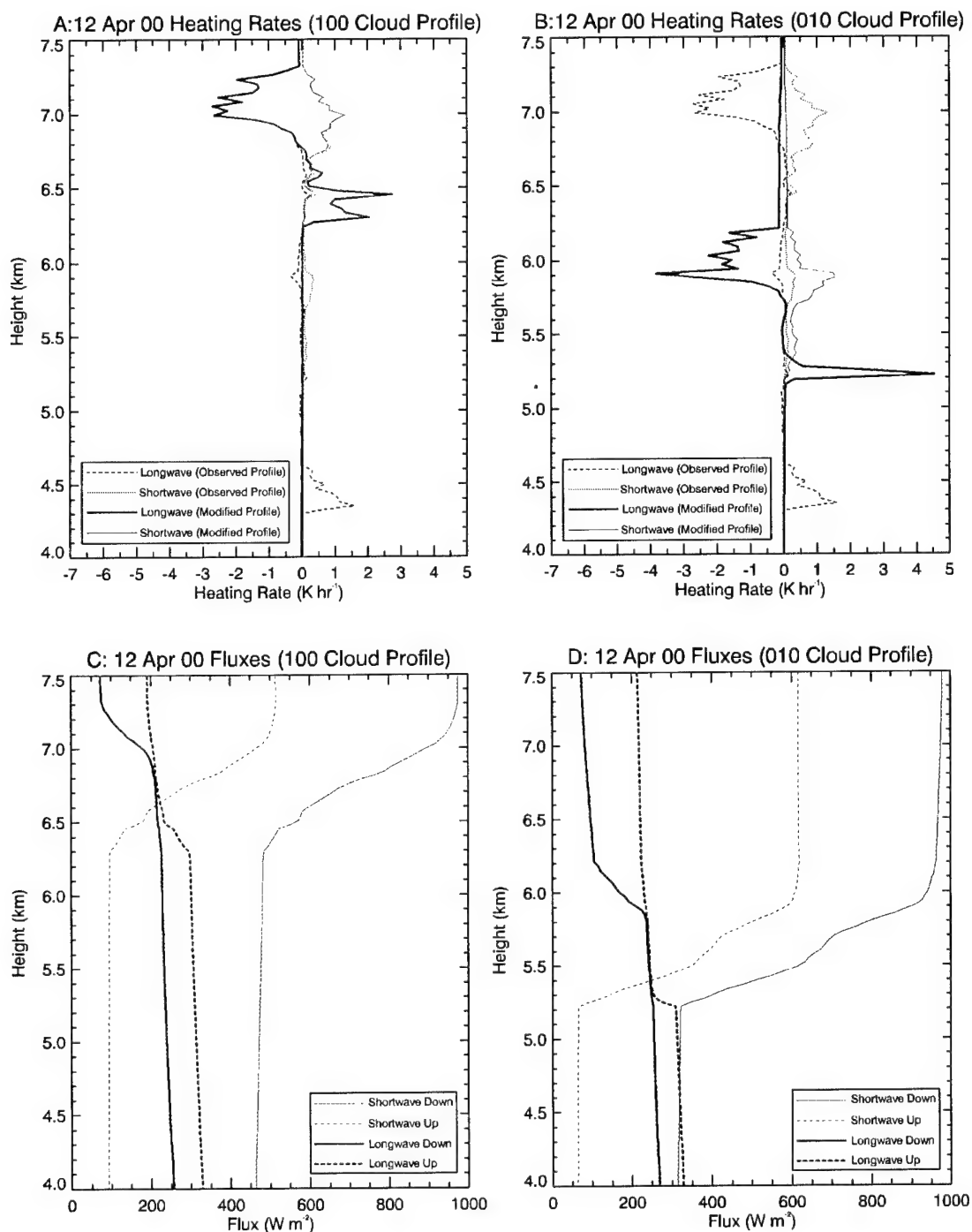


**Figure 9.26** Same as Fig 9.23 except for 12 Apr 00. In panel (A), note the longwave heating at the base of the top layer when removing the bottom layers. Likewise, panel (B) shows both radiative heating and cooling in the middle layer that was completely absent when all three layers were present.

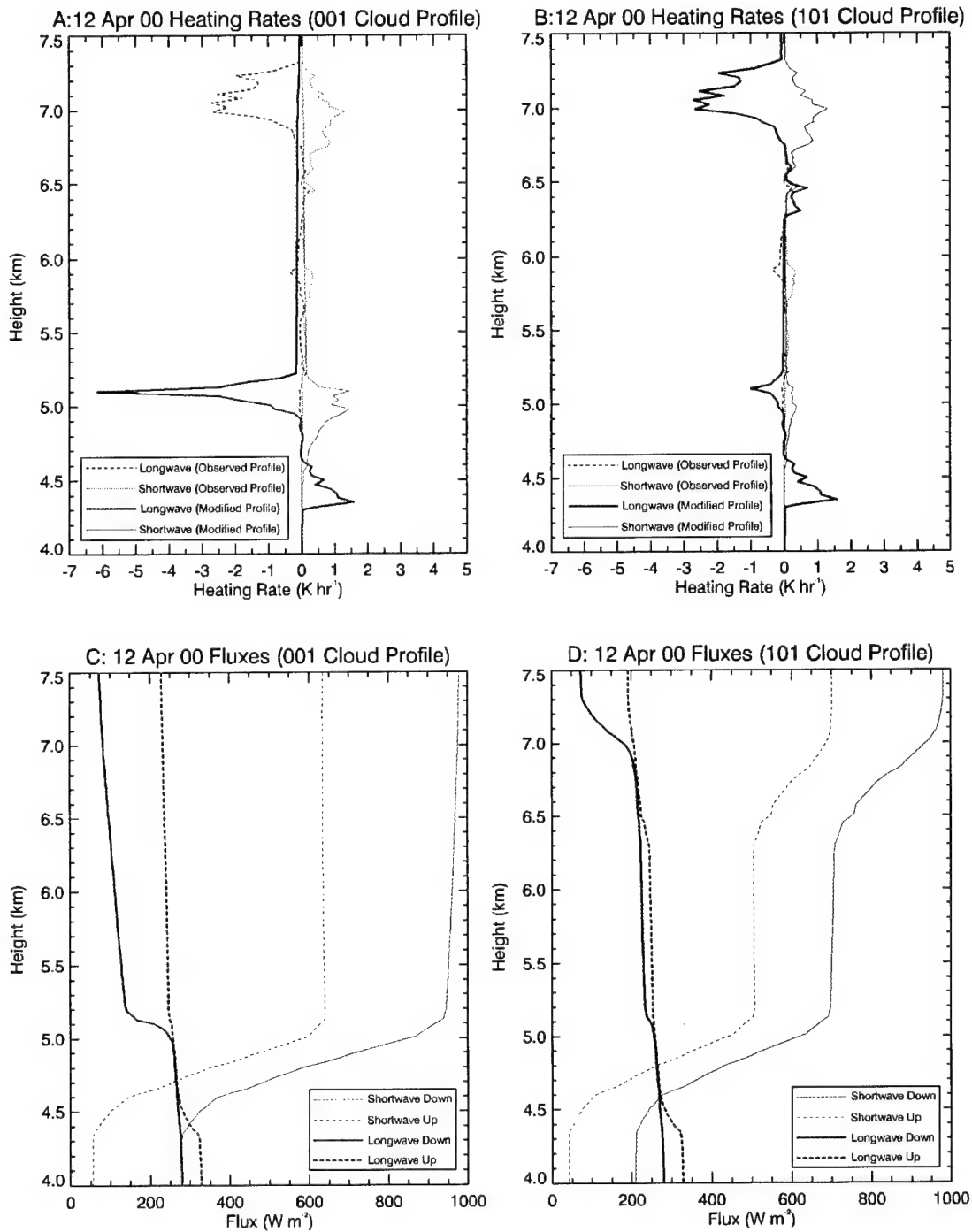


**Figure 9.27** Same as Fig 9.24 except for 12 Apr 00. Significant longwave cooling is apparent in (A) when the lowest layer is allowed to radiate without interacting with upper layers; from zero when layers are present to 6  $\text{K hr}^{-1}$  when they are removed. The net radiative profile will change with time as layers develop and dissipate.

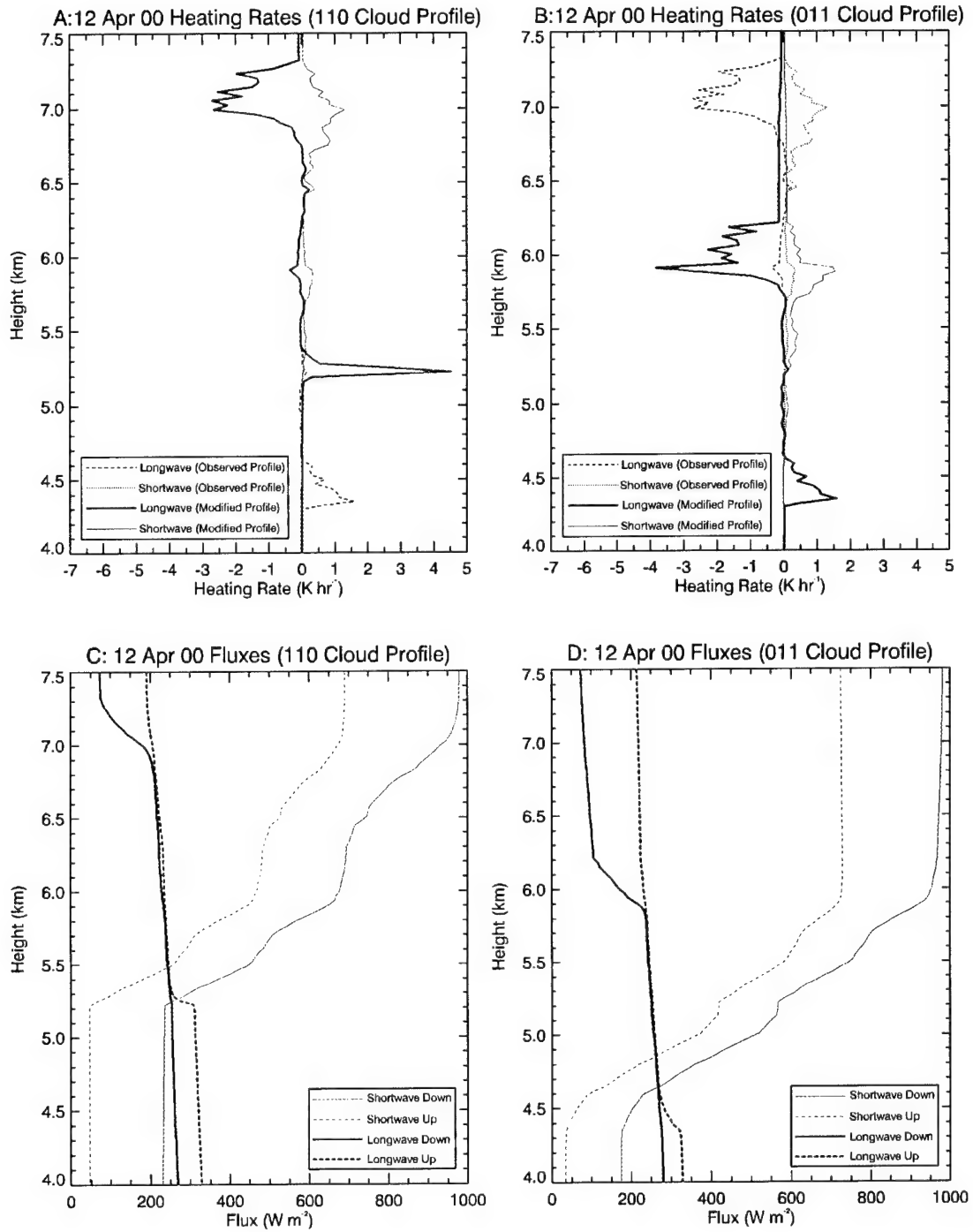


**Figure 9.28** Same as Fig 9.25 except for 12 Apr 00. Note that the bottom of the lowest layer and the top of the top layer interact radiatively as if they were a single cloud layer. However, since the differential heating acts over a greater vertical distance with multiple layers, the radiatively driven circulations will be weaker.

rate that occurs at the top of the bottom layer when the top two cloud layers are included. In this case, the cloud top can radiate more directly to space in the longwave part of the spectrum and receive shortwave energy more directly from the sun.

The largest departure from the net heating profile of the control case occurs when the middle layer is isolated in the “010” case (Figure 9.26B). The  $3.8 \text{ K hr}^{-1}$  longwave cooling rate and  $1.5 \text{ K hr}^{-1}$  shortwave heating rate at cloud top, as well as the  $4.5 \text{ K hr}^{-1}$  longwave heating rate at cloud base, are in stark contrast to the near-zero values seen at those levels in the control case. As previously noted, the apparent lack of net radiational heating at the mid-layer levels in the multi-layer case is due to the compensating effects of cooling from the layer below and warming from the layer above. As a result, if any of the three layers dissipates, the net radiational cooling to space and warming to the surface of the Earth will change, due primarily to the differences in lwc, iwc, and the height of the remaining cloud layer(s).

The microphysical and physical characteristics of cloud layers have an important implication for the radiatively induced circulation strength of single versus multiple layers. Specifically, with all other atmospheric conditions held constant, a single-layer cloud with a given lwc, iwc and height should have a more vigorous circulation than if it was part of a multi-layered system. This is especially evident in the 12 Apr 00 “010” case just shown, as the vertical differential heating rate increased from near zero when the cloud was sandwiched between the other two layers, to approximately  $7.0 \text{ K hr}^{-1}$  when it was isolated. Likewise, the longwave heating component is missing at the base of the top layer, and the longwave cooling and shortwave heating are absent from the top of the bottom layer in a multi-layered system, reducing the differential heating gradient

from that which they would experience as a single layer. Unfortunately, we can only speculate on these differences in circulation strength, because we do not have the vertical wind measurements in the two multi-layer clouds to demonstrate this more conclusively.

#### **9.4 Mid-level, Mixed-Phase Cloud Radiative Parameters**

In an effort to synthesize the data into some meaningful quantitative information for mid-level cloud modeling or remote sensing studies, several radiative parameters were calculated from the spiral sounding data for the clouds modeled in previous sections. The results are listed in Table 9.3 and include effective radii for liquid droplets and ice particles, liquid and ice water paths, and optical depths for liquid, ice and total water. Cloud depth and the mean liquid and ice water contents from the aircraft soundings are also included for quick reference. Several assumptions were made when computing the various parameters and are discussed below.

First, note that the cloud depths for the multi-layered cloud systems on 10 Mar and 12 Apr 00 do not include the clear air between the layers, but are the sums of the three cloud layers in each system. This was done to avoid confusion concerning the calculation of liquid water path (lwp), ice water path (iwp), and optical depth ( $\tau$ ), as the values shown in the table represent only those through the depth of the cloud. For reference, the 10 Mar 00 cloud layers were 400, 800 and 625 m thick, while the 12 Apr cloud layers were 900, 680, and 780 m thick. The actual values of lwp, iwp, and  $\tau$  would all be slightly larger in reality due to small radiative interactions with gases and particulate in the clear air between layers.

**Table 9.3 List of mid-level cloud radiative parameters for use in cloud modeling or remote sensing studies, including cloud depth, mean liquid water content (lwc), mean effective radius for liquid droplets and ice particles ( $r_{\text{eff}}$ ), liquid water path (lwp), ice water path (iwp), and the optical depths for liquid droplets ( $\tau_{\text{liquid}}$ ), ice particles ( $\tau_{\text{ice}}$ ), and the combination of liquid and ice ( $\tau_{\text{total}}$ ).**

(Spirals)	Cloud	Liquid			Ice			$\tau_{\text{liquid}}$	$\tau_{\text{ice}}$	$\tau_{\text{total}}$
	depth [m]	lwc [g m <sup>-3</sup> ]	$r_{\text{eff}}$ [ $\mu$ ]	lwp [g m <sup>-2</sup> ]	iwc [g m <sup>-3</sup> ]	$r_{\text{eff}}$ [ $\mu$ ]	iwp [g m <sup>-2</sup> ]			
<b>11 Nov 99</b>	525	0.13	12.2	84.6	0.02	114.3	8.5	10.4	0.12	<b>10.5</b>
<b>2 Dec 99</b>	550	0.06	7.8	27.2	0.01	146.9	2.1	5.2	0.02	<b>5.2</b>
<b>5 Dec 99</b>	610	0.09	10.2	73.4	-----	-----	-----	10.8	-----	<b>10.8</b>
<b>10 Mar 00</b>	1825	0.01	14.0	19.9	0.01	212.9	32.4	10.6	0.25	<b>10.9</b>
<b>12 Apr 00</b>	2360	0.10	21.4	167.4	0.23	314.9	727.9	11.7	3.85	<b>15.6</b>

The effective radii (e.g., Stephens, 1994) for cloud liquid droplets were calculated from FSSP size and concentration information. This calculation essentially involves dividing the liquid droplet volume by its cross-sectional area. The same calculation was done for the ice particles using the 2D-C data, but there are errors associated with the non-sphericity of particles. Specifically, the 2D-C data gives information about the maximum dimension of the ice particles; the more non-spherical the particles are, the more errors there are in the effective radius values. From the CPI images shown in Chapter 5, these errors should be reasonably small (<20%) due to the large amounts of riming on the basic needle, plate, and stellar crystal structures.

The liquid water paths were calculated by summing the product of the mean lwc and vertical depth at every 30 m through the cloud. Ice water content was calculated by the same method, using the mean ice water contents over 30 m intervals. The errors

associated with these calculations are minimal, but a slight increase in accuracy may have been obtained by using smaller vertical increments. The 30 m interval was chosen to mirror the vertical grid spacing of the BUGSRAD model input.

Liquid optical depth for visible wavelengths was calculated using the approximation:

$$\tau_{liquid} = \frac{3}{2} \frac{lwp}{\rho_{liquid} (r_{eff})}$$

where  $\rho_{liquid}$  is the density of liquid water and  $r_{eff}$  is the effective radius of the liquid water droplets. The “2” in the denominator approximates the efficiency factor for extinction as a function of size parameter for a single particle, and is valid for situations in which particle sizes are large relative to the wavelength. The optical depth of the cloud due to ice particles was calculated the by the same method, only using  $iwp$  and the density of ice instead of  $lwp$  and the density of liquid water. As noted in Stephens et al. (1990), the density of ice varies according to ice crystal size and habit. In this study, we assume a fixed value of  $0.9 \text{ kg m}^{-3}$  for the density of ice and ignore its variation on particle size. This value has been used in recent studies by Francis et al. (1998) and Francis et al. (1999) and is conservative, since a smaller  $\rho_{ice}$  would result in larger values of optical depth. Once the optical depths for liquid and ice were calculated, they were simply added together for the total optical depth,  $\tau_{total}$ .

Despite the sources of error in each of the calculations leading to total optical depth for the visible wavelengths, the resulting values are consistent and show a mean value of 10.6 for the mid-level clouds measured during CLEX. Once again, these values are conservative, but serve as a good baseline for modeling and remote sensing studies.

## **10. Summary and Implications of Results**

This dissertation describes airborne measurements of the microphysical and radiative structures of six mid-level clouds obtained in late Autumn 1999 and early Spring 2000. The cases were comprised of one single-layer cloud consisting primarily of liquid water; three single-layer, mixed-phase clouds; and two multi-layered, mixed-phase clouds. The detailed descriptions and analyses of these clouds provide a basis for the initialization and evaluation of cloud models that fully utilize mixed-phase cloud microphysics. A further goal of this research is to use the newly acquired knowledge of the microphysical and radiative structures presented in the preceding chapters to improve mid-level, mixed-phase cloud forecasts and model parameterizations. The following summary of the research findings includes applications of the results to enhance existing forecasting and modeling techniques.

### **10.1 Synoptic and Mesoscale Situations**

The synoptic and mesoscale forcing that characterized the cloud regions from which the six measurements were obtained was discussed and compared. The clouds were often associated with a 500-mb low-pressure center and/or potential vorticity advection. The 11 Nov 99 cloud formed as a PV maximum swept into northern MT and provided some lift for moisture being advected around the apex of a large ridge axis. The five cloud cases in OK all developed in association with a 500-mb low-pressure center.

With the exception of the “wrap-around” cloud embedded in northerly flow on 5 December 1999, the other clouds usually formed in southwesterly to westerly flow ahead of a 500-mb low in the TX panhandle region. The development of these clouds may have been aided by rising motion in the right front exit region of the jet streaks at 200-300 mb.

Forecasters concerned with mid-level cloud formation should search the atmospheric sounding data for moist layers of air that may be subject to large-scale or mesoscale lifting mechanisms, such as frontal systems, jet streaks, potential vorticity advection with a shortwave trough, or orographic lift. Moisture often advects into an area as an integral part of a large-scale system, such as low-pressure centers moving into the continental U.S. from the Pacific Ocean or the Gulf of Mexico. During the warmer months of the year, mid-level moisture may be supplied from upstream convection. Detrained convective moisture will not be as apparent as that associated with large-scale systems and therefore may not be included as input into numerical weather prediction models. This source of mid-level moisture is often missed by the sounding data, due to the smaller spatial and temporal scales of convectively produced moisture.

In the absence of large-scale lift, mid-level moisture may still ascend and condense to form clouds through radiative processes. This is especially true as sunset approaches, because net cloud top cooling increases when solar heating ceases, as shown by the radiative sensitivity to solar zenith angle in Chapter 9 (e.g., figures 9.18 and 9.19). Conversely, mid-level cloud dissipation may occur shortly after sunrise, as shortwave heating causes a decrease in net cloud top cooling that weakens circulations, especially in thinner clouds. Perhaps the most difficult mid-level clouds to forecast are those in which

detrained moisture is radiatively cooled to form clouds at night. Since this type of cloud is relatively thin, it will likely dissipate the following morning. Clouds formed by this mechanism are relatively short-lived and difficult to detect; they could have a significant impact on nighttime military operations, by obscuring the ground and hampering the use of electro-optic weaponry.

## 10.2 Measurements

Mean values of the microphysical parameters were highlighted and contrasted. Clouds were sampled from 2390 to just over 7000 m in altitude, with corresponding pressures of 400 to 750 mb, and were typically 500-600 m in depth. In-cloud temperatures ranged from just below freezing to a low of  $-31^{\circ}\text{C}$ . The peak liquid water content was  $0.35\text{ g m}^{-3}$  near the top of the 5 Dec 99 case, with mean values of horizontal racetracks generally between 0.01 and  $0.15\text{ g m}^{-3}$ . Mean ice water contents varied from a low of near  $0.01\text{ g m}^{-3}$  for the 2 Dec 99 case to a high of  $0.22\text{ g m}^{-3}$  for the 12 Apr 00 case. Wind directions were from  $180$  to  $270^{\circ}$  for all but the 5 Dec 99 case, which was from  $350^{\circ}$ . Horizontal speeds increased with height and were normally  $25$  to  $30\text{ m s}^{-1}$ . The standard deviation of the vertical wind was normally  $0.15$  to  $0.75\text{ m s}^{-1}$ , giving a relative measure of mixing and turbulence between the various cases.

### 10.2.1 Cloud Structure

Several structural questions were examined. The first question dealt with the vertical structure of lwc and iwc in mixed-phase clouds. Vertical profiles of lwc increased with height, while iwc decreased with height through single-layer clouds. One

exception was the pseudo-convective cloud on 4 December 1999, which was measured after being convectively mixed in a series of squall lines. The ice profile in this case was more evenly mixed through a vertical layer than in the other more quiescent single-layer cases. In the multi-layered cases, the iwc was uniformly distributed through each of the cloud layers.

Regarding the observed differences in iwc distribution between single- and multi-layered clouds, we propose that a seeder-feeder mechanism caused the disparity. In this hypothesis, ice sedimentation led to a peak in iwc near the bases of single clouds, but fed the lower layers in multi-layered systems. If ice particles are not continually introduced into the top of a cloud, sedimentation will cause the ice to settle to the bottom of the cloud, as it did in the single-layer cases. The presence of ice crystals having growth habits from temperatures colder than the height at which they were observed in the 2D-C measurements and CPI imagery supported the theory of the seeder-feeder process. There was also an order of magnitude difference in lwc between the two multi-layered systems, from a mean of about  $0.01 \text{ g m}^{-3}$  in the 10 Mar 00 case to approximately  $0.10 \text{ g m}^{-3}$  for the 12 Apr 00 case. We attributed this dissimilarity to differences in forcing, speculating that more vigorous cloud circulations on 12 Apr 00 caused increased production of liquid water and a concomitant increase in the rate of ice particle growth.

The microphysical structure of clouds is of primary importance to numerical weather prediction and global climate models. The mixed-phase structure of mid-level clouds affects cloud lifetime. If the lwc production rate is greater than the bulk ice growth rate and can maintain the cloud against mass depletion due to sedimentation, the cloud may sustain itself for a long period of time. For a weather forecast, this will

determine whether or not there is mid-level cloud cover over an area. For a general circulation model, the cloud lifetime affects the Earth radiation budget. The longer the cloud exists, the more net cooling to space. If the system is layered, higher layers cool to space more than lower layers; if upper layers glaciate first, then the lower layers will radiate to the top of the atmosphere at increasingly warmer temperatures.

The structure is also important for aviation. The supercooled liquid water at the tops of the single-layer clouds pose a light to moderate icing hazard, whereas the increasingly high concentration of ice near the cloud base is more conducive to light rime icing. Aircraft transiting multi-layered clouds are also more susceptible to light rime icing, as the available supercooled liquid will be more readily used for ice particle growth. Additionally, due to the correlation between lwc, net radiative forcing, and circulation strength, single-layer clouds are more likely to contain more intense turbulence than multi-layered clouds.

#### 10.2.2 Droplet Spectra

Liquid droplet spectra from the single-layer cases showed the peak concentration was of the smallest droplets in the lower parts of the clouds. As altitude increased, the droplet spectrum shifted until the greatest concentration of the largest droplets was found at or near cloud top. For the multi-layered cases, the largest concentrations were generally for the droplet sizes in the 14-16  $\mu\text{m}$  range, with the exceptions noted. The homogeneous distribution of smaller droplets was probably due to the large amounts of ice through all of the layers of both multi-layered cases, depleting the liquid water via the Bergeron-Findeison process.

The modes were not as clear for the ice particle spectra as they were for the liquid droplets. In the single-layer cases, the largest concentrations were of ice particles having radii on the order of 80-100  $\mu\text{m}$ , with a smaller concentration of larger particles at the base of the cloud. The multi-layered cases both showed rather homogeneous concentrations of particles with altitude, but the sizes increased toward cloud base for the 12 Apr 00 case, in contrast to more uniform sizes in the 10 Mar 00 case. The differences are attributed to the order of magnitude higher lwc amounts on 12 Apr 00.

### 10.2.3 Role of the CPI in Mixed-Phase Cloud Studies

The role of the Cloud Particle Imager in studies of mixed-phase clouds was highlighted. In past observational work, PMS probes have suffered from various errors in mixed-phase clouds, limiting their utility in these conditions. These errors were described in some detail, along with the methods used to minimize the effects in the ensuing analysis. The CPI greatly aided our qualitative analyses on several occasions, including the accurate discrimination of liquid droplets from ice particles down to sizes of about 5  $\mu\text{m}$  in radius. The imagery also provided the sizes and shapes of particles, ice crystal habits, and the effects of riming and sublimation. Without this information from the CPI, there would have been more errors in the lwc and iwc measurements. The CPI also helped to reliably determine the seeder-feeder mechanism in multi-layered clouds, as well as the riming and sublimation processes that pointed to cyclic growth through several of the clouds.

The actual sizes and shapes and the large departures from “pristine” crystals seen in the imagery are extremely important for radiative transfer and remote sensing, since

scattering of energy is largely dependent on these parameters. Building single-scattering properties that best represent mixed-phase clouds is problematic at best. However, a good approximation may start with the basic ice crystal habits in various temperature ranges, with an added factor to account for riming growth, sublimation, multi-axis growth, etc. "Pristine" crystals are very rare in CPI images from the CLEX clouds, as a great deal of particle growth and decay occurred in mixed-phase conditions. The basic needle, stellar, or plate-like structure is somewhat evident in the CPI images and must play a role in determining the basic ice particle shape.

#### 10.2.4 Thermodynamic Structure

Another question we examined was the thermodynamic structure of the clouds, particularly discontinuities in vertical profiles that might give clues to the processes driving cloud motions and affecting microphysical structure. An interesting finding, and in contradiction to our preconceived paradigms regarding stratus and stratocumulus clouds, was the lack of temperature inversions or wind shear at the top and bottom of clouds. Several observational studies of low-level boundary layer clouds had easily identifiable temperature inversions of 2 to 10° C at cloud top, but there were no such inversions evident in any of the six CLEX cases. We attributed this disparity to differences between the boundary layer-trade inversion mechanics of stratocumulus systems, which are a combination of thermodynamic, moist convective, and radiative processes, and the primarily radiative processes creating inversions above mid-latitude, mid-level clouds. Virtual potential temperature was found to be the best indicator of

cloud boundary for the systems we observed, with changes of only 1 to 2° C evident at most of the interfaces.

Wind shear was similarly scarce in the data, with only one noteworthy directional shear of about 35° on 10 Mar 00. Otherwise, vertical wind profiles did not vary by more than 10° in direction or 5 m s<sup>-1</sup> in speed. Again, the differences between the stratocumulus and mid-level cloud wind shear were due to the mechanics of the coupled boundary layer versus the decoupled atmosphere at mid-levels.

Because relatively little is known about the structure of mid-level clouds, some models may have applied known stratocumulus or cirrus structure parameterizations to the mid-cloud layers. However, since neither temperature inversions nor wind shear was observed in CLEX clouds, such parameterizations may introduce unexpected errors into numerical models that treat mid-level clouds as elevated stratocumulus layers and attempt to “force” these parameters on the clouds. For example, imposing a cloud top inversion on a mid-level cloud may cause less effective mixing with the ambient air above cloud, or the imposition of cloud top wind shear may bring about more mixing than would actually be realized through normal radiative processes. The point is that some aspects of altocumulus should be parameterized, but the parameterization would have to be different than that for stratocumulus or cirrus clouds.

An assessment of the relationship between temperature and iwc yielded similar results to recent studies of Arctic stratus; namely, there is a poor correlation between the two quantities. The iwc was a maximum in the -8 to -20° C temperature range, corresponding to the regime in which the difference between saturation vapor pressure with respect to ice and water maximizes, and to the regime in which ice crystals with

plate-like structure grow most rapidly. Models that use temperature to parameterize cloud phase will have errors associated with them. The cloud microphysical structure will be wrong, affecting the overall evolution and radiative structure. Two specific examples will be discussed in more detail in the summary of findings from the radiative sensitivity studies.

### **10.3 Comparison of Findings with Other Observations and Cloud Processes**

Observations of cloud depth, lwc, temperature, and vertical wind from previous studies were in good agreement with the CLEX measurements. This provided an added degree of confidence in the data and analysis of the aircraft observations, allowing for further exploration of the similarities and differences between mid-level clouds, as well as those between mid-level and boundary layer clouds.

After determining the microphysical structure, the CLEX findings were coupled with a literature review to provide an overview of the primary formation, maintenance and dissipation processes governing mid-level, mixed-phase clouds. Mid-level moisture and ascent are the two main ingredients for cloud formation. Radiative processes play a key role in the lifetime of mid-level clouds as differential radiative heating induces the updrafts necessary to produce liquid water. The bulk condensation rate must outpace the bulk ice growth rate to prevent the cloud from glaciating. The concentration of ice forming nuclei, the size and concentration of liquid droplets, the sedimentation rate of large ice particles, the entrainment rate, and the large-scale vertical velocity field are other primary factors to consider in determining the lifetime of a mixed-phase cloud.

#### **10.4 Death of an Altocumulus Cloud**

The specific physical mechanisms responsible for the maintenance and dissipation of the 11 Nov 99 cloud observed during CLEX were examined. To accomplish this, a budget of the vertically averaged specific liquid water content was constructed so the large-scale subsidence, radiative heating, entrainment drying, and sedimentation fallout could be computed. Subsequent analysis showed that the evolution of the 11 Nov 99 cloud was governed primarily by large-scale ascent and then subsidence. The liquid water budget revealed that the largest contributor to decay of liquid water is subsidence drying, and the smallest contributor is sedimentation. The role of radiative cooling was particularly interesting; liquid water increases due to radiative cooling, but it is offset by radiatively induced entrainment drying, making it unclear whether the net effect of radiative cooling is to prolong or curtail cloud lifetime. The main result of the budget analysis, though, indicates that future altocumuli studies should put more emphasis on the large-scale velocity and moisture fields, instead of focusing exclusively on the microphysics.

#### **10.5 Radiative Effects and Sensitivities**

The radiative fluxes and heating rate profiles through the observed mid-level clouds were modeled using the BUGSRAD single-column radiation code from the CSU GCM. Results of these cases were used as a basis to examine the sensitivity of radiative processes to microphysical and physical changes that occur in mid-level, mixed-phase clouds. Since several of the implications for forecasting and modeling were already discussed in Chapter 9, only the highlights are recapitulated here.

### 10.5.1 Sensitivity to Liquid and Ice Water Content

By doubling and halving the lwc and iwc, it was shown that the fluxes and heating rates are directly correlated to the amounts of liquid and ice through the cloud systems, particularly at cloud base and cloud top. The higher the lwc, the larger the vertical differential radiative heating rate, and the stronger the resulting cloud circulation. Dry air entrainment provides a negative feedback to this process, so it is imperative that the correct amounts of lwc and iwc are used, as they play a large role in dictating the lifetime of the system. It was also shown that not only the lwc or iwc amount affects the radiative profile, but the vertical placement of the condensate as well. Net cloud top radiative cooling was maximized when the lwc or iwc was a maximum at cloud top; smaller quantities above the maximum resulted in smaller radiative cooling rates. Thus, it is important to know if dry air entrainment has eroded the cloud top lwc to cause a decrease in the amount of net radiative cooling.

### 10.5.2 Sensitivity to Cloud Water Phase

Incorrect parameterizations of cloud phase using temperature will cause large errors in the radiative properties of mid-level clouds. The ECMWF and CSU GCM models seem to be representative of the more sophisticated numerical weather prediction and general circulation models currently available, yet for lack of a better parameterization scheme, they use temperature to determine the liquid to ice ratio. Inverting the 11 Nov 99 cloud so that ice would increase toward cloud top resulted in a net vertical differential radiative heating rate of about  $5 \text{ K hr}^{-1}$ . Since  $-20^\circ \text{C}$  is a typical

threshold for strictly delineating phase, the 2 Dec 99 case in the  $-27$  to  $-30^{\circ}\text{C}$  range would have been classified as an all ice cloud, leading to errors in the vertical differential net radiative heating rate of 400%.

Although temperature is obviously not a good choice, a better set of parameters for determining cloud phase remains unclear. Hobbs and Rangno (1985) and Pinto (1998) suggest that cloud age is probably the best discriminator; the older a cloud is, the more ice it will have (given below freezing temperatures, of course). Hobbs and Rangno also point to a correlation between ice concentration and liquid droplet sizes in which ice particles tended to form in concentrations of one per liter when droplet sizes reached approximately  $20\text{ }\mu\text{m}$  in diameter. An equally important consideration, but one that is much more difficult to ascertain due to spatial and temporal variability, is the number of ice forming nuclei in a system (e.g., Harrington et al., 1999). A low concentration of ice nuclei is the only viable way to explain the limited amount of ice particles in the 2 Dec 99 cloud, but there was no particle counter on the aircraft to verify this hypothesis, so it remains speculative.

Finally, future observational studies of the microphysical structure should explore the possibility of parameterizing the vertical ice water content distribution as a function of its shape relative to cloud base and cloud top. For example, the 11 Nov 99 case showed an increase of iwc with decreasing height in the cloud, a maximum about 100 meters above cloud base, and then a decrease towards the cloud base. If other single-layer clouds show a similar distribution, it may be worthwhile to parameterize cloud iwc based solely on the shape of the distribution, rather than some combination of microphysical factors.

### 10.5.3 Sensitivity to Shortwave Heating

Solar elevation angles affect the amount of shortwave heating at cloud top, and therefore the net radiative heating profile of a cloud layer. This produces a diurnal cycle in mid-level cloud frequency of occurrence. The net vertical differential heating rate is reduced after sunrise, reducing the strength of the cloud circulation and the production of liquid water. If the cloud is only generating enough condensate to keep pace with the bulk ice growth rate, any decrease will result in glaciation and dissipation. Conversely, the decrease of shortwave heating at cloud top after sunset may increase the internal circulations enough to produce the condensate necessary for new cloud formation or cloud growth.

### 10.5.4 Sensitivity to Cloud Height

Even if the correct microphysics are input into a model, incorrect cloud heights will result in flawed radiative profiles. With all other parameters constant, the associated air density differences involved in displacing the cloud lwc to a different height will give rise to different amounts of radiative heating and cooling. For the 2 Dec 99 case, a location error of one kilometer results in longwave and shortwave heating rate errors of approximately  $1 \text{ K hr}^{-1}$  each. These errors would increase for clouds containing more liquid and ice than the 2 Dec 99 cloud.

### 10.5.5 Sensitivity to Cloud Layering Effects

The effects of layering were demonstrated by eliminating various combinations of cloud layers from the vertical profiles. The net radiative heating profiles are sensitive to

absorption, emission, and scattering interactions between the layers. To capture the effects of layering, a model must account for the various formation and dissipation processes in the system. For example, seeder-feeder processes were evident in the multi-layered cloud cases, with ice particles from upper layers feeding the lower layers. If the upper layers dissipate due to sedimentation or other cloud decay processes, the tops of the next highest layers will radiate directly to space at a different rate; likewise, if lower layers are eliminated first, the bases of the next lowest layers interact directly with upwelling radiation from the surface or boundary layer clouds. Moistening due to ice particle sedimentation and sublimation beneath a cloud layer may cause the formation of several successively lower layers, with varying amounts of lwc and iwc. In this way, the effects of changing cloud heights and the associated variations in radiative transfer complicate the forecast and global climate models.

Finally, several mid-level cloud radiative parameters were calculated, including liquid and ice water paths, effective radii for liquid droplets and ice particles, and optical depth for liquid, ice, and total water. These values serve as a good baseline for radiative parameterizations in models or remote sensing studies, especially those interested in mixed-phase clouds.

The main findings of this research are listed in bullet format in the concluding chapter, along with some prospective ideas for future work on mid-level, mixed-phase clouds.

## 11. Conclusions And Future Work

This study is based on aircraft measurements of six mid-level clouds and the observational findings from previous studies of mid-level or mixed-phase clouds. The conclusions can and should be used as a basis for forecasting, modeling and parameterizing mid-level, mixed-phase clouds, but should not be generalized as representative of all clouds of this type.

### 11.1 Conclusions:

- Five of six mid-level clouds were mixed-phase, containing both supercooled liquid water and ice particles; the sixth cloud contained only supercooled liquid despite temperatures of  $-6$  to  $-8^{\circ}\text{C}$ .
- Two of the three single-layer, mixed-phase clouds had maximum lwc at or near cloud top and maximum iwc at or near cloud base; the third cloud was convectively mixed prior to the aircraft observations
- The two multi-layered, mixed-phase clouds had a similar lwc profile, but the iwc was homogeneously distributed in the vertical, probably due to a seeder-feeder process operating between the cloud layers.

- A lack of strong temperature inversions or wind shear at mid-level cloud boundaries was a major difference from boundary layer clouds, which are coupled to surface processes and typically exhibit both of these traits.
- Virtual potential temperature was the best indicator of mid-level cloud boundaries.
- Neither ice concentrations nor iwc were correlated to cloud temperature. The highest iwc values were found between  $-8$  and  $-20^{\circ}\text{C}$ , corresponding to the maximum growth regime of ice crystals having plate-like structures and the regime in which the difference between saturation vapor pressure with respect to ice and water peaks.
  - Synthesizing CLEX research with past observational studies, a combination of temperature, cloud age, liquid droplet size, and ice forming nuclei concentration is a better discriminator of cloud phase than temperature alone.
  - Future model parameterizations should also explore methods for determining the ice distribution as a function of distance from cloud base and cloud top.
- The cloud particle imager was an invaluable tool for the qualitative analysis of mixed-phase clouds, especially for discriminating cloud phase and ice crystal habit.
- Comparisons with past observational studies of mixed-phase clouds showed good quantitative agreement with CLEX data, providing confidence in the measurements.

- Mid-level cloud formation requires moisture and a lifting mechanism. Radiative processes are important for the development of these clouds, as vertical differential heating drives the cloud circulations to produce condensate to the system.
- Maintenance of mixed-phase clouds requires that the condensate supply rate outpace the bulk ice growth rate. Sedimentation of ice particles minimizes the impact of the Bergeron-Findeison process on the available liquid water. The concentration of ice-forming nuclei is also extremely important, as low concentrations allow mixed-phase clouds to exist in a supercooled liquid state for long periods of time.
- The main dissipation mechanisms were those depleting the available cloud water and included radiative heating, subsidence, ice sedimentation, and dry air entrainment.
- An analysis of the liquid water budget for the “death” of the 11 Nov 99 altocumulus cloud showed that evolution was governed by large-scale ascent and then subsidence. The largest contributor to liquid water decay was subsidence drying; the smallest factor was sedimentation in this particular case.
- In the Lagrangian case, the role of radiative cooling was unclear, as differential vertical heating drove the internal cloud circulations, but also allowed for dry air entrainment into the cloud.

- Radiative fluxes and heating rates were directly correlated to the amounts of liquid and ice through the cloud systems. This was particularly apparent at cloud base and cloud top, where the radiation did not interact with intervening layers.
- The configuration of cloud lwc and iwc affects the radiative budget. Net cloud top radiative cooling was greatest when the maximum lwc or iwc was at cloud top; if dry air entrainment erodes cloud top moisture, net cloud top radiative cooling is damped.
- Incorrect parameterizations of cloud phase using temperature caused large errors in the radiative transfer through mid-level clouds. Classifying the 2 Dec 99 case as an all ice cloud led to errors in the vertical differential net radiative heating rate of 400%.
- Solar elevation angles affected the amount of shortwave heating at cloud top and, therefore, the net radiative heating profile of a cloud layer. This effect produced a diurnal cycle in mid-level cloud frequency of occurrence.
- With all other parameters constant, incorrect cloud heights resulted in flawed radiative profiles. A one-kilometer vertical displacement caused longwave and shortwave heating rate errors of approximately  $1 \text{ K hr}^{-1}$  each for the 2 Dec 99 case.
- To capture the effects of layering, models need to account for formation and dissipation processes in the system. The effects of varying cloud height and the associated variations in radiative transfer complicate forecasts and numerical models.

## 11.2 Future Work

- More mid-level cloud aircraft observations are needed to increase the database and verify earlier findings. Lagrangian measurements are superior to Eulerian measurements for determining maintenance and dissipation mechanisms.
  - The inclusion of cloud airborne radar would be extremely useful for obtaining cloud scale morphological, kinematic, and microphysical properties.
- The observed clouds should be simulated in a cloud resolving or mixed-layer model to further examine the interactions between dynamics, microphysics and radiative processes and to determine the primary mixed-phase processes.
- Remote sensing studies of clouds (CloudSat, MODIS, PICASSO-CENA, etc.,) would benefit from using the observed mixed-phase microphysics to test the response of specific instruments to mid-level clouds.
- Future research should examine the diurnal and seasonal cycles of mid-level clouds in more detail; evidence points to large shortwave heating impacts on cloud lifetime.
- Because of the relatively thick supercooled liquid layer at the top of single-layer, mid-level, mixed-phase clouds, discerning the ice particles would be difficult, but it would be interesting to determine if mixed-phase signals are present in current satellite data.

*The views expressed in this dissertation are those of the author and do not reflect the official policy or position of the United States Air Force, Department of Defense, or the US Government.*

## References

- Albrecht, B. A., D. A. Randall and S. Nicholls, 1988: Observations of Marine Stratocumulus Clouds During FIRE. *Bull. Amer. Meteorol. Soc.*, **69**, 618-626.
- Arnott, W. P., D. Mitchell, C. Schmitt, D. Kingsmill and D. Ivanova, 2000: Analysis of the FSSP Performance for Measurement of Small Crystal Spectra in Cirrus. Proceedings 13<sup>th</sup> International Conference on Clouds and Precipitation, Reno NV, 14-18 August, pp. 191-193.
- Baumgardner, D., W. Strapp, and J. E. Dye, 1985: Evaluation of the Forward Scattering Spectrometer Probe. Part II: Corrections for Coincidence and Dead-time Losses. *J. Atmos. Oceanic Technol.*, **2**, 626-632.
- Baumgardner, D., 1987: Corrections for the Response Times of Particle Measuring Probes. Preprints, 6th Symposium of Meteorological Observations and Instrumentation, New Orleans, 12-16 January. AMS, Boston, Mass., pp 148-151.
- Baumgardner, D., 1989: Airborne Measurements for Cloud Microphysics. NCAR Research Aviation Facility Bulletin 24, pp. 1-22.

\_\_\_\_\_ and M. Spowart, 1990: Evaluation of the Forward Scattering Spectrometer Probe. Part III: Time Response and Laser Inhomogeneity Limitations. *J. Atmos. Oceanic Technol.*, **7**, 666-672.

Biter, C. J., J. E. Dye, D. Huffman, and W. D. King, 1987: The Drop-Size Response of the CSIRO liquid water content probe. *J. Atmos. Oceanic Technol.*, **4**, 359-367.

Bretherton, C. S. and R. Pincus, 1995: Cloudiness and Marine Boundary Dynamics in the ASTEX Lagrangian Experiments. Part I: Synoptic Setting and Vertical Structure. *J. Atmos. Sci.*, **52**, 2707-2723.

Bretherton, C. S., P. Austin, and S. T. Siems, 1995: Cloudiness and Marine Boundary Layer Dynamics in the ASTEX Lagrangian Experiments. Part II: Cloudiness, Drizzle, Surface Fluxes, and Entrainment. *J. Atmos. Sci.*, **52**, 2724-2735.

Brost, R. A., J. C. Wyngaard, and D. H. Lenschow, 1982: Marine Stratocumulus Layers. Part II: Turbulence Budgets. *J. Atmos. Sci.*, **39**, 818-836.

Clough, S. A., F. X. Kneizys, and R. W. Davies, 1989: Line Shape and the Water Vapor Continuum. *Atmos. Res.*, **23**, 229-241.

Cober, S. G., G. A. Isaac, A. V. Korolev, and J. W. Strapp, 2000: Assessing the Relative Contributions of Liquid and Ice Phases in Winter Clouds. Proceedings of the 13<sup>th</sup> International Conf. on Clouds and Precipitation, Reno NV, 14-18 August, pp. 689-692.

Cooper, W. A., 1978: Cloud Physics Investigations by the University of Wyoming in HIPLEX 1977, Final Report, University of Wyoming, Laramie, WY, 320 pp.

Cotton, W. R. and R. A. Anthes, 1989: *Storm and Cloud Dynamics*. Academic Press, pp 745-787.

Field, P. R., 1999: Aircraft Observations of Ice Crystal Evolution in an Altostratus Cloud. *J. Atmos. Sci.*, **56**, 1925-1941.

Fowler, L. D., D. A. Randall and S. A. Rutledge, 1996: Liquid and Ice Cloud Microphysics in the CSU General Circulation Model. Part I: Model Description and Simulated Microphysical Processes. *J. of Climate*, **9**, 458-529.

Fu, Q. and K. N. Liou, 1992: On the Correlated k-distribution Method for Radiative Transfer in Non-homogeneous Atmospheres. *J. Atmos. Sci.*, **49**, 2139-2156.

Francis, P. N., P. Hignett and A. Macke, 1998: The Retrieval of Cirrus Cloud Properties from Aircraft Multi-Spectral Reflectance Measurements During EURCREX'93. *Quart. J. Roy. Meteor. Soc.*, **124**, 1293-1312.

Francis, P. N., J. S. Foote and A. J., Baran, 1999: Aircraft Measurements of the Solar and Infrared Radiative properties of Cirrus and Their Dependence on Ice Crystal Shape. *J. Geophys. Res.*, **104**, 31,685-31,695.

Gardiner, B. A. and J. Hallett, 1985: Degradation of In-cloud Forward Scattering Spectrometer Probe Measurements in the Presence of Ice Crystals. *J. Atmos. Oceanic Technol.*, **2**, 171-180.

Garrett, T. J., L. F. Radke and P. V. Hobbs, 2001: Aerosol Effects on Cloud Emissivity and Surface Longwave Heating in the Arctic. Submitted to *J. Atmos. Sci.*, Special Issue on Global Aerosol Climatology.

Gedzelman, S. D., 1988: In Praise of Altocumulus. *Weatherwise*, **41**, 143-149.

Geisler, J. E. and E. B. Kraus, 1969: The Well-Mixed Ekman Boundary Layer. *Deep Sea Research*, Supplement to Vol. 16, Pergamon Press, pp 73-84.

Hallett, J., and B. J. Mason, 1958: The Influence of Temperature and Supersaturation on the Habit of Ice Crystals Grown from the Vapor. *Proc. Roy. Soc.*, **A247**, 440-453.

Harrington, J. Y., T. Reisin, W. R. Cotton, S. M. Kreidenweis, 1999: Cloud Resolving Simulations of Arctic Stratus Part II: Transition-Season Clouds. *Atmos. Res.*, **51**, 45-75.

Heymsfield A. J. and C. M. R. Platt, 1984: A Parameterization of the Particle Size Spectrum of Ice Clouds in Terms of the Ambient Temperature and the Ice Water Content. *J. Atmos. Sci.*, **41**, 846-855.

Heymsfield A. J. and S. L. Parrish, 1986: An Interactive System for Processing PMS Two-Dimensional Imaging Probe. *J. Atmos. Oceanic Technol.*, **3**, 734-736.

Heymsfield, A. J., L. M. Milosevich, A. Slingo, K. Sassen and D. O'C. Starr, 1991: An Observational and Theoretical Study of Highly Supercooled Altocumulus. *J. Atmos. Sci.*, **48**, 923-945.

Heymsfield, A. J., 1993: Microphysical Structures of Stratiform and Cirrus Clouds, in *Aerosol-Cloud-Climate Interactions*, edited by P. V. Hobbs, pp. 97-121, Academic Press, San Diego, CA.

Hobbs, P. V. and A. L. Rangno, 1985: Ice Particle Concentrations in Clouds. *J. Atmos. Sci.*, **42**, 2523-2549.

\_\_\_\_\_ 1998: Microstructures of Low and Middle-Level Clouds Over the Beaufort Sea. *Quart. J. Roy. Meteor. Soc.*, **124**, 2035-2071.

Hoskins, B. J., M. E. McIntyre and A. W. Robertson, 1985: On the Use and Significance of Isentropic Potential Vorticity Maps, *Quart. J. Roy. Meteor. Soc.*, **111**, 877-946.

Iselin, J. P. and W.J. Gutowski Jr., 1997: Water Vapor Layers in STORM-FEST Rawinsonde Observations. *Mon. Wea. Rev.*, **125**, 1954-1963.

Jiang, H., W. R. Cotton, J. O. Pinto, J. A. Curry, M. .J. Weissbluth, 2000: Cloud Resolving Simulations of Mixed-Phase Arctic Stratus Observed During BASE: Sensitivity to Concentration of Ice Crystals and Large-Scale Heat and Moisture Advection. *J. Atmos. Sci.*, **57**, 2105-2112.

Johnson, R. H., T. M. Rickenbach, S. A. Rutledge, P. E. Ciesielski, and W. H. Schubert, 1999: Trimodal Characteristics of Tropical Convection. *J. Appl. Meteor.*, **12**, 2397-2416.

Kajikawa, M., 1989: Observation of the Falling Motion of Early Snowflakes. Part II: On the Variation of Falling Velocity. *J. Meteor. Soc. Japan*, **67**, 731-737.

King, W. D., D. A. Parkin and R. J. Handsworth, 1978: A Hot Wire Liquid Water Device Having Fully Calculable Response Characteristics. *J. Appl. Meteor.*, **17**, 1809-1813.

Kobayashi, T., 1957: Experimental Research on the Snow Crystal Habit and Growth by Means of a Diffusion Cloud Chamber. *J. Meteor. Soc. Japan*, 75<sup>th</sup> Anniv. Vol., 38-44.

Korolev, A. V., G. A. Isaac and J. Hallett, 1999: Ice Particle Habits in Arctic Clouds. *Geophys. Res. Letters*, **26**, 1299-1302.

Lawson, R. P., A. V. Korolev, S. G. Cober, T. Huang, J. W. Strapp and G. A. Isaac, 1998: Improved Measurements of the Drop Size Distribution of a Freezing Drizzle Event. *Atmos. Res.*, **47-48**, 181-191.

\_\_\_\_\_ and T. L. Jensen, 1998: Improved Microphysical Observations in Mixed-Phase Clouds. American Meteorological Society Conference on Cloud Physics. 17-22 August, Everett, WA pp. 451-454

\_\_\_\_\_, B. A. Baker and C. G. Schmitt, 2001: An Overview of Microphysical Properties of Arctic Clouds Observed in May and July during FIRE.ACE. Accepted for publication in *J. Geophys. Res.*, Special Issue on FIRE.ACE.

Lazarus, S. M., S. K. Krueger and G. G. Mace, 2000: A Cloud Climatology of the Southern Great Plains ARM CART, *J. Climate*, **13**, 1762-1775.

Lenschow, D. H. and L. Kristensen, 1985: Uncorrelated Noise in Turbulence Measurements. *J. Atmos. Oceanic Technol.*, **2**, 68-81.

Lenschow, D. H., 1986: *Aircraft Measurements in the Boundary Layer: Probing the Atmospheric Boundary Layer*, Lenschow, D.H. (Ed.). American Meteorological Society, Boston. 39-55.

Liu, S., 1998: Numerical Modeling of Altocumulus Cloud Layers. Ph D. Dissertation, University of Utah, 148 pp.

Liu, S. and S. K. Krueger, 1998: Numerical Simulations of Altocumulus Using a Cloud Resolving Model and a Mixed Layer Model. *Atmos. Res.*, **47-48**, 461-474.

Mason, B. J., 1994: The Shapes of Snow Crystals – Fitness for Purpose? *Quart. J. Roy. Meteor. Soc.*, **120**, 849-860.

Matveev, L. T., 1984: *Cloud Dynamics*. Atmospheric Science Library, D. Reidel Publishing Company.

McClatchey, R. A., R. W. Fenn, J. E. Selby, F. E. Voltz and J. S. Goring, 1972: Optical Properties of the Atmosphere, 3<sup>rd</sup> Edition, AFCRL-72-0497, Air Force Cambridge Research Labs., 107 pp.

McFarquhar, G. M. and A. J. Heymsfield, 1996: Microphysical Characteristics of Three Anvils Sampled During the Central Equatorial Pacific Experiment (CEPEX). *J. Atmos. Sci.*, **53**, 2401-2423.

\_\_\_\_\_ 1998: The Definition and Significance of an Effective Radius for Ice Clouds. *J. Atmos. Sci.*, **55**, 2039-2052.

Mischenko, M. I., W. B. Russow, A. Macke, and A. A. Lacis, 1996: Sensitivity of Cirrus Cloud Albedo, Bi-directional Reflectance and Optical Thickness Retrieval Accuracy to Ice Particle Shape. *J. Geophys. Res.*, **101**, 16973-16985.

Mitchell, D. L., R. Zhang and R. Pitter, 1990: Mass-Dimensional Relationships for Ice Particles and the Influence of Riming on Snowfall Rates. *J. Appl. Meteor.*, **29**, 153-163.

Mitchell, D. L., 1996: Use of Mass- and Area-Dimensional Power Laws for Determining Precipitation Particle Terminal Velocities. *J. Atmos. Sci.*, **53**, 1710-1723.

Nakaya, U., 1954: *Snow Crystals, Natural and Artificial*. Harvard Univ. Press, Cambridge, England.

Nicholls, S., 1984: Dynamics of Stratocumulus: Aircraft Observations and Comparisons with a Mixed Layer Model. *Quart. J. Roy. Meteor. Soc.*, **110**, 783-820.

Paltridge, G. W., W. J. King and C. M. R. Platt, 1986: A Case Study of Ice Particle Growth in a Mixed-Phase Altostratus Cloud. *Aust. Meteor. Mag.*, **34**, 149-154.

- Passarelli, R. E., 1978: Theoretical and Observational Study of Snow-Size Spectra and Snowflake Aggregation Efficiencies. *J. Atmos. Sci.*, **35**, 882-889.
- Pinto, J. O., 1998: Autumnal Mixed-Phase Cloudy Boundary Layers in the Arctic. *J. Atmos. Sci.*, **55**, 2016-2037.
- Poellot, M. R., W. P. Arnott and J. Hallett, 1999: In-situ Observations of Contrail Microphysics and Implications for their Radiative Impact. *J. Geophys. Res.*, **104**, 12,077-12,084.
- Randall, D. A., 1984: Stratocumulus Cloud Deepening through Entrainment. *Tellus*, **36A**, 446-457.
- \_\_\_\_\_ 1989: Interactions Among Radiation, Convection, and Large-Scale Dynamics in a General Circulation Model. *J. Atmos. Sci.*, **46**, 1943-1970.
- Rauber, R. M. and A. Tokay, 1991: An Explanation for the Existence of Supercooled Water at the Tops of Cold Clouds. *J. Atmos. Sci.*, **48**, 1005-1023.
- Ritter, B. and J. F. Geleyn, 1992: A Comprehensive Radiation Scheme for Numerical Weather Prediction Models with Potential Applications in Climate Situations. *Mon. Wea. Rev.*, **120**, 303-325.

Rockel, B., E. Raschke and B. Weyres, 1991: A Parameterization of Broad Band Radiative Properties of Water, Ice and Mixed Clouds. *Beitr. Phys. Atmos.*, **64**, 1-12.

Rogers, R. R. and M. K. Yau, 1989: *A Short Course in Cloud Physics*, Third Edition. Pergamon Press, 293 pp.

Stephens, G. L., 1978: Radiation Profiles in Extended Water Clouds. I: Theory. *J. Atmos. Sci.*, **35**, 2111-2122.

Stephens, G. L., 1994: *Remote Sensing of the Lower Atmosphere, An Introduction*. Oxford University Press, 523 pp.

\_\_\_\_\_ and P. J. Webster, 1979: Sensitivity of Radiative Forcing to Variable Cloud and Moisture. *J. Atmos. Sci.*, **36**, 1542-1556.

\_\_\_\_\_, S. C. Tsay, P. W. Stackhouse, Jr., P. J. Flatau, 1990: The Relevance of the Microphysical and Radiative Properties of Cirrus Clouds to Climate and Climatic Feedback. *J. Atmos. Sci.*, **47**, 1742-1753

\_\_\_\_\_, P. Gabriel, and P. T. Partain, 2000: Parameterization of Atmospheric Radiative Transfer. Part I: Validity of Simple Models. Submitted to *J. Atmos. Sci.*

Strapp, J. W., P. Chow, M. Maltby, A. D. Bezer, A. Korolev, I. Stromberg and J. Hallett, 1999: Cloud Microphysical Measurements in Thunderstorm Outflow Regions during Allied/BAE 1997 Flight Trials. AIAA 00-0498.

Stull, R. B., 1988: *An Introduction to Boundary Layer Meteorology*, Kluwer Academic Publishers, Norwell, MA., 666 pp.

Sun, Z., and K. P. Shine, 1994: Studies of the Radiative Properties of Ice and Mixed-Phase Clouds. *Quart. J. Roy. Meteor. Soc.*, **120**, 111-137.

Tiedtke, M., 1993: Representation of Clouds in Large-Scale Models. *Mon. Wea. Rev.*, **121**, 3040-3060.

Tulich, S. N. and T. H. Vonder Haar, 1998: Measured and Calculated Structures of a Multi-Layer Altocumulus Cloud. M.S. Thesis, CSU Atmos. Sci. Paper #647, 190 pp.

Twomey, S., 1974: Pollution and the Planetary Albedo, *Atmos. Environ.*, **8**, 1251-1256.

Vonder Haar, T. H., S. K. Cox, G. L. Stephens, J. M. Davis, T. L. Schneider, W. A. Peterson, A. C. Huffman, K. E. Eis, D. L. Reinke and J. M. Forsythe, 1997: Overview and Objectives of the DoD Center for Geosciences Sponsored "Complex Layered Cloud Experiment". Preprints, Cloud Impacts on DoD Operations and Systems Conference, September 23-25, Newport, R.I.

Warren, S. G., C. J Hahn, J. London, R. M. Chervin and R. Jenne, 1988: Global Distribution of Total Cloud Cover and Cloud Type Amount Over Land. NCAR TN-317 STR, 212 pp.

Warren, S. G., C. J Hahn, J. London, R. M. Chervin and R. Jenne, 1988: Global Distribution of Total Cloud Cover and Cloud Type Amount Over the Ocean. NCAR TN-317 STR, 212 pp.

Young, S. A., C. M. R. Platt, R. T. Austin and G. R. Patterson, 2000: Optical Properties and Phase of Some Mid-latitude, Mid-level Clouds in ECLIPS. *J. Appl. Meteor.*, **39**, 135–153.